Autonomous Robotic Inspection and Maintenance on Ship Hulls and Storage Tanks

Deliverable report – D3.1

Context	
Deliverable title	Simultaneous localisation and geometry inference on a metal plate
Lead beneficiary	CETIM
Author(s)	H. WALASZEK, Q.A.VU, A. SAIDOUN, N. SAMET, E. NDIAYE (CETIM) O. Ouabi (CNRS)
Work Package	WP3
Deliverable due date	31st March 2022 (M27)
Document status	
Version No.	1
Type	REPORT
Dissemination level	Public
Last modified	07 April 2022
Status	RELEASED
Date approved	07 April 2022
Approved by Coordinator	Prof. Cédric Pradalier (CNRS) Signature: 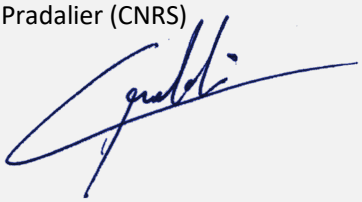
Declaration	Any work or result described therein is genuinely a result of the BugWright2 project. Any other source will be properly referenced where and when relevant.

This project has received funding from the European Union's Horizon 2020 research and innovation programme under Grant Agreement No. 871260

TABLE OF CONTENTS

LIST OF FIGURES

HISTORY OF CHANGES

Date	Written by	Description of change	Approver	Version No.
03/2022	CTIM	Creation of the document	CNRS	0.1
31/03/22	CNRS	Proofreading	CNRS	1
31/04/22	CTIM	Modifications	CNRS	1.1
01/04/22	CNRS	Proofreading	CNRS	

ABBREVIATIONS

UGW	Ultrasonic Guided Waves
PWAS	Piezoelectric Wafer Active Sensors
TRL	Technology readiness level
SLAM	Simultaneous Localisation and Mapping

Executive summary

This document corresponds to deliverable D3.1 entitled "Simultaneous localisation and geometry inference on a metal plate", planned at M27 of the project. The work carried out in this phase of the project aims to develop a control methodology based on Ultrasonic Guided Waves (UGW) in order to meet the following objectives:

- The detection of the plate boundaries (i.e., welding joints)
- The simultaneous recovery of plate geometry and robot localisation

I. Introduction

In order to meet these objectives, a collaboration between the CETIM, CGE (CETIM Grand Est) and the CNRS has been organised around two major subjects that have been conducted in parallel, but are meant to be jointly integrated in the final robotic setup:

- The first subject consists in carrying out a numerical and experimental analysis of the interaction between different guided wave modes, and representative discontinuities of a ship's hull (welding joint, ribs-stiffeners). The objective of this phase is to define the sensitivity of each guided wave mode, as function of the discontinuities encountered by the ultrasonic wave and thus to determine the most suitable sensor technology. At the end of this work, we selected a transducer in order to generate the previously selected wave and to optimise the resolution of the guided wave measurement results in order to simplify the interpretation.

- The second subject concerns the elaboration of a methodology to achieve simultaneous localisation and plate geometry inference using ultrasonic guided waves. The considered setup only requires a collocated emitter/receiver pair of piezoelectric transducers that is mounted on a mobile platform. By relying on the acoustic reflections on the plate boundaries, accurate sensor localisation and plate geometry reconstruction can be achieved. The proposed approach is tested experimentally, in a laboratory environment, and using isolated metal plates. Industrial 1MHz contact piezoelectric transducers are used for signal in emission and reception, and a low order antisymmetric acoustic mode is selected for the proof-of-concept experiments.

- Acoustic localisation and mapping typically require prior knowledge of the wave propagation. However, this may not be a realistic assumption when considering a practical robotic inspection operation (due to variations of the local structure properties and operation conditions). Hence, we have elaborated a methodology to simultaneously localise plate boundaries and recover the propagation model. The experimental results show that it is beneficial to the targeted objective.

The results of this work have been the subject of four research papers:

- Application of ultrasonic guided waves to localisation and geometry inference on a metal plate, (in the process of submission in Ultrasonics, 2022).
- On-plate localisation and mapping for an inspection robot using ultrasonic guided waves, published in IEEE/RSJ International Conference on Intelligent Robots and Systems (IROS) (Pradalier, et al., 2020).

- A FastSLAM approach integrating beamforming maps for ultrasound-based robotic inspection, published in IEEE Robotics and Automation Letters (Ouabi, et al., 2021).
- Learning the propagation properties of rectangular metal plates for Lamb wave-based mapping, published in Ultrasonics (Ouabi, et al., 2022).

Finally, the procedure followed for the selection of the ultrasonic sensor is explained. Additional tests are to be carried out to decide on the sensor choice.

II. Application of ultrasonic guided waves to localisation and geometry inference on a metal plate

In this part, the work carried out within the framework of WP3, task D3.1 is organized into four papers, three of which have already been published and a fourth one that is currently under review. These papers are attached at the end of this deliverable.

- The first paper (Walaszek, et al., 2022) summarises the numerical and experimental study carried out on a representative model to better understand the interaction between the different types of guided waves with the obstacles present in the structure of a boat hull (welds, ribs-stiffeners, and transverse webs).

- In (Pradalier, et al., 2020), a first proposal for the use of UGW for localisation and mapping of the autonomous robot on a steel plate is presented.

- Then, in (Ouabi, et al., 2021), a novel FastSLAM approach for a robotic system inspecting structures made of large metal plates is presented.

- Finally, (Ouabi, et al., 2022) proposes a novel approach based on GW for autonomous navigation and environment sensing.

The abstracts of the four papers are presented below:

Application of ultrasonic guided waves to localisation and geometry inference on a metal plate

H. WALASZEK[1], Q.A.VU[1], A. SAIDOUN[1], N. SAMET[2], E. NDIAYE[2], J. THABOUREY[2]

[1]CETIM, 52 avenue Félix Louat, Senlis - France

[2] CETIM Grand Est, 21 rue de Chemnitz, BP 2278, Mulhouse - France

ABSTRACT

Non-destructive inspection of large structures represents one of the major challenges in various industrial sectors (energy, oil & gas, naval, etc.). In recent years, non-destructive testing methods, in particular ultrasonic methods, have been increasingly integrated into autonomous robots in order to carry out faster inspections, and therefore more reliable maintenance without the direct intervention of human operators. The benefit of using a robot during the inspection of large structures consists in the automatization of ultrasonic probe handling and motion, with controlled and reproduceable coupling of ultrasonic probes with the structure to be inspected. Some robotized ultrasonic crawlers are currently available, but are based on local ultrasonic measurements, that leads to important time of operation to scan large hull surfaces. In addition to their potential to detect defects, ultrasonic methods, and in particular guided waves, are able to propagate for several meters. Guided wave could allow precise

localisation of the robot and also mapping of structural configurations based on acoustic characteristics of reflected or transmitted waves. In the present work, the boat hull case is considered. A numerical and experimental analysis was carried out in order to study the interactions between different guided wave modes and discontinuities (welds, ribs-stiffeners, and transverse webs). The final objective of this study is the development and integration of an inspection technology in an autonomous robot system applied to the control of large structures (ex: boat hull, tank, etc.).

Submission in Ultrasonics (2022)

On-plate Localisation and mapping for an inspection robot using ultrasonic guided waves[1]

C. PRADALIER[1], O. OUABI[1], P. POMAREDE[1], J. STECKEL[2, 3]

[1]International Research Lab 2958 Georgia Tech-CNRS, Metz, France

[2]University of Antwerp, Antwerp, Belgium

[3]Flanders Make Strategic Research Center, Lommel, Belgium

ABSTRACT

This paper presents a proof-of-concept for a localisation and mapping system for magnetic crawlers performing inspection tasks on structures made of large metal plates. By relying on ultrasonic guided waves reflected from the plate edges, we show that it is possible to recover the plate geometry and robot trajectory to a precision comparable to the signal wavelength. The approach is tested using real acoustic signals acquired on metal plates using lawn-mower paths and random-walks. To the contrary of related works, this paper focuses on the practical details of the localisation and mapping algorithm.

Published in: IEEE/RSJ International Conference on Intelligent Robots and Systems, 2020.

A FastSLAM Approach Integrating Beamforming Maps for Ultrasound-Based Robotic Inspection of Metal Structures[2]

O. OUABI[1], P. POMAREDE[1], N. F. DECLERCQ[1,3], M. GEIST[2], C. PRADALIER[1]

[1]International Research Lab 2958 Georgia Tech-CNRS, Metz, France

[2]Google Research, Brain Team, Paris, France

[3]Georgia Institute of Technology, Atlanta, GA30332-0250 USA

ABSTRACT

We present a novel FastSLAM approach for a robotic system inspecting structures made of large metal plates. By taking advantage of the reflections of ultrasonic guided waves on the plate boundaries, it is possible to recover, with enough precision, both the plate shape and the robot trajectory. Contrary to our previous work, this approach considers the dispersive nature of guided waves in metal plates. This is leveraged to construct beamforming maps from which we solve the mapping problem through plate edges estimation for every particle, in a FastSLAM fashion. We demonstrate, with real acoustic measurements obtained on different metal plates, that such a framework achieves more accurate results, while the complexity of the algorithm is sensibly reduced.

Published in: IEEE ROBOTICS AND AUTOMATION LETTERS, VOL. 6, NO. 2, APRIL 2021

[1] **DOI**: 10.1109/IROS45743.2020.9340936

[2] **DOI**: 10.1109/LRA.2021.3062600

Learning the propagation properties of rectangular metal plates for Lamb wave-based mapping[3]

O. OUABI[1], P. POMAREDE[1], N. F. DECLERCQ[1, 3], N. ZEGHIDOUR[2], M. GEIST[2], C. PRADALIER[1]

[1]International Research Lab 2958 Georgia Tech-CNRS, Metz, France

[2]Google Research, Brain Team, Paris, France

[3]Georgia Institute of Technology, Atlanta, GA30332-0250 USA

ABSTRACT

The inspection of sizeable plate-based metal structures such as storage tanks or marine vessel hulls is a significant stake in the industry, which necessitates reliable and time-efficient solutions. Although Lamb waves have been identified as a promising solution for long-range non-destructive testing, and despite the substantial progress made in autonomous navigation and environment sensing, a Lamb-wave-based robotic system for extensive structure monitoring is still lacking. Following previous work on ultrasonic Simultaneous Localisation and Mapping (SLAM), we introduce a method to achieve plate geometry inference without prior knowledge of the material propagation properties, which may be lacking during a practical inspection task in challenging and outdoor environments. Our approach combines focalization to adjust the propagation model parameters and beamforming to infer the plate boundaries location by relying directly on acoustic measurements acquired along the mobile unit trajectory. For each candidate model, the focusing ability of the corresponding beamformer is assessed over high-pass filtered beamforming maps to further improve the robustness of the plate geometry estimates. We then recover the optimal space-domain beamformer through a simulated annealing optimization process. We evaluate our method on three sets of experimental data acquired in different conditions and show that accurate plate geometry inference can be achieved without any prior propagation model. Finally, the results show that the optimal beamformer outperforms the beamformer resulting from the predetermined propagation model in non-nominal acquisition conditions.

Published in: Ultrasonics 106705, 2022.

III. Sensor and Mapping Concepts

Based on the results presented in (Walaszek, et al., 2022), the candidate sensor for our application should meet the following requirements:

- modal selectivity on transmission and detection: generate/detect properly the SH_0 mode with the best SNR possible
- omnidirectional transmission and reception
- the echo mode will be preferred (transmitter and receiver probe at the same location)

In order to meet these conditions, two innovative technologies will be tested in this project:

► PZT omnidirectional sensors

Piezoelectric sensors are sensors widely used in non-destructive ultrasonic testing. They are often used to produce bulk waves. When they are used to generate guided waves, they can be coupled with a wedge or often with a strong mechanical pressure to ensure correct acoustic coupling. The desired mode can be produced but it is on one hand directive and on the second hand often followed by another non-desired mode. Unwanted modes are often sources of disturbances and complicate the analysis and understanding of signals due to their dispersion. Directional sensors are not suitable for our TFM reconstruction application which requires an omnidirectional sensor.

[3] **DOI**: https://doi.org/10.1016/j.ultras.2022.106705

Generating a mono-mode with omnidirectional piezoelectric sensor is not an easy task, several authors have worked on this subject and the best solutions are exposed in (Miao, 2017).

Figure 1 present a new design of omnidirectional sensor which allows to generate the only fundamental mode SH_0 is shown (Miao, 2017).

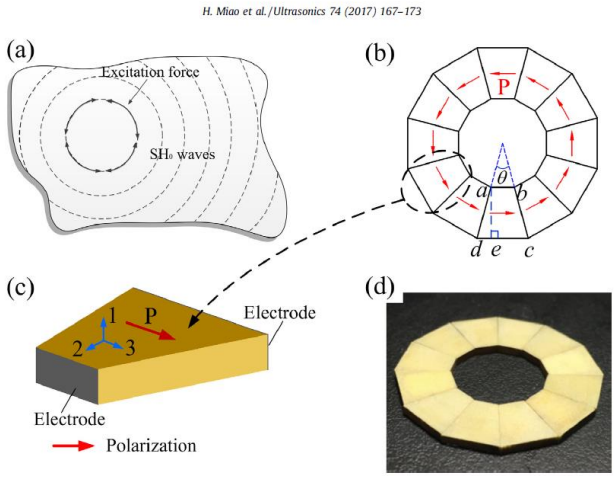

Figure 1: New omnidirectional sensor design to generate SH0 waves

The sensor is a ring array of twelve trapezoidal d_{24} face shear PZT elements. Each PZT element can produce face shear deformation, thus effective circular shear deformation can be done. The performance of omnidirectional SH_0 wave piezoelectric transducer (OSH-PT) has been examined by both finite element simulations and experimental tests. It was found that OSH-PT can excite and receive pure SH_0 waves in a selected frequency range where no other undesired wave modes are generated such as Lamb waves.

In the same context Huan (Huan, 2019) & (Huan, 2019) proposed a sensor solution for the omnidirectional wave generation of the fundamental mode SH_0 (Figure 2).

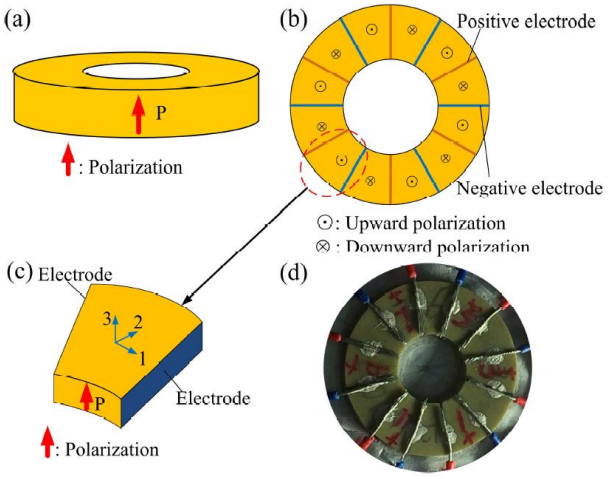

Figure 2: Schematic structure of the proposed omnidirectional SH wave piezoelectric transducer (OSH-PT): (a) a thickness poled PZT ring; (b) polarization and wiring of the 12 evenly divided elements of the PZT ring; (c) polarization and electrodes of a single PZT element; (d) picture of the actually fabricated OSH-PT

In 2008, Lingyu Yu and Victor Giurgiutiu from the University of South Carolina (Lingyu, 2008) were working on an in-situ method for damage detection in thin-wall structures using embedded 2-D ultrasonic phased arrays with Piezoelectric Wafer Active Sensors (PWAS). This method uses scanning beams of guided Lamb waves that can travel for large distances with little energy loss. The PWAS phased array rely on the selective excitation of single-mode guided waves that are best adapted for phased array damage detection for a given plate thickness and material characteristics.

The authors tested several array configurations with different geometrical shapes and concluded that rectangular array provides the suitable result. This configuration shows that it can achieve single beamforming within 360° range with an optimized combination of good directionality and compact size.

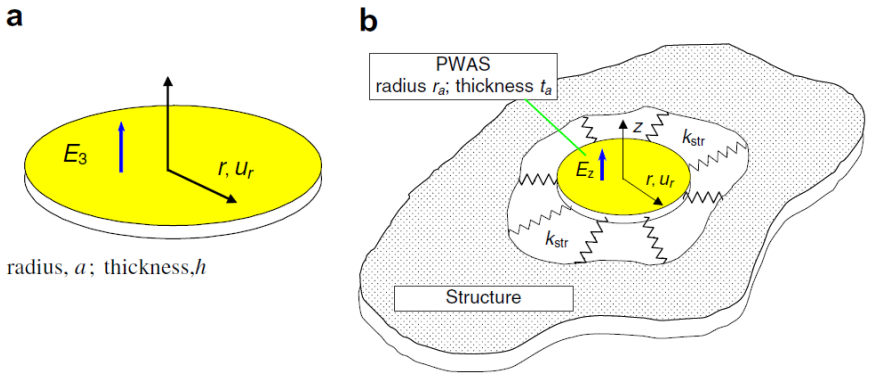

Figure 3: Circular PWAS illustration: (a) the schematic; (b) a circular PWAS constrained by structural stiffness, kstr (ω)

Even if experiments are conducted at very low frequency ranges, A_0 and S_0 Lamb waves exist simultaneously. Giurgiutiu (Giurgiutiu, 2005) showed that the PWAS length 2a, plate thickness 2d, and material properties μ and λ, it is possible to find frequencies at which only one mode (A_0 or S_0) is existing (Figure **3**).

► Magnetostrictive omnidirectional sensors

Magnetostrictive sensors are widely used for GW pipeline control. Figure 4 shows an example of a magnetostrictive system. It is composed of a magnetised metal strip and a coil on top. To generate guided waves by magnetostriction, a pulsed current is introduced into a transmitting coil coupled to a ferromagnetic material. The local modification of the magnetisation of the material is accompanied by a deformation of the material in a direction parallel to the applied magnetic field. This deformation, which corresponds to the magnetostrictive effect, generates a shear horizontal wave. The probes used enable the generation of waves from a few kHz to a few hundred kHz which propagate at the speed of ultrasonic waves in the material. When this wave is reflected by the presence of a defect or obstacle and reaches the receiving coil, the magnetic flux in this coil changes. This change induces an electric current in the "receiving" coil which is proportional to the amplitude of the mechanical wave. This current is then amplified, conditioned, and analysed.

Figure 4: magnetostrictive guided wave system - MsSR3030 (SWRI)

In the context of an application on boat hulls, the system presented Figure **4** is not completely adapted. Despite the good selectivity of the SH mode, the magnetostrictive probe remains directional. However, a recent product from SWRI company associating the magnetostrictive probe with a rotating system allowing to perform a 360° scan synchronised with the acquisition system. Figure **5** shows the Mst 360 probe. The scanner rotates the MsT for data collection at regular angular intervals using a single or multiple frequencies.

Figure 5: MsT 360 Probe (SWRI)

Feasibility tests will be conducted with this new probe on the mock-up, first to finalise the test plan on the location of obstacles and further, for Task 3.2 "Defect localisation by acoustic triangulation and tomography" for the detection of defects.

It shall be noted that other transducers called "EMAT" are able to produce guided waves, without physical contact of the probe with the plate (Salzburger, 2013). These transducers do not need either coupling agent, which is a substantial advantage. The GW EMAT transducers available on the market are directional, but some papers describe omni-directional solutions. Such a solution was not studied because we favoured more advanced methods in TRL (Technology readiness level) at this stage of the study.

IV. On-plate Simultaneous Localisation and Mapping Framework

This section presents the Simultaneous Localisation and Mapping (SLAM) framework based on guided waves that we have elaborated. Our objective is to recover simultaneously the sensor position and the metal plate geometry (i.e. the position of weld joints on a large structure) by relying on the acoustic reflections of the excited wave on the plate boundaries. We assume that the acoustic sensors and the selected acoustic mode meet the requirements specified in the previous section.

As the sensor is to be mounted on a robotic platform, it is assumed that noisy odometry information (typically provided by the wheels encoders or Inertial Measurement Unit) is available. It should also be noted that other localisation systems (such as ultra-wide band beacons) may be used in combination with guided waves for accurate robot localisation, although it is not yet the case in the conducted experiments.

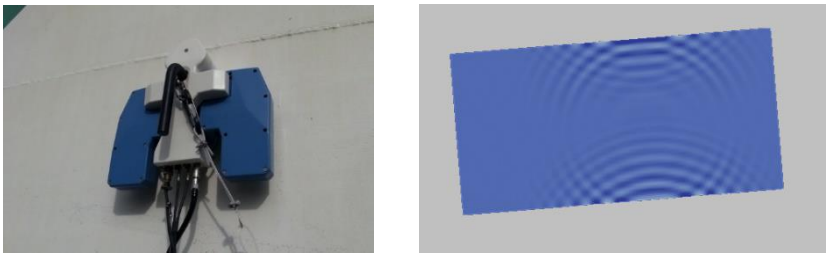

Figure 6: Left, close-up of the Altiscan magnetic crawler on a storage tank. Right, omnidirectional guided waves reflecting on the edges of a metal panel in a simulated environment.

Acoustic SLAM has been the subject of various research works. However, the methods presented in the literature that tackle the similar problem of room shape reconstruction using acoustic echoes are evaluated in simulation and rely on important assumptions that may not be applicable in practice to ultrasonic measurements. Hence, we have first developed a proof-of-concept approach based on a FastSLAM algorithm (Pradalier, et al., 2020) for solving the online SLAM problem on an isolated metal panel, while tackling echo detection (for retrieving a list of ranges from the acoustic measurements) and association (grouping the acoustic echoes from different observation positions that originate from a reflection on the same boundary).

We have subsequently introduced beamforming to achieve plate boundary mapping (Ouabi, et al., 2021), which alleviates the need for specifically tackling the echo detection and echo association problems, but we restrain the estimated geometries to rectangular shapes. This proved to lead to more accurate and robust estimation results. Furthermore, the rectangular geometry constraint is not considered as an issue, as ship hulls and storage tanks are made in majority of rectangular metal panels.

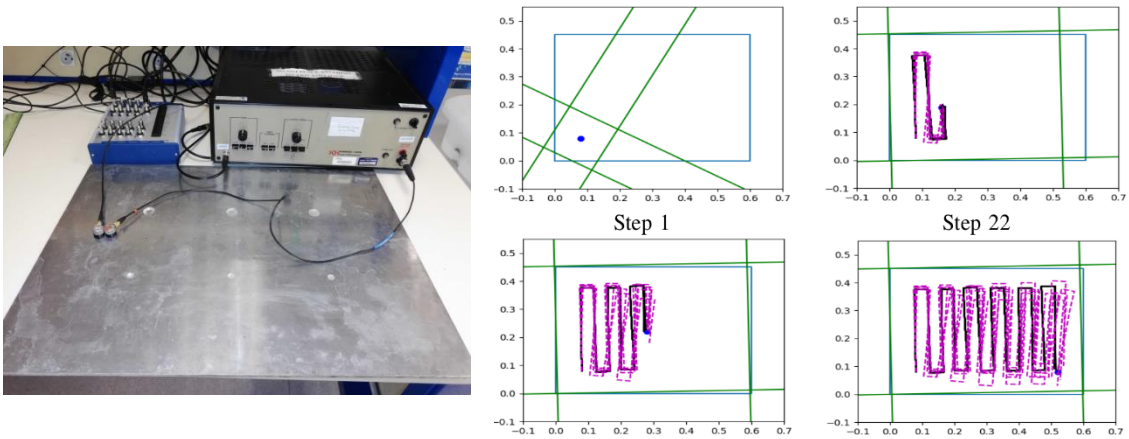

Figure 7: Left, picture of the experimental setup for acquiring the acoustic measurements.
Right, an example of SLAM results obtained

In our experiments, we have considered the A_0 Lamb wave mode, which is omnidirectional and is predominant in low frequencies. Our approach is tested using acoustic measurements that are acquired by moving manually on the metal surface, a pair of nearly collocated V103-RM U8403008 contact piezoelectric transducers (see Fig.4, left). The results show that centimetre precision in localisation and mapping can be achieved on a small aluminium panel (600x450x6mm) and a larger steel plate (1700x1000x6mm) in a laboratory environment, and limited odometry noise conditions, as illustrated by Figure 4, right. Hence, this demonstrates the feasibility of guided wave-based SLAM and represents a first step towards long-range robotic inspection. The detailed presentation of the work is available in the article (Ouabi, et al., 2021).

The methods mentioned above typically require prior knowledge of the acoustic signal propagation in the metal plate. However, the hypothesis that the propagation model is known a priori may not be realistic for a practical inspection task on a large metal structure due to a wide variety of external perturbations that can significantly affect the acoustic signals, and to a lack of knowledge of the structure physical condition (which is the reason why it is being inspected). For these reasons, we have addressed the problem of simultaneous acoustic mapping and propagation model calibration.

The proposed approach relies on optimal beamforming, for achieving plate geometry inference concurrently to propagation model calibration by relying on measured data itself. The experimental results obtained in a laboratory environment demonstrate its efficiency, with the notable result that optimal beamforming leads to better reconstruction results when the acquisition conditions deteriorate compared to a fixed predetermined propagation model. The details on both the methodology and experimental results are available in (Ouabi, et al., 2022).

V. Conclusion

This document summarizes the work carried out in Task 3.1 “Simultaneous Localisation and Geometry Inference on a metal plate”. The main conclusions are as follow:

Numerical simulations enable the comparison between the sensitivity of the different modes of GW in relation with the detection of discontinuities (welding, stiffeners). Due to its low dispersion and the absence of mode conversion, SH_0 seems to be the best candidate for our application.

- The experimental tests carried out on a representative mock-up have allowed to validate all the numerical results.
- The proposed imaging methodology, which gives a global view of the GW response of the area under scan improves the resolution of the results and also simplifies their analysis
- A demonstration of the feasibility of SLAM on a metal structure using omnidirectional guided waves
- The automatic calibration of the propagation model for plate geometry mapping by relying on the acoustic data itself.

References

Giurgiutiu, 2005. Tuned Lamb Wave Excitation and Detection with Piezoelectric Sensors for Structural Health Monitoring. *Journal of Intelligent Material Systems and Structures,* Volume 16.

Huan, 2019. A high-resolution structural health monitoring system based on SH wave piezoelectric transducers phased array. *Ultrasonics,* Volume 97, pp. 29-37.

Huan, 2019. A practical omni-directional SH wave transducer for structural health monitoring based on two thickness-poled piezoelectric half-rings. *Ultrasonics,* Volume 94, pp. 342-349.

Lingyu, 2008. In situ 2-D piezoelectric wafer active sensors arrays for guided wave damage detection. *Ultrasonics,* Volume 48, pp. 117-134.

Liu, Z., 2018. Development of an omnidirectional SH0 mode electromagnetic acoustic transducer employing a circumferential periodic permanent magnet array. *I EEE Sensors,* Volume vol 21 issue 6.

Miao, 2017. A new omnidirectional shear horizontal wave transducer using face-shear (d24) piezoelectric ring array. *Ultrasonics,* Volume 74, pp. 167-173.

Ouabi, et al., 2021. A fastslam approach integrating beamforming maps for ultrasound-based robotic inspection of metal structures. *IEEE Robotics and Automation Letters,* Volume 6(2), pp. 2908-2913.

Ouabi, et al., 2022. Learning the propagation properties of rectangular metal plates for Lamb wave-based mapping. *Ultrasonics,* p. 106705.

Pradalier, Ouabi, Pomarede & Steckel, 2020. On-plate localisation and mapping for an inspection robot using ultrasonic guided waves: a proof of concept. *IEEE/RSJ International Conference on Intelligent Robots and Systems (IROS),* pp. 5045-5050.

Salzburger, H., 2013. EMAT pipe inspection with guided waves welding in the world. *le soudage dans le monde ,* pp. 5-6.

Walaszek, H. et al., 2022. Application of ultrasonic guided waves to localisation and geometry inference on a metal plate.

Annexes

Ouabi, et al., 2021. A fastslam approach integrating beamforming maps for ultrasound-based robotic inspection of metal structures. *IEEE Robotics and Automation Letters,* Volume 6(2), pp. 2908-2913.

Ouabi, et al., 2022. Learning the propagation properties of rectangular metal plates for Lamb wave-based mapping. *Ultrasonics,* p. 106705.

Pradalier, Ouabi, Pomarede & Steckel, 2020. On-plate localisation and mapping for an inspection robot using ultrasonic guided waves: a proof of concept. *IEEE/RSJ International Conference on Intelligent Robots and Systems (IROS),* pp. 5045-5050.

Walaszek, H. et al., 2022. Application of ultrasonic guided waves to localisation and geometry inference on a metal plate.

A FastSLAM Approach Integrating Beamforming Maps for Ultrasound-Based Robotic Inspection of Metal Structures

Othmane-Latif Ouabi, *Graduate Student Member, IEEE*, Pascal Pomarede, Matthieu Geist, Nico F. Declercq, and Cédric Pradalier, *Member, IEEE*

***Abstract*—We present a novel FastSLAM approach for a robotic system inspecting structures made of large metal plates. By taking advantage of the reflections of ultrasonic guided waves on the plate boundaries, it is possible to recover, with enough precision, both the plate shape and the robot trajectory. Contrary to our previous work, this approach takes into account the dispersive nature of guided waves in metal plates. This is leveraged to construct beamforming maps from which we solve the mapping problem through plate edges estimation for every particle, in a FastSLAM fashion. It will be demonstrated, with real acoustic measurements obtained on different metal plates, that such a framework achieves more accurate results, while the complexity of the algorithm is sensibly reduced.**

***Index Terms*—Industrial robots, range sensing, SLAM.**

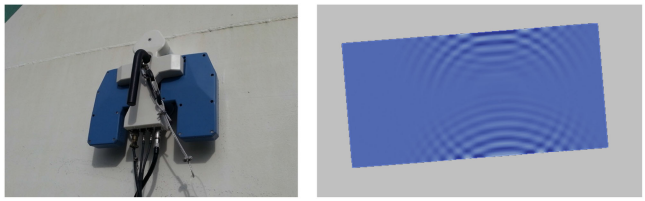

Fig. 1. (Left) A magnetic crawler carrying out an inspection task on a metal structure. (Right) Guided waves reflected by the edges of a plate in a simulation environment. We aim to enable on-plate localization and mapping with a high precision for magnetic crawlers equipped with acoustic transducers, and relying on such ultrasonic reflections.

I. Introduction

In this work[1], we describe a new FastSLAM approach [1] to achieve Simultaneous Localization and Mapping (SLAM) for a robotic system relying on Ultrasonic Guided Waves (UGWs) to support inspection tasks on large metal structures such as storage tanks or ship hulls. In Structural Health Monitoring (SHM), acoustic tomography techniques can be used for defect detection and characterization, but they rely on the accurate prior knowledge of the positions of the sensors which are integrated into the structure [2], [3]. To deploy similar methods on a robotic platform, recovering the robot position with respect to the individual metal plates may be beneficial, as it could lead, in combination with external localization systems, to precise localization of the mobile unit, and thus, to accurate inspection results.

On metal plates, guided waves are often generated by applying piezo-electric transducers in contact with the surface. These waves propagate radially around the emitter through the plate material, and potentially over large distances. When encountering the plate edges, these waves are reflected perpendicularly, and a receiver can sense the reflections. In this setup, the resulting acoustic data carry essential information on the source position and the plate geometry.

In this work, we consider a mobile unit equipped with acoustic transducers for both emission and reception, and moving on a metal surface. We leverage the sensing of the ultrasonic reflections to estimate both the plate shape and the robot trajectory. The principle of this approach is illustrated in Fig. 1. In the robotic field, this problem is known as Simultaneous Localization and Mapping (SLAM).

One of the significant challenges arises from the dispersive nature of UGWs [4]. It means that the propagation velocity is a function of the wave frequency, resulting in a waveform deformation when the propagation distance increases. Besides, propagation in metal plates is highly reverberant. These characteristics account for the relative complexity of acoustic data and call for specific processing methods to achieve on-plate localization and mapping with high accuracy. On the robotic aspect, recent works consider the similar problem of room shape reconstruction from acoustic echoes [5], [6]. As the sound velocity in the air is constant, the determination, from the measurements, of the first-order reflections is not a significant issue. However, identifying several echoes from guided wave data is

Manuscript received October 14, 2020; accepted February 15, 2021. Date of publication February 26, 2021; date of current version March 18, 2021. This letter was recommended for publication by Associate Editor M. Kaess and Editor S. Behnke upon evaluation of the reviewers' comments. *(Corresponding author: Othmane-Latif Ouabi.)*

Othmane-Latif Ouabi, Pascal Pomarede, and Cédric Pradalier are with the International Research Lab. Georgia Tech-CNRS in Metz, Metz 57070, France (e-mail: oouabi@georgiatech-metz.fr; Pascal.POMAREDE@ensam.eu; cedric.pradalier@gmail.com).

Matthieu Geist is with the Google Research, Paris, France (e-mail: mfgeist@google.com).

Nico F. Declercq is with the International Research Lab. Georgia Tech-CNRS in Metz, Metz 57070, France and also with the Georgia Institute of Technology, Atlanta, GA 30332-0250 USA (e-mail: declercq@gatech.edu).

This letter has supplementary downloadable material available at https://doi.org/10.1109/LRA.2021.3062600, provided by the authors.

Digital Object Identifier 10.1109/LRA.2021.3062600

[1]This work is part of the BugWright2 project. This project is supported by the European Commission under Grant 871260 - BugWright2.

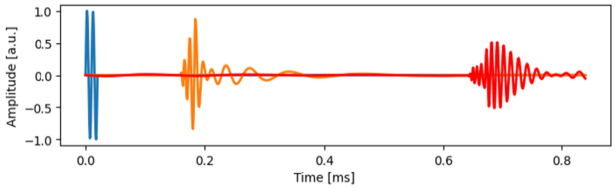

Fig. 2. Illustration of wave dispersion in plates with simulated data. The excitation signal is in blue, the signal propagated after 0.5 meters in orange, and the signal propagated after 2 meters in red.

more difficult due to the wave dispersion and the wave packets overlapping.

In our previous work [7], ultrasonic measurements on metal plates have proven to yield sufficient information to provide both localization and mapping capabilities on metal plates. However, the dispersive nature of the waves was not taken into account and the relative complexity of the algorithm may jeopardize its robustness and accuracy. In this paper, we present an alternative method to solve the SLAM problem from ultrasonic measurements. First, a wave propagation model is introduced and is leveraged to detect acoustic reflections. From them, we build beamforming maps [8] which are subsequently integrated into a FastSLAM framework to solve the mapping problem. Our approach achieves more accurate results than our previous method on real data, with less algorithmic complexity.

In summary, our contributions are the introduction of propagation models and the integration of beamforming maps in FastSLAM to achieve on-plate Simultaneous Localization and Mapping with high accuracy for robotic inspection.

II. Related Work

On the one hand, standard methods to inspect large metal structures consist in deploying a mobile robot to perform point-by-point thickness measurements with an acoustic probe, but the entire surface cannot be inspected in a reasonable amount of time due to the limited surface of the transducer. On the other hand, UGWs have been successfully used by SHM systems to inspect large structures such as pipelines or rails [4], [9], but the transducers are integrated into the structure and their position is known accurately. Hence, outside of the authors' works, UGWs-based techniques have not been deployed on a robotic system, nor have guided waves proven to yield accurate localization capabilities which are critical for such methods to work.

Moreover, UGWs propagation is dispersive, which means that the longer the distance a wave packet travels in a metal plate, the more it deforms. Fig. 2 illustrates this phenomenon. It shows that the shape of the signal is significantly different after propagating over two meters. In SHM, the chosen frequency range generally lies in a dispersion-limited bandwidth, but for our case-study, waves might propagate over much larger distances. Hence, wave dispersion may still have some effects on the signals, and shall not be neglected. In the literature, the use of propagation models in the context of localization and mapping on metal structures has not been thoroughly investigated. This work aims to answer this need.

In typical guided wave data, there are numerous echoes due to the multiple reflections on the plate edges and their number increases exponentially with the observation time. In addition, the wave packets overlap because of the wave dispersion. The consequence is that it is very challenging to recover individual wave-packets from the mixture data [10]. Therefore, most of the recent SHM techniques still rely only on the incident wave packet [3], [4], [11], [12]. For on-plate localization and mapping purposes, however, the retrieval of multiple echoes is essential, as they all provide range-only information to the edges. In the echo detection literature, time-delay estimation techniques have been successfully applied to ultrasound waves in the air [13], [14] but in a non-dispersive context. In [7], we used $\mathcal{L}_1$-regularized least squares to retrieve the multiple echoes without taking into account wave dispersion. Here, we rely on a wave propagation model to determine, through correlation with acoustic data, the likelihood of a reflection over a full range of distances to the transducers. In this new setup, the resolution of the difficult echo association problem is no longer required.

Recently, there have been attempts to infer a plate geometry from guided waves data [15]. Yet, non-dispersive propagation models are used, and the sensors are integrated into the structure. In robotics, the most similar problem is room shape reconstruction from acoustic echoes [5], [6]. However, they rely on sound waves propagating in the air without dispersion and do not consider the association problem to determinate the wall from which each echo originates. In [7], we rely on the most likely echo-line association but the overall algorithm is rather complicated due to the map management, and its robustness is limited. Here, from the likelihoods of reflection, we build beamforming maps to estimate the plate shape and limit ourselves to rectangular geometries (which are to be expected in our application). Then, these elements are integrated into a FastSLAM algorithm to achieve localization and mapping simultaneously.

In summary, we present a new method that efficiently integrates wave propagation models from the guided waves theory and beamforming maps in a FastSLAM algorithm to achieve more accurate on-plate localization and mapping results with less algorithmic complexity comparing to our previous method. The results obtained with experimental acoustic data from different metal plates support our claim.

III. Method

In this work, we are considering a mobile unit equipped with a co-localized emitter/receiver pair of transducers and moving on a metal surface. At the i^{th} scanning position, the emitter sends a pulse $s(t)$ to excite guided waves in the plate material, and the receiver collects the acoustic response $z_i(t)$ which contains the ultrasonic echoes. We intend to use these data and the robot odometry to recover accurately both the plate shape and the robot trajectory.

A. Measurement Model

Acoustic measurements essentially consist in a succession of the reflections of the excitation wave on the plate boundaries. As the small-sized corrosion patches we aim to detect with robotic inspection may not act as reflectors, their potential effect is neglected for the SLAM problem. Under the assumption that the material is isotropic, the propagation linear, and the reflections on the edges are orthogonal, a standard measurement model

to reverberation is the image source model [16]. It relies on the fact that each reflection from the plate boundaries can be considered as a signal originating from a fictional source, which is deduced from the real source position and the reverberant media geometry. In metal plates, the image source model can be leveraged to account for first order as well as higher order reflections, resulting in the following measurements:

$$z_i(t) = \sum_{\mathbf{x} \in \mathcal{I}(\mathbf{x}_i)} g(\mathbf{x}, \mathbf{x}_i, t) * s(t)$$

where $\mathbf{x}_i = [x_i, y_i]$ is the position of the robot during time step i, $\mathcal{I}(\mathbf{x}_i)$ the set of the image sources positions when the real source is in $\mathbf{x}_i$, $g(\mathbf{x}, \mathbf{x}_i, t)$ the acoustic response of the plate to an impulse being generated in $\mathbf{x}$ and received in $\mathbf{x}_i$, and $*$ denotes the convolution operation. In a non-dispersive media, the impulse response is simply given by $g(\mathbf{x}, \mathbf{x}_i, t) = \delta(t - \frac{||\mathbf{x}-\mathbf{x}_i||}{c})$, where δ denotes the Dirac distribution, and c is the constant propagation velocity. It results in waves propagating at a constant speed and without distortion. In a dispersive media like metal plates, a well-suited model of the propagation is given by the solutions of the Helmholtz equation [17]. For an ideal isotropic media, the impulse response is only a function of the propagation distance r between the (fictional) source and the receiver. Moreover, it is usually reduced, in the Fourier domain, to:

$$\hat{g}(r, \omega) \approx e^{-jk(\omega)r} / \sqrt{k(\omega)r}. \tag{1}$$

where $k(\omega)$ is the wavenumber of the major acoustic mode, and its non-linear dependency with respect to the pulsation ω is the typical characteristic of dispersive propagation. More details on how to determine this relation given prior information on the plate material can be found in the literature [4].

B. Correlation-Based Echo Detection

With the aim to retrieve the distances of the robot to the edges from data $z_i(t)$, we use the designed propagation model to estimate the likelihood that an orthogonal reflection occurred at a distance r. First, we consider the signal that would only contain such a reflection: $\hat{z}(r, t) = \hat{g}(2r, t) * s(t)$. Next, we build the correlation signal to assess the likelihood that this pattern is present within the measurement:

$$z'_i(r) = \frac{\langle z_i(t), \hat{z}(r, t) \rangle}{\sqrt{\langle z_i(t), z_i(t) \rangle \langle \hat{z}(r, t), \hat{z}(r, t) \rangle}} \tag{2}$$

where $\langle ., . \rangle$ denotes the scalar product in the domain of continuous signals: $\langle u(t), v(t) \rangle = \int_{-\infty}^{+\infty} u(\tau) v(\tau) d\tau$. As the resulting signal z'_i presents oscillations consistent with the wave spatial periodicity, it is more convenient to only work with its envelope that we will call $z_i(r)$ for simplicity (which shall not be mistaken with the temporal signal $z_i(t)$):

$$z_i(r) = |z'_i(r) + j\mathcal{H}(z'_i)(r)| \tag{3}$$

where $\mathcal{H}$ denotes the Hilbert transform operator. Hence, the resulting signal z_i takes its values only between 0 and 1, and a higher value at r translates into a high likelihood that a reflection occurred at such a distance. In summary, by looking at the local maxima of $z_i(r)$, one can deduce the most likely reflections. Besides, it is noteworthy that a single measurement cannot provide enough information to determine an edge without ambiguity, as all the lines tangent to the circle with radius r and centered at the sensors position may equally account for the correlation measurement.

C. Map Estimation Via Beamforming

Similarly to our previous work, the map is represented by a set of lines: $\mathbf{M} = \{r_l, \theta_l\}_{l=1...4}$ where the parameters (r_l, θ_l) define the line equation in the 2D plane with:

$$x \cdot \cos\theta_l + y \cdot \sin\theta_l - r_l = 0$$

in a non-mobile frame with respect to the plate. Moreover, as we limit our case-study to rectangular shapes, the possible maps possess only four lines forming a rectangle altogether.

Let's assume a hypothetical robot trajectory $\{x_i, y_i\}_{i=1...T}$. We aim at estimating the map $\mathbf{M}$, which means establishing the probability density function $p(\mathbf{M}|x_{1..T}, y_{1..T}, z_{1...T})$. A first solution would consist in assessing, for each map in the 8-D domain, the correlation between the observations and the predicted data based on the image source model. However, such an approach would be far too cumbersome for a real-time application. Instead, we rely on a beamforming map. Such a map attributes, to every line parameters (r, θ), the likelihood of the line existence given the observations with:

$$\mathcal{L}_T(r, \theta) = \sum_{i=1}^{T} z_i(|x_i \cdot \cos\theta + y_i \cdot \sin\theta - r|).$$

where $d_i(r, \theta) = |x_i \cdot \cos\theta + y_i \cdot \sin\theta - r|$ is the distance between the robot during time-step i and the hypothetical line being considered. In the equation, all the correlation values add up constructively along all the observations if an edge is indeed present. Also, it can be noted that only first-order reflections are taken into account, as we reason on individual lines. One may consider that higher order reflections are less likely to account for high correlation amplitudes because of wave scattering after each additional reflection which causes loss of energy to the wave packet. Finally, to retrieve the most plausible map, we solve the following optimization problem:

$$\hat{\mathbf{M}} = \arg\max_{\mathbf{M}} \mathcal{L}_T(\mathbf{M}) = \arg\max_{\mathbf{M}} \sum_{l=1}^{4} \mathcal{L}_T(r_l, \theta_l)$$

where $\mathbf{M}$ is restricted to be a rectangle. It can be solved efficiently by taking that constraint into account. First, one can determine the most likely line:

$$(r_1, \theta_1) = \arg\max_{r,\theta} \mathcal{L}_T(r, \theta).$$

Next, it is possible to rely on the assumption that the retrieved line provides the most reliable estimation of the plate orientation w.r.t. the robot. Therefore, the determination of the other lines for $l = 2, 3, 4$ reduces to solving simple and independent one-dimensional optimization problems:

$$\theta_l = \theta_1 + \frac{\pi(l-1)}{2}\ ; \quad r_l = \arg\max_{r} \mathcal{L}_T(r, \theta_l).$$

D. Particle Evaluation and FastSLAM Algorithm

FastSLAM is a common approach to approximate Bayesian filters in the context of a SLAM problem. It relies on a particle

Algorithm 1: FastSLAM($\mathcal{P}_{T-1}, \mathbf{u}_{T-1}, z_T(r)$).

Data: Particle set $\mathcal{P}_{T-1}$, odometry data $\mathbf{u}_{T-1}$ and correlation measurement $z_T(r)$.
Result: Particle set $\mathcal{P}_T$ for the current time step T.
if *T=0* **then**
  Initialize the particle filter with $\mathcal{P}_0 = \{[x_0, y_0, \alpha_0], \text{null-fuction}\}_{n=1\ldots N}$
else
  for $n = 1\ldots N$ **do**
    $\mathbf{X}_T^{(n)} \sim p\left(\mathbf{X}_T | \mathbf{X}_{T-1}^{(n)}, \mathbf{u}_{T-1}\right)$;
    $\mathcal{L}_T^{(n)}(r,\theta) = \mathcal{L}_{T-1}^{(n)}(r,\theta) + z_T(|x_T^{(n)}\cos\theta + y_T^{(n)}\sin\theta - r|)$;
    $\mathbf{M}_T^{(n)} = \arg\max_{\mathbf{M}} \mathcal{L}_T^{(n)}(\mathbf{M})$;
    $w_T^{(n)} \propto \exp\left\{\beta \sum_{(r_l,\theta_l)\in\mathbf{M}_T^{(n)}} z_T\left(d_T^{(n)}(r_l,\theta_l)\right)\right\}$
  end
  Construct $\mathcal{P}_T$ by sampling each particle proportionally to their respective weight.
end
return $\mathcal{P}_T$.

filter in the localization space, where each particle holds a hypothesis on the map which is inferred from the particle trajectory and the measurements. During time step T, a set with N particles has the following form:

$$\mathcal{P}_T = \left\{\mathbf{X}_T^{(n)} = \{x_i^{(n)}, y_i^{(n)}, \alpha_i^{(n)}\}_{i=1\ldots T}, \mathcal{L}_T^{(n)}\right\}_{n=1\ldots N}$$

where $\mathbf{X}_T^{(n)}$ represents the n-th particle belief on the robot trajectory augmented with its heading over time steps $i = 1\ldots T$, and $\mathcal{L}_T^{(n)}$ its beamforming map which depends on the trajectory. Moreover, each particle is provided with a weight indicating how the particle belief accounts for the measurements. To define it, we rely on the current correlation measurement and assess the likelihoods of the map edges retrieved from $\mathcal{L}_T^{(n)}$ and the current robot position belief:

$$w_T^{(n)} = \eta \cdot \exp\left\{\beta \sum_{(r_l,\theta_l)\in\mathbf{M}_T^{(n)}} z_T\left(d_T^{(n)}(r_l,\theta_l)\right)\right\} \quad (4)$$

where η is the normalization factor and β a positive parameter. It enables to fix the confidence in the correlation measurements and shall be tuned so that the resulting weight distribution is consistent with the motion and observation noises. The weights are used to sample, with replacement, the particles after each time step. Besides, one may note that we are not considering, in (4), the uncertainty on the lines retrieval from the beamforming maps for simplicity. Altogether, the implementation of FastSLAM is given in Algorithm 1.

IV. Results

In this part, we test our FastSLAM approach on experimental data. We detail the experimental setup and show the results in terms of localization and mapping accuracy.

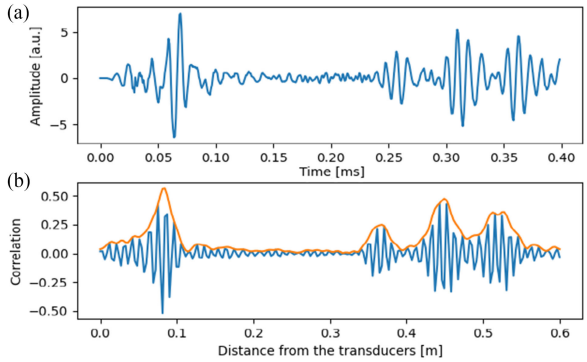

Fig. 3. Illustration of the echo detection principle based on correlation with a propagation model. a) represents the acoustic measurement. b) shows the correlation signal (blue) and its envelope (orange).

A. Experimental Setup

In order to assess the efficiency of our procedure, we use an emitter-receiver pair of transducers on two different metal plates. The first plate has dimensions 600 × 450 × 6mm, is in aluminium, and has small artificial holes on it. The second plate has dimensions 1700 × 1000 × 6 mm and is in steel. The acoustic data for the plate 1 have been already presented in [7] and will serve as a way to demonstrate the improvement of the procedure. The acquisition process is globally the same to collect the data on the second plate: the transducer pair is moved by hand on the vertices of a regular grid. At every position, 10 measurements of the ultrasonic response are averaged to improve the signal quality. This operation is not critical in a laboratory environment, but it may be necessary in outdoor conditions, where the inspection robot shall operate, to alleviate the effect of external disturbances. The acquisition positions are also carefully recorded. In total, 108 measurements are collected on the plate 1, while this number increases to 117 for plate 2. We use two tonebursts of a sinusoidal wave at 100 kHz as the excitation. Moreover, the direct incident signal is smoothly removed from the data as it does not correspond to a reflection on an edge.

For each plate, we determine a wave propagation model as in eq. (1) and use $N = 20$ particles. To simulate a sweep of a plate by a robotic crawler, a sequence of measurements is selected from the database and is presented to the SLAM framework, with the theoretic displacement between grid cells used as odometry. Also, we add Gaussian noise on the odometry data: $\bar{\Delta r} \sim \mathcal{N}(\Delta r, (10^{-2}\Delta r + \Delta r_0)^2)$ and $\bar{\Delta\theta} \sim \mathcal{N}(\Delta\theta, (10^{-2}\Delta\theta + \Delta\theta_0)^2)$ with $\Delta r_0 = 10^{-3}$ m and $\Delta\theta_0 = 10^{-2}$ rad to simulate odometry uncertainty which may be limited due to the robot magnetic adherence and embedded accelerometers used to provide precise heading on a nearly-vertical structure, in a realistic scenario [7].

B. Echo Detection

First, we illustrate the echo-detection principle. We show, in Fig. 3.a), the measured acoustic signal for a position corresponding to 8 cm to the edges, in a corner of plate 1. On b), we show the resulting correlation signal computed using eq. (2) and its envelope calculated with eq. (3), yielding the signal which is

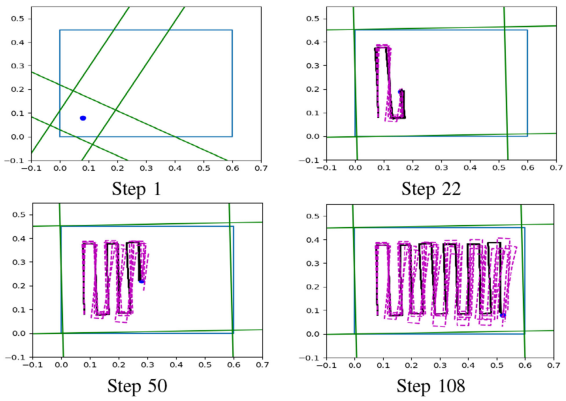

Fig. 4. Trajectories estimated by all the particles (black lines), dead-reckoning trajectories (dash magenta lines) and map retrieved by the most likely particle (green lines) during Steps 1, 22, 50 and 108 for a lawn-mower path on plate 1 (zoom for details). The true outline of the plate and true sensor positions correspond to the blue rectangle and blue dot respectively.

fed to the FastSLAM algorithm. It can be seen on b) that we manage to retrieve, from the local maxima, all the distances where first-order reflections occurred which are 8, 37 and 52 cm. The echo detected at nearly 45 cm corresponds to a higher-order reflection, but still has an amplitude that is comparable to that of the first-order wave packets. The existence of such a reflection is not assumed by the algorithm. Hence, we will determine a posteriori if their presence has a detrimental effect on the results.

C. Localization and Mapping Results

We run our FastSLAM algorithm using the data of plate 1, and simulate a lawn-mower path. Although the results are generated off-line, our method can run online on a real robotic platform. Indeed, as the beamforming maps of size $Z \times Z$ are updated incrementally, the complexity of one FastSLAM iteration with N particles is $\mathcal{O}(N \times Z^2)$, which leads to a computational time of a few tens of milliseconds per iteration in our setup, with $Z = 300$ and $N = 20$.

In Fig. 4, we show the particles' belief on the sensors trajectory during measurement steps 1, 22, 50 and 108. We also represent the map retrieved by the particle with the highest weight and several dead-reckoning trajectories obtained using noisy odometry input only. During Step 1, the map is not correctly estimated. As only one measurement has been integrated, the distance to the closest edge can be recovered but, the orientation is essentially random. Rapidly, the three closer edges are recovered as shown during Step 22. However, the right edge is not yet well estimated as it is further away. During Step 50, the plate shape is fully recovered, and during the final step, both the estimation of the plate shape and trajectory are accurate. In contrast, the dead-reckoning trajectories present noticeable drift. This illustrates that, by relying on the acoustic data, the proposed approach can appropriately compensate for moderate odometry noise.

Fig. 5 depicts the beamforming map for the most likely particle during the final step. We can see that the intensity peaks due to the edges are clearly visible, and our optimization method does not face difficulty to retrieve them.

To compare our new FastSLAM approach with the previous one, we show, in Fig. 6, the average localization and line parameters estimation errors calculated over 100 runs of each

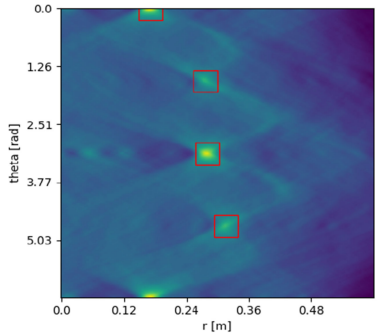

Fig. 5. Beamforming map for the particle with the highest weight during the final step. The rectangles indicate the edges retrieved with our method.

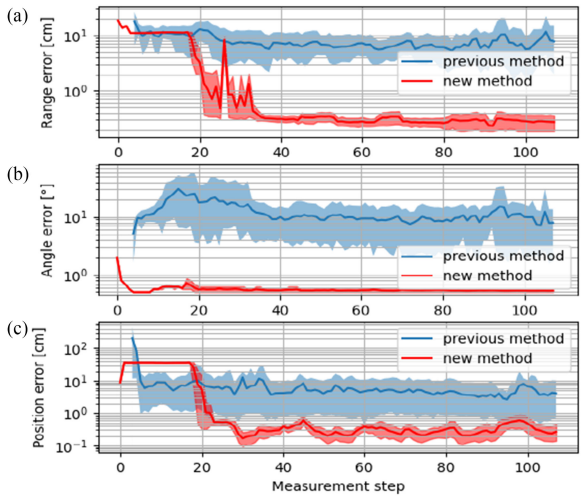

Fig. 6. Localization and mapping results over 100 repetitions of a lawn-mower path on plate 1 for the previous and the new method. a) Average estimation errors on the range parameter of the lines. b) Average estimation errors on the angle parameter. c) Average localization errors in the estimated plate frame. The 10% and 90% quantiles correspond to the upper and lower bounds of the coloured areas. The scales along the y-axis are logarithmic.

algorithm, and using the same acoustic data on plate 1. We simulated 100 repetitions of the lawn-mower path for the sensors trajectory. In the figure, we represent the 10% and 90% quantiles with the aim to measure the repeatability of each approach. It can be observed that, with our new method, only a few tens of measurement steps are necessary to recover, in average, the range parameters of the lines with a precision of a few millimeters, and the plate orientation with a precision better than one degree. The localization result is also very precise as, after a quick convergence, the position errors remain in the order of a few millimeters despite the defects on the plate. Besides, the estimation is not subject to randomness as the 10% and 90% quantiles remain close to the average results. In comparison, our previous method demonstrates poorer results. Indeed, not only are the estimation errors higher, but also the variation of precision can be relatively significant between two runs. Altogether, the results illustrate the improvement of localization and mapping that is achieved by our new method.

With the aim to assess the results for a larger plate, we run our algorithm with the measurements obtained on plate 2, and simulate again a lawn-mower path. The results obtained over 100 runs are provided in Fig. 7. On this plate, the echo

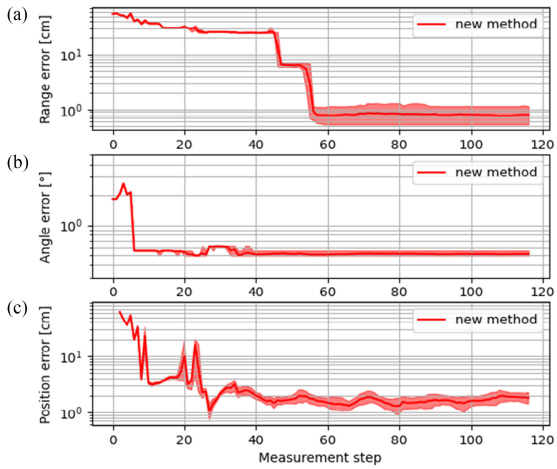

Fig. 7. Localization and mapping results over 100 repetitions of a lawn-mower path on plate 2 for the new method. a) Average estimation errors on the range parameter of the lines. b) Average estimation error on the angle parameter. c) Average localization errors in the estimated plate frame. The 10% and 90% quantiles correspond to the upper and lower bounds of the coloured areas. The scales along the y-axis are logarithmic.

Scenario	Range error [mm]	Angle error [degree]
Scenario 1	3.007 ± 0.098	0.234 ± 0.0004
Scenario 2	10.766 ± 22.921	0.206 ± 0.134

Fig. 8. Average estimation errors and standard deviations on the lines parameters obtained during the last measurement step for the two scenarios in consideration. The errors are evaluated using 100 repetitions.

detection employed by our previous method is not efficient, as it does not consider the wave dispersion effect, whereas the propagation distances are larger. This induces large misdetection rates and poor results. Hence, we display only the results of our new approach. Despite the slower convergence caused by the larger surface, and the slightly higher localization error, our method still provides precise estimates of the trajectory and plate geometry. This result indicates that our approach still works on surfaces sufficiently large to be used for realistic applications. The underlying prerequisites are a wave propagation model and filter parameters that conveniently fit the acoustic measurements and on-the-field noisy conditions. Naturally, one may also expect longer convergence times when the plate surface increases, as the echo detection is expected to be efficient mostly for short ranges as shown in Fig. 7.a).

As a final evaluation, we determine the average mapping errors and standard deviations over 100 runs obtained during the final step for a lawn-mower path (Scenario 1) and a random walk (Scenario 2) on plate 1. Fig. 8 presents the results. It can be noticed that the overall results are relatively poorer for the random walk. This illustrates that the estimation accuracy also strongly depends on the robot path which shall be optimized for optimal reconstruction.

V. Conclusion

We have designed a new FastSLAM approach to achieve Simultaneous Localization and Mapping on metal plates by relying on ultrasonic guided waves. Comparing to our previous work, this method relies on wave propagation models and beamforming maps. Experiments carried on an undamaged and a damaged metal plate in a laboratory environment demonstrate that this new approach achieves better results in terms of accuracy and robustness with less algorithmic complexity. In future works, this method shall be adapted and tested in more realistic scenarios. Indeed, on a large metal structure in outdoor environments, more complex and noisy signals are expected due, for example, to inferior surface quality, to the presence of anti-fouling coating on the plates, to more complex plate geometries, or due to wave scattering caused by the welds which fix the different plates altogether. Furthermore, adaptive techniques shall be investigated to adjust the propagation model and filter parameters which may no longer be assumed known a priori. Also, a real robotic platform shall be used, and active-sensing strategies shall be investigated to recover the plate geometry efficiently.

References

[1] M. Montemerlo, S. Thrun, D. Koller, B. Wegbreit, "Fastslam: A factored solution to the simultaneous localization and mapping problem," in *Proc. 18th Nat. Conf. Artif. Intelli.*, 2002, pp. 593–598.
[2] W. Cailly and H. Walaszek, "Three dimensional ultrasonic imaging of mechanical components by inversion," in *7th edition of the International Symposium on AirCraft Materials*, 2018. Available: https://www.researchgate.net/publication/331985263_Three_dimensional_ultrasonic_imaging_of_mechanical_components_by_inversion_7_th_INTERNATIONAL_SYMPOSIUM_ON_AIRCRAFT_MATERIALS-Compiegne_France_2_Contents
[3] P. Huthwaite and F. Simonetti, "High-resolution guided wave tomography," Wave Motion, 2013.
[4] Z. Su and L. Ye, *Identification of Damage Using Lamb Waves: From Fundamentals to Applications*, 01 2009, vol. 48.
[5] M. Krekovic, I. Dokmanic, and M. Vetterli, "Echoslam: Simultaneous localization and mapping with acoustic echoes," in *Proc. IEEE Int. Conf. Acoustics, Speech Signal Process.*, 2016, pp. 11–15.
[6] F. Peng, T. Wang, and B. Chen, "Room shape reconstruction with a single mobile acoustic sensor," in *Proc. IEEE Glob. Conf. Signal Inf. Process.*, 2015, pp. 1116–1120.
[7] C. Pradalier, O.-L. Ouabi, P. Pomarede, and J. Steckel, "*On-Plate localization and mapping for an inspection robot using ultrasonic guided waves: A proof of concept*," in *Proc. Int. Conf. Intelli. Robot. Syst.*, 2020, pp. 5045–5050.
[8] B. D. Van Veen and K. M. Buckley, "Beamforming: A versatile approach to spatial filtering," *IEEE ASSP Mag.*, vol. 5, no. 2, pp. 4–24, Apr. 1988.
[9] P. Cawley and D. Alleyne, "The use of lamb waves for the long range inspection of large structures," *Ultrasonics*, 1996.
[10] Z. Su, L. Ye, and Y. Lu, "Guided lamb waves for identification of damage in composite structures: A review," *J. Sound Vib.*, vol. 295, no. 3, pp. 753–780, 2006.
[11] M. Zhao, W. Zhou, Y. Huang, and H. Li, "Sparse bayesian learning approach for propagation distance recognition and damage localization in plate-like structures using guided waves," *Struct. Health Monit.*, vol. 20, no. 1, Art. no. 1475921720902277.
[12] Q. Jianxi, F. Li, S. Abbas, and Y. Zhu, "A baseline-free damage detection approach based on distance compensation of guided waves," *J. Low Freq. Noise, Vib. Act. Control*, 2018.
[13] J. Steckel and H. Peremans, "Sparse decomposition of in-air sonar images for object localization," in *Proc. IEEE Sensors*, pp. 1356–1359, 2014.
[14] B. Fontaine and H. Peremans, "Determining biosonar images using sparse representations." *The J. Acoust. Soc. Amer.*, vol. 125, no. 5, pp. 3052–9, May 2009.
[15] E. Hong and C. Schaal, "Reverse engineering stiffened plates using guided wave-based nondestructive testing methods ," in *Health Monit. Struct. Biol. Syst. XII, T. Kundu*, Ed., *International Society for Optics and Photonics. SPIE*, 2018.
[16] H. Kuttruff, *Room Acoustics*, fourth edition, 2000.
[17] N. Quaegebeur, P. Masson, D. Langlois Demers, and P. Micheau, "Dispersion-based imaging for structural health monitoring using sparse and compact arrays," *Smart Mater. Structures*, 2011.

Ultrasonics 123 (2022) 106705

Contents lists available at ScienceDirect

Ultrasonics

journal homepage: www.elsevier.com/locate/ultras

Learning the propagation properties of rectangular metal plates for Lamb wave-based mapping☆

Othmane-Latif Ouabi [a,*], Pascal Pomarede [a], Nico F. Declercq [a,b], Neil Zeghidour [c], Matthieu Geist [c], Cédric Pradalier [a]

[a] International Research Lab Georgia Tech-CNRS, 2 rue Marconi, 57070 Metz, France
[b] Georgia Institute of Technology, Atlanta, GA 30332-0250, USA
[c] Google Research, Paris, France

ARTICLE INFO

Keywords:
Lamb waves
Acoustic mapping
Helmholtz equation
Optimal beamforming
Model learning

ABSTRACT

The inspection of sizeable plate-based metal structures such as storage tanks or marine vessel hulls is a significant stake in the industry, which necessitates reliable and time-efficient solutions. Although Lamb waves have been identified as a promising solution for long-range non-destructive testing, and despite the substantial progress made in autonomous navigation and environment sensing, a Lamb-wave-based robotic system for extensive structure monitoring is still lacking. Following previous work on ultrasonic Simultaneous Localization and Mapping (SLAM), we introduce a method to achieve plate geometry inference without prior knowledge of the material propagation properties, which may be lacking during a practical inspection task in challenging and outdoor environments. Our approach combines focalization to adjust the propagation model parameters and beamforming to infer the plate boundaries location by relying directly on acoustic measurements acquired along the mobile unit trajectory. For each candidate model, the focusing ability of the corresponding beamformer is assessed over high-pass filtered beamforming maps to further improve the robustness of the plate geometry estimates. We then recover the optimal space-domain beamformer through a simulated annealing optimization process. We evaluate our method on three sets of experimental data acquired in different conditions and show that accurate plate geometry inference can be achieved without any prior propagation model. Finally, the results show that the optimal beamformer outperforms the beamformer resulting from the predetermined propagation model in non-nominal acquisition conditions.

1. Introduction

During their lifetime, marine vessels are continuously deployed on the seas for goods shipping. This inexorably leads to the deterioration of the hull due, for example, to the formation of biofouling on the surface, or due to the salinity of the water that can favor the formation of defects such as cracks or corrosion patches. Other large metal structures such as storage tanks deteriorate over time due to their operational conditions, and the underpinning defects may not always be detectable with the bare eye [1]. Thus, in the marine and petrochemical industries, the inspection of large-scale metal structures – which are usually made of metal panels assembled out together – must rely on efficient solutions that can seamlessly integrate into their day-to-day operation.

Standard inspection methods are time-consuming as they often require the intervention of trained operators, causing a significant financial impact. Moreover, these methods work for localized inspection areas; thus, the entire surface cannot be inspected in a reasonable amount of time. For ship hulls inspection, for example, either human operators or robots such as magnetic crawlers [2] can apply acoustic probes on the structure surface to perform thickness measurements, and detect corrosion patches. However, only the surface directly covered by the probe is effectively controlled with a single measurement.

The inspection of structures over long ranges is being actively investigated in the literature. Lamb waves, in particular, are being integrated into modern Non Destructive Testing (NDT)-capable devices. These waves can be emitted in plate materials by piezoelectric transducers and can propagate radially over long distances in a direction parallel to the surface. What makes them appealing is that they are sensitive to material integrity. Usually, they are deployed on static networks of sensors that are permanently attached to the structure. Thus, defect detection and localization can be achieved through the triangulation of

☆ This work is part of the BugWright2 project. This project is supported by the European Commission under grant agreement 871260 - BugWright2.
* Corresponding author.
E-mail address: oouabi@georgiatech-metz.fr (O.-L. Ouabi).

https://doi.org/10.1016/j.ultras.2022.106705
Received 21 July 2021; Received in revised form 20 December 2021; Accepted 3 February 2022
Available online 17 February 2022

acoustic scatterers from residual signals [3–7], or by using baseline-free methods [8–11].

Besides, the interest in the development of a robotic system for long-range inspection is steadily growing, as it holds tremendous potential for industrial applications, and its feasibility is being demonstrated by recent works [12–14]. Yet, deploying acoustic imaging techniques on a robotic system necessitates precise localization of the transducers, which is critical for accurate inspection results. Contrary to standard Structural Health Monitoring (SHM) technology where the positions of the sensors are known accurately, these positions need to be estimated in the framework of a robotic application due to kinematics modeling errors, and due to the imprecise wheel displacement and rotation data provided by the wheels' encoders.

When induced by a source excitation, Lamb waves can reflect on the metal plate boundaries, usually without mode conversion when the excitation frequency is sufficiently appropriate [15]. As the resulting acoustic measurements contain such reflections, they provide range-only information between the source position and the plate edges which may be useful for accurate localization, in combination with other measurement systems. Lamb wave-based localization has been demonstrated for a pulse-echo setup on a rectangular and isotropic metal panel, but with prior knowledge of the structure geometry [16]. Hence, determining precisely the sensor position on a large structure is intrinsically connected to building a map of the environment (*i.e* mapping the environment) which can rapidly become a tedious task if not made automatically [17]. Furthermore, from a robotic perspective, defect detection and localization may be interpreted as a mapping problem as well. Overall, the mapping of acoustic scatterers (whether they be plate boundaries or defects) by a mobile unit is a major issue that needs to be addressed to enable the emergence of a viable robotic inspection system.

In the literature, the problem of defect detection and localization using acoustic reflections on the structure boundaries has been widely studied [18–21]. Furthermore, approaches to detect the boundaries of a rectangular panel [22], to identify structural features such as stiffeners [23], or to localize an acoustic source [24,25] have been investigated. Yet, they are deployed on static networks of sensors. A recent work [26] proposes a Lamb wave-based approach to map a rectangular metal panel using a pair of mobile sensors, along with an exploration strategy. Yet, the work is dedicated to pitch–catch configurations, the Time of Flights (ToF) readings are not done automatically, the mapping is only based on the edge echo that arrives first, and the final map may eventually be erroneous due to gridlock situations that are not predictable.

Recent works from the authors address Lamb wave based Simultaneous Localization and Mapping (SLAM), where the geometry of the plate and the position of a co-located emitter/receiver pair of piezoelectric transducers are jointly estimated. A method based on L_1-regularized Least-squares for echo detection and on a FastSLAM algorithm [27] has been presented in first instance [28]. Subsequently, propagation models to account for the dispersive nature of guided waves in metal plates and space domain Delay-And-Sum (DAS) beamforming [29] have been integrated into a FastSLAM algorithm for the exclusive mapping of rectangular shapes [30]. Results proved to be accurate on two different metal panels. However, no solutions were proposed to limit the detrimental effect of interference on the mapping results which is a well-known issue inherent to DAS beamforming [29]. Besides, the approach requires prior knowledge of the propagation model.

Prior knowledge of the physical properties of isotropic metal structures is in general sufficient for acoustic localization and mapping in well controlled environments. However, the hypothesis that the propagation model is known a priori may not be realistic for a practical inspection task on a large metal structure due to a wide variety of external perturbations that can significantly affect the acoustic signals, and to a lack of knowledge of the structure physical condition (which is the reason why it is being inspected). Potential perturbations may include but may not be limited to temperature variations which are already known to affect acoustic measurements substantially [31], pressure due to the neighboring metal plates which are welded altogether, moisture, the varying thickness of the coating, or the effect of the coupling (namely water in the case of acoustic inspection with a robotic system). Consequently, adaptive methods that automatically calibrate the propagation model by relying directly on data acquired on the field may be necessary to achieve accurate localization and mapping results, without any human intervention.

Recent works in the literature either address the problem of extracting the dispersion characteristics of materials from ultrasonic data [32–35], or investigate acoustic localization techniques that can also recover the propagation properties [25,36,37]. However, simultaneous acoustic localization and propagation characterization from pulse-echo ultrasonic measurements acquired by a mobile unit has not been thoroughly studied. In the literature of beamforming, adaptive methods have been elaborated to compensate for inaccurate knowledge of the properties of the propagation media for underwater acoustic source localization purposes [38], or more generally, for Matched Field Processing [39]. Beamforming has been combined with focalization [40], an approach that considers the propagation environment as an acoustic lens, and which seeks, through an optimization process, to adjust the propagation parameters so that the focalization capability of beamforming is maximized. It has also been studied for joint acoustic signal separation and source localization [41]. The potential of focalization has been successfully demonstrated in simulation for underwater acoustic localization, and may provide an interesting approach for Lamb waves. Yet, this has not yet been demonstrated.

This paper proposes an approach that combines focalization and DAS beamforming to achieve Lamb wave-based mapping of a plate-like structure by a mobile unit, so that accurate mapping results can be achieved during an inspection task without prior knowledge of the propagation properties of the material. For the sake of simplicity, the localization problem is not addressed here. The proposed approach combines focalization to adjust the parameters of propagation models that are derived from the Helmholtz equation, and beamforming to localize the plate edges. The focalization capability of a candidate beamformer is assessed over high-pass filtered beamforming maps, so that the detrimental effects of interference and high-order reflections are lowered. A simulated annealing optimization process is then implemented so that the optimal beamformer can be recovered based directly on data. Results acquired on experimental data in three different scenarios show that the proposed approach is effective. Furthermore, mapping the plate geometry with the optimal beamformer is found to be more efficient than mapping with a predetermined propagation model in non-nominal acquisition conditions.

The outline of the present article is as follows. First, the general theory on Lamb waves propagation in metal panels is briefly presented. Next, the approach based on DAS beamforming for mapping the plate edges with a single mobile platform by leveraging the acoustic reflections is recalled. The choice of the propagation parameters to search for, namely, the plate thickness, the longitudinal and transverse velocities, is then discussed, and the simulated annealing process is presented. Finally, experimental results and discussions conclude the article.

2. Lamb wave-based mapping

In what follows, we briefly recall the essential principles of the theory on Lamb waves propagation in metal plates, namely, the Rayleigh–Lamb equations. We then introduce a simple propagation model based on approximate solutions of the Helmholtz equation to account for dispersive propagation under the hypothesis of a linear model and an isotropic material. Next, we summarize the mapping strategy to localize the plate boundaries based on a known propagation model and a space-domain delay-and-sum beamformer [30]. These elements will be the basis of the core contribution of this paper, which is plate mapping without prior knowledge of the propagation model.

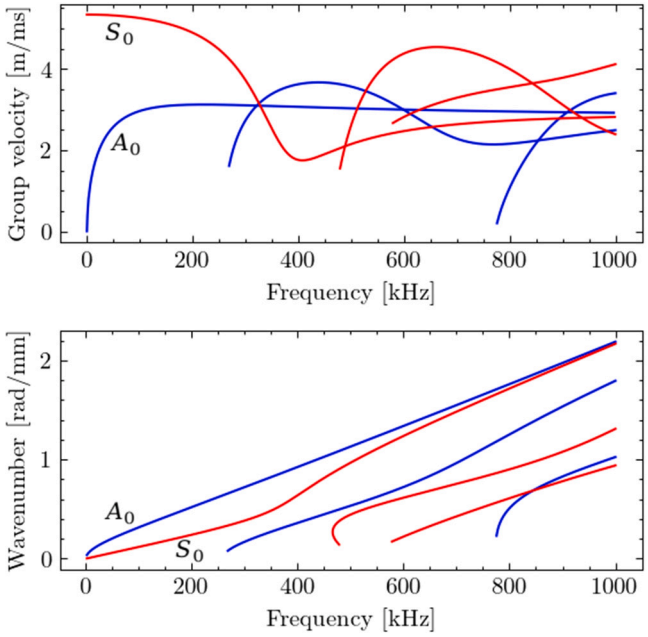

Fig. 1. Dispersion curves for several low order symmetric and anti-symmetric Lamb wave modes in a 6 mm thick aluminum plate. The top figure depicts the group velocities while the bottom plot shows the wavenumbers.

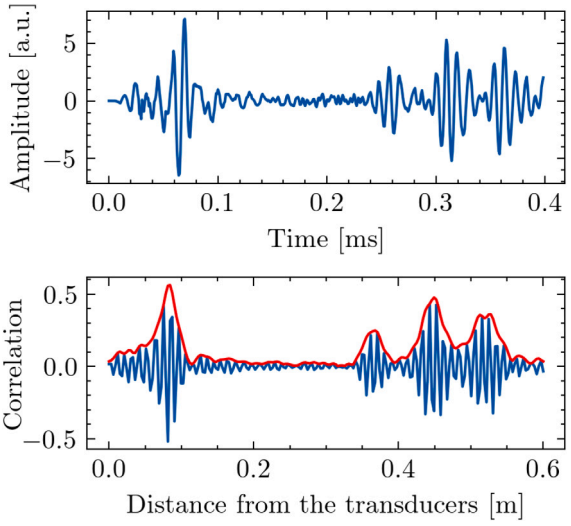

Fig. 2. Example of an acoustic signal acquired on an aluminum plate (top plot) and the correlation signal obtained from the measurement along with its envelope (bottom plot). The ranges relative to the first-order reflections (8, 37, 52 cm) can be successfully retrieved from the local maxima. The echo at nearly 45 cm corresponds to a higher-order reflection.

2.1. Lamb waves propagation in a metal plate

The theory on Lamb wave propagation in an isotropic and homogeneous wave guide is well established [42]. According to the Rayleigh–Lamb equations:

$$\frac{\tanh qh}{\tanh ph} = -\left[\frac{4k^2qp}{(k^2-q^2)^2}\right]^{\alpha} \tag{1}$$

where h denotes the half-thickness of the plate, $k = 2\pi/\lambda$ is the wavenumber, λ is the wavelength, and the following equations define p and q:

$$p^2 = \frac{\omega^2}{c_L^2} - k^2; \quad q^2 = \frac{\omega^2}{c_T^2} - k^2.$$

In the above equation, ω is the pulsation, and c_L and c_T are respectively the longitudinal and transverse velocities related to the material. For $\alpha = 1$, the equation yields the physical properties of symmetric modes, whereas for $\alpha = -1$, the properties of anti-symmetric modes are stipulated. The resolution of the equation, using dichotomy algorithms for example [3], yields a dispersion relation $k(\omega \cdot d)$ (or $k(\omega)$ for a fixed d), where $d = 2h$ is the plate thickness. One particularity is that each equation always admits at least one positive real-valued solution, and the number of solutions increases with frequency. Hence, at least the two fundamental modes A0 and S0 propagate within the material, while higher-order modes propagate when the excitation frequency exceeds their respective cut-off frequency. Fig. 1 depicts dispersion curves for symmetric and anti-symmetric modes for a 6 mm thick aluminum plate. In practice, a low excitation frequency is used to avoid multimodal propagation, and one mode is often predominant over the other fundamental mode. Also, as their velocities are frequency-dependent, these modes are dispersive, resulting in wavepacket distortion and spreading in the signal when the propagation distance increases.

Finite Element Methods (FEM) are often used to simulate Lamb waves propagation [43], but their heavy computational load makes them impractical to use for acoustic localization operations. Instead, one can rely on computationally efficient and relatively accurate propagation models given by the solutions of the Helmholtz equation, for which the wavenumber abides by the dispersion relation of the mode assumed to exist in the material. When a signal s is used to excite Lamb waves in a metal plate, under the hypotheses of linear propagation and isotropic media, the vertical component u of the displacement field abides by:

$$\nabla^2 u(r,\omega) + k^2(\omega) \cdot u(r,\omega) = -s(\omega)$$

where r is the propagation distance from the excitation point. It is known that the solution, *i.e.* the acoustic transfer function $g(r,\omega)$, can be expressed with the Hankel function of 0 order and of the first kind yielding the scalar field: $u(r,\omega) = g(r,\omega) \cdot s(\omega) = H_0^1(k(\omega)r) \cdot s(\omega)$. The transfer function is often simply reduced to:

$$\hat{g}(r,\omega) \approx \exp(-jk(\omega)r)/\sqrt{k(\omega)r}. \tag{2}$$

The use of this acoustic model is widespread in the literature of guided waves, primarily to achieve defect detection and localization purposes [44,45].

2.2. Space-domain beamforming for plate geometry inference with a single mobile unit

We are considering a mobile platform equipped with an emitter/receiver pair of piezoelectric transducers nearly co-located. At the ith scanning position, the emitter excites the Lamb waves in the plate material with the pulse $s(t)$. Simultaneously, the receiver collects the acoustic response $z_i(t)$ which contains the reflections on the plate boundaries, and it will be assumed that the excitation signal is chosen adequately so that the A0 mode is predominant (while the propagation of S0 is negligible). The objective is to infer the plate geometry and the sensors' acquisition positions in the plate frame. In robotics, this is known as a mapping problem because the displacement between each acquisition position (*i.e* odometry data) is assumed to be known flawlessly. Even though a solution for simultaneous localization and mapping has been proposed [30], the localization problem is disregarded in this paper for the sake of simplicity.

In the considered setup, the acoustic measurements essentially consist of a superposition of the acoustic reflections. Under the assumption that the material is homogeneous, isotropic and the propagation linear, a standard measurement model to reverberation is the image source model [46]. It states that each reflection from the plate boundaries can

be considered as a signal originating from a fictional source, deducted from the actual source position and reverberant media geometry. In metal plates, the image source model can be leveraged to account for first order as well as higher-order reflections, resulting in the following measurements in the time domain:

$$z_i(t) = \sum_{\mathbf{x}\in\mathcal{I}(\mathbf{x}_i)} g(|\mathbf{x}-\mathbf{x}_i|,t) * s(t)$$

where $\mathbf{x}_i = [x_i, y_i]$ is the position of the robot during time step i, $\mathcal{I}(\mathbf{x}_i)$ the set of the image sources positions when the real source is in $\mathbf{x}_i$, $g(|\mathbf{x}-\mathbf{x}_i|,t)$ the acoustic transfer function associated to the predominant A0 mode, and $*$ denotes the convolution operation. An example of a clean acoustic measurement acquired on an aluminum plate can be seen in Fig. 2, where the transducers have been placed on a 600 × 450 × 6 mm aluminum plate, and at 8 cm of the two edges of a corner.

To retrieve the ranges from the sensors to the plate edges from data $z_i(t)$, we determine the correlation signal:

$$z_i'(r) = \frac{\langle z_i(t), \hat{z}(r,t)\rangle}{\sqrt{\langle z_i(t), z_i(t)\rangle\langle \hat{z}(r,t), \hat{z}(r,t)\rangle}}$$

where $\hat{z}(r,t) = \hat{g}(2r,t) * s(t)$ is the expected signal for the incident wave reflecting at a distance r from the transducers, and $\langle .,. \rangle$ denotes the scalar product in the domain of continuous signals: $\langle u(t), v(t)\rangle = \int_{-\infty}^{+\infty} u(\tau)v(\tau)d\tau$. To alleviate the oscillations present in z_i', we retrieve its envelope $e_i(r)$ with:

$$e_i(r) = \left|z_i'(r) + j\mathcal{H}(z_i')(r)\right|$$

where $\mathcal{H}$ denotes the Hilbert transform operator. Thus, the resulting signal e_i yields the distances of the transducers to the metal plate edges with the position of its local maxima. This principle is illustrated in the bottom plot of Fig. 2. Besides, it is noteworthy that a single measurement cannot provide enough information to determine an edge without ambiguity, as all the lines tangent to the circle with radius r and centered at the position of the sensor may equally account for the correlation measurement.

The plate geometry to be recovered is represented by a set of lines: $\mathbf{M} = \{r_l, \theta_l\}_{l=1\ldots4}$ where the parameters (r_l, θ_l) define the line equation in the 2D plane with:

$$x\cdot\cos\theta_l + y\cdot\sin\theta_l - r_l = 0$$

in a non-mobile frame with respect to the plate, as illustrated in Fig. 3. The origin O of the reference frame can be taken as the initial position of the mobile unit while on the metal panel. Moreover, for convenience, the plate geometry is restricted to rectangular shapes.

Next, given a robot trajectory $\{x_i, y_i\}_{i=1\ldots N}$ (assumed to be flawlessly provided by odometry for the mapping problem), the beamforming map $\mathcal{L}_N$ is computed to assess the likelihood of existence of any line (r,θ) with:

$$\mathcal{L}_N(r,\theta) = \sum_{i=1}^{N} e_i(d_i(r,\theta)) \tag{3}$$

where $d_i(r,\theta) = |x_i\cdot\cos\theta + y_i\cdot\sin\theta - r|$ is the distance between the robot during measurement step i and the hypothetical line being considered. In the equation, all the correlation values add up constructively along with all the observations if an edge is indeed present. Also, it can be noted that only first-order reflections are taken into account, as we reason on individual lines. One major advantage of this approach is that $\mathcal{L}_N(r,\theta)$ can be computed recursively when an additional measurement e_N is made available, as $\mathcal{L}_N(r,\theta) = \mathcal{L}_{N-1}(r,\theta) + e_N(|x_N\cdot\cos\theta + y_N\cdot\sin\theta - r|)$. This is beneficial for a robotic task meant to be performed in real time, as a map estimate is available at any time, and the computational load of one update is low. Finally, to infer the most plausible plate geometry from $\mathcal{L}_N$, we solve the following optimization problem:

$$\hat{\mathbf{M}} = \arg\max_{\mathbf{M}} \mathcal{L}_N(\mathbf{M}) = \arg\max_{\mathbf{M}} \sum_{l=1}^{4} \mathcal{L}_N(r_l,\theta_l) \tag{4}$$

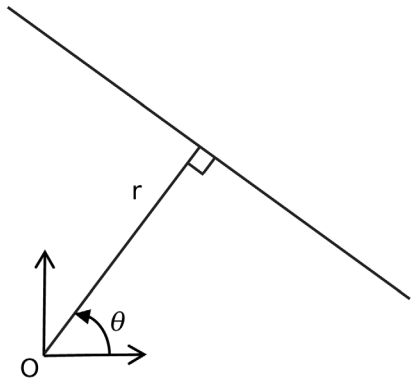

Fig. 3. Representation of lines in a 2-dimensional plane with (r,θ) coordinates.

where $\mathbf{M}$ is restricted to be a rectangle. It can be solved efficiently by taking that constraint into account. First, one can determine the most plausible line with:

$$(\hat{r}_1, \hat{\theta}_1) = \arg\max_{r,\theta} \mathcal{L}_N(r,\theta).$$

Next, assuming that $\hat{\theta}_1$ provides the most reliable estimation of the plate orientation w.r.t. the robot, the determination of the other lines reduces to solving independent and straightforward one-dimensional optimization problems:

$$\hat{\theta}_l = \hat{\theta}_1 + \frac{\pi(l-1)}{2} \;; \quad \hat{r}_l = \arg\max_{r} \mathcal{L}_N(r,\hat{\theta}_l)$$

for $l = 2,3,4$. Solving the plate geometry inference with this approach gives accurate results in laboratory conditions [30]. However, this approach has some limitations. The fact that an infinity of lines can equally account for one reflection causes interference, which is a well-known issue encountered when relying on standard DAS beamforming. The effect of interference is further exacerbated by the high order reflections which are not considered in Eq. (3), whereas their presence cannot be neglected as shown by Fig. 2-(b). The consequence is that beamforming maps are fuzzy, which can make the estimation ambiguous, as it will be illustrated later. Also, the method relies on prior knowledge of the propagation model g to obtain accurate results, whereas such a hypothesis may not be realistic for a practical inspection task in challenging outdoor environments, where the structure state is truly unknown.

3. Optimal beamforming for model learning

In this section, we present an adaptive method to recover a metal plate geometry without the assumption of a known model. It is based on focalization in the parameter space (*i.e.* the propagation model is adjusted) and beamforming for localizing the plate boundaries. First, the parametrization of propagation models using solutions of the Helmholtz equation is presented. Next, we introduce and apply a simple high-pass filter to the beamforming maps to limit the detrimental effect of interference and high-order reflections. A loss function is then designed to assess the focusing capability of a candidate beamformer which should maximize spatial coherency (*i.e.* the energy that is focused at the geometry estimate on the beamforming map) in the case when the propagation model is appropriate. Finally, an optimizer based on simulated annealing [47] is presented to recover optimal propagation parameters by minimizing the loss in a limited number of iterations. The efficiency of such an approach has been successfully demonstrated for underwater source localization purposes [40,41].

3.1. Parametrization of the propagation model

With the hypothesis of linear and isotropic propagation, we aim at recovering both a propagation model $\hat{g}(r,t)$ and the plate geometry expressed as a set of lines $\hat{\mathbf{M}} = \{\hat{r}_l, \hat{\theta}_l\}_{l=1..4}$.

For candidate propagation models, we keep relying on the (approximate) solutions of the Helmholtz equation. Hence, estimating the propagation model reduces to the estimation of only three parameters which are the longitudinal velocity c_L, the transverse velocity c_T and the plate thickness d, and that we will gather in the variable $\Omega = \{c_L, c_T, d\}$. This choice is convenient as we constrain the propagation models to be physically plausible while limiting the search space for the propagation model parameters to a low dimension, which will facilitate the optimization process. As the complete state of the structure may be unknown during the inspection, adapting these wave parameters may be relevant. Indeed, plate thickness may not be known accurately for each surface plate as the structural integrity is unknown. Besides, the effects of variation of temperature, pressure, moisture may be interpreted as variations of the effective velocities. For more complex sources of disturbances such as the effect of coupling or structure irregularities, we are not seeking to strictly compensate for their effect with such a simple model, yet sufficiently enough to predict the plate boundaries location accurately. Next, given candidate values Ω for the model parameters, the dispersion equation for the A0 mode given in Eq. (1) is numerically solved and is used to infer the propagation model $\hat{g}_\Omega(r,t)$ with Eq. (2).

3.2. Design of the loss function

Compared to plate geometry reconstruction with a known propagation model, inferring the plate geometry and propagation parameters simultaneously requires the determination of a larger number of unknowns. Consequently, an appropriate loss function that ideally prevents irregular cost surfaces with many local minima is needed to facilitate the optimization process.

Here, we introduce a loss function to assess the ability of a candidate beamformer (related to candidate parameter values Ω) to focus the energy of the wave packets contained in the measurements at the plate geometry estimate so that minimizing the loss function w.r.t. the model parameter search space improves the spatial coherency achieved with the beamformer. For candidate propagation parameters, the beamforming map $\mathcal{L}_\Omega(r,\theta)$ is constructed as in Eq. (3), allowing a plate geometry estimate $\hat{\mathbf{M}}_\Omega$ to be retrieved from it with the same optimization process as in Eq. (4). We then evaluate the total energy focused at the estimate $\hat{\mathbf{M}}_\Omega$ over the beamforming map that has been high-pass filtered to limit the effect of interference and high-order reflections. The filtered map value at each line (r,θ) is simply defined by the difference between its initial energy value and the minimum of energy in its vicinity that is to be appropriately defined:

$$\tilde{\mathcal{L}}_\Omega(r,\theta) = \mathcal{L}_\Omega(r,\theta) - \min_{(r',\theta')\in V(r,\theta)} \mathcal{L}_\Omega(r',\theta'). \tag{5}$$

where $V(r,\theta)$ refers to the set of lines in the vicinity of (r,θ). Compared to the standard $\mathcal{L}_\Omega(r,\theta)$, the filtered map $\tilde{\mathcal{L}}_\Omega$, while being inexpensive to compute, has the advantage to present fewer areas where the intensity is high but homogeneous (such a situation occurs due to the combination of high-order reflections and interference). Hence, it is more compatible with Eq. (4) for the determination of the location of the edges. Thus, using Eq. (5) may appropriately filter "fuzzy" areas where the energy is spread homogeneously (*i.e.* not focused at a single point) due to interference on the beamforming maps, and may isolate correct intensity peaks. This will be illustrated next with experimental data.

To simultaneously recover propagation parameters and the plate geometry, performing a joint search in both the propagation model space and the geometry space would be computationally expansive. Instead, we rely on an optimal beamforming formulation: the loss is only evaluated over candidate model parameters Ω, and for the corresponding geometry estimate $\hat{\mathbf{M}}_\Omega$ retrieved *from the high-pass filtered beamforming map* $\tilde{\mathcal{L}}_\Omega$ with Eq. (4). The loss value $l(\Omega)$ that we will seek to minimize is then taken as minus the sum of the intensity levels evaluated at the retrieved edges:

$$l(\Omega) = -\sum_{(r,\theta)\in\hat{\mathbf{M}}_\Omega} \tilde{\mathcal{L}}_\Omega(r,\theta) \tag{6}$$

so that the energy focused at the plate geometry estimate can be maximized, while the detrimental effects of interference and high-order reflections can be minimized. The geometry estimate provided by the optimal beamformer is expected to match closely the ground truth geometry due to the maximum of spatial coherency as long as measurements have been acquired on a sufficient portion of the plate surface. Besides, to highlight the benefit of using high-pass filtered beamforming maps, propagation model selection based on the loss evaluated using the regular beamforming map $\mathcal{L}_\Omega(r,\theta)$ will also be carried out in the following sections, and the mapping results will be compared.

3.3. Optimization with simulated annealing

An optimization process is needed to adjust the wave propagation parameters (longitudinal and transverse velocities and the plate thickness) through the minimization of the loss function. Due to the implicit definition of the propagation models, first-order methods such as gradient descent are impractical to use for our problem.

Simulated annealing [47] is efficient for estimating a global minimum of a cost function, even when the number of unknowns is large [41]. This metaheuristic is inspired from metallurgy where, to form a perfect crystal (which corresponds to the state of minimal energy), a pure liquid substance is slowly cooled. At each iteration of the optimization process, a random perturbation is applied to the current point value. The perturbation is systematically accepted if the energy is decreased. To escape local minima, the perturbation is accepted according to a Boltzmann probability distribution if the energy is increased. The temperature, which is a hyperparameter, is decreased slightly after each iteration so that the probability to increase the energy goes to zero. Hence, the major controllable parameters of simulated annealing are the distribution of the perturbation and the profile of the temperature cooling.

For Lamb-wave based mapping without a prior propagation model, the parameter search is reduced to the optimization over the value of Ω as the geometry is directly deduced using Eq. (4) when Ω is fixed. Our implementation of the optimizer is similar to that used in articles related to the underwater localization problem [40]. The major difference lies in the cost function design. First, we initialize the propagation parameters with uniform distributions within predefined intervals which are plausible regarding the application:

$$c_L^0 \sim \mathcal{U}([c_{\min}, c_{\max}]); \quad c_T^0 \sim \mathcal{U}([c_{\min}, c_L^0 - m])$$
$$d^0 \sim \mathcal{U}([d_{\min}, d_{\max}]).$$

The value of c_T is drawn below the value of c_L, with a small margin $m > 0$, as it cannot physically be higher (*i.e* there are no positive real-valued solutions to the Rayleigh–Lamb equation).

At each iteration of the algorithm, the parameters are randomly disturbed using the following perturbations:

$$c_L^{t+1} = \min\left\{\max\{c_L^t + \Delta c \cdot \chi_0^3, c_{\min}\}, c_{\max}\right\}$$
$$c_T^{t+1} = \min\left\{\max\{c_T^t + \Delta c \cdot \chi_1^3, c_{\min}\}, c_L^{t+1} - m\right\}$$
$$d^{t+1} = \min\left\{\max\{d^t + \Delta d \cdot \chi_2^3, d_{\min}\}, d_{\max}\right\}.$$

Using the min–max formulation enables to leverage prior information by constraining the parameter values within plausible intervals. Similarly to the initialization step, c_T^{t+1} is restricted to be lower than c_L^{t+1} with the same margin m. χ_0, χ_1, χ_2 are independent random values between -1 and 1, and are drawn from uniform distributions: $\chi_{1,2,3} \sim$

$\mathcal{U}([-1,1])$. They are raised to power 3 so that small variations are more likely. Still, large variations can be possible to explore regions of the search space that are far occasionally when the values of Δc and Δd are chosen to be large enough.

Next, for the new parameter values Ω^{t+1}, the dispersion relation $k_{\Omega^{t+1}}(\omega)$ is determined by solving the Rayleigh–Lamb equations. As the relation is computed numerically at each iteration of the optimization process, the computational load can be quite demanding. A trick to save computational time is to determine the wavenumber only for a restricted set of pulsation values $\omega_1, \ldots, \omega_K$ and to use linear interpolation to determine the wavenumber for other frequencies.

Next, the acoustic transfer function $\hat{g}_{\Omega^{t+1}}(r,\omega)$ is determined with the Helmholtz model given in Eq. (2). The beamforming map $\mathcal{L}_{\Omega^{t+1}}(r,\theta)$ is then computed and a plate geometry estimate $\hat{\mathbf{M}}_{\Omega^{t+1}}$ is retrieved from it, allowing the determination of the loss value $l(\Omega^{t+1})$ with Eq. (6).

The variation of energy between the previous and disturbed parameters is $\Delta E = l(\Omega^{t+1}) - l(\Omega^t)$. In the context of simulated annealing, the disturbed parameter value is not systematically kept. It is the case only when:

$$\chi < \exp\left\{-\frac{\Delta E}{\gamma T}\right\}$$

where γ is a strictly positive scaling parameter, T is the temperature at the iteration t, and χ is drawn randomly and uniformly between 0 and 1. Consequently, when the energy is decreased, the disturbed parameters are systematically kept. Otherwise, the acceptance rate is given by the Boltzmann distribution which yields lower acceptance rates for more significant increases of energy. The temperature parameter is often chosen to decrease inverse logarithmically. To enable fast convergence of simulated annealing, we will decrease the temperature inverse linearly. Trials and errors are used to determine appropriate parameters for the optimizer: the values that empirically demonstrate a lower likelihood for the optimizer to be stuck in local maxima while maintaining a sufficient convergence speed are retained.

As it has already been highlighted, the cost function may be heavy to assess, in particular when the number of considered measurements is high. Indeed, each iteration of the optimizer requires solving the Rayleigh–Lamb equation for a set of frequency values, then computing the beamforming map using the N measurements, and recovering a plate geometry estimate with the optimization. For a robotic application, a few seconds might be needed to achieve convergence with around 100 measurements and using a linear decrease of the temperature. Thus, our method cannot be used in real time. Yet, this is not an issue, as it could be considered, during a practical robotic inspection task, to stop the robot for a few seconds to run the optimizer occasionally, and restrict the maximum number of acoustic measurements used to perform the optimization.

4. Experimental setup

We test our approach on experimental acoustic data that have been acquired in three different scenarios. To generate the datasets, an emitter/receiver pair of contact piezoelectric V103-RM U8403008 transducers is moved at different positions on the plate surface, in each scenario. These transducers are used because, at the time of the experiment, it was the best solution available to the authors to generate and receive Lamb waves, although it may not be optimal. During the acquisition, the transducers are placed one beside the other to approximate a pulse-echo setup. The excitation signal used to emit the waves in the material corresponds to two tone bursts of a sinusoidal wave at 100 kHz, with an amplitude of 100 V peak to peak. This frequency is chosen as it has been experimentally observed that the predominant propagation mode was A0 for all the scenarios, and the others modes are almost nonexistent. It is to be noted that, in our experiments, two different transducers are used, whereas our method is based on a point-like and co-located emitter–receiver assumption

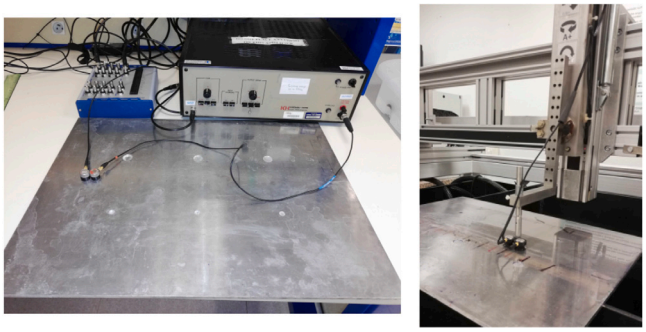

Fig. 4. Pictures showing the experimental setups for Scenario 1 (left) and Scenario 3 (right).

that we assimilate to the center between the transducers. This is not a significant problem as the diameter of the transducers (1.7 cm), and thus the distance between their centers is not large compared to the wavelength (2 cm) for the considered excitation frequency. Thus, the difference induced by this setup has negligible impact on the signals.

Different operations are performed next on the measurements. For Scenario 1 and 2 only, 10 scans are acquired per acquisition position and are averaged to improve the signal-to-noise ratio. This operation is performed although it is not critical in a laboratory environment. In addition, the high frequencies (>400 kHz) of the signals are filtered out. Also, the equivalent of twice the excitation duration is smoothly removed at the beginning of each measurement with a sigmoid window. Indeed, it is not desirable to keep the first wave packet resulting from the direct transmission of the excitation between the emitter and the receiver, as it does not correspond to a reflection on a plate boundary. The counterpart is that transducers cannot be brought closer to an edge than the dead-zone distance (which amounts here to 2 to 4 wavelengths), otherwise, the first reflection on it would be removed as well.

For Scenario 1, the transducers are moved by hand on an aluminum plate of size 600 × 450 ×6 mm that contains artificial holes of different thicknesses and depths as shown in Fig. 4. In total, $N_1 = 108$ measurements are acquired, each of them containing $M_1 = 500$ samples collected at a sampling rate of 1.25 MHz. The signals are acquired with a National Instruments USB 6356 data acquisition device. For Scenario 2, the data is collected with an oscilloscope on a steel plate of dimensions 1700 × 1000 × 6 mm. With these data, we can test our approach on a different material and show that it is still applicable to a larger surface. A total of $N_2 = 117$ measurements are collected with a sampling frequency of 6 MHz. The total number of samples per measurement is $M_2 = 5000$. For Scenarios 1 and 2, the transducers are in contact with the surface during the acquisition. Coupling gel is placed at their interface to ensure a good coupling. For Scenario 3, the data are acquired on the same plate as the one used for Scenario 1. However, a thin layer of water of approximately 1 mm of thickness is put all over the plate surface, and the transducers are not placed in contact with the plate surface during the acquisition, but are kept in contact with the water only. The acquisitions are performed using a customer-design five axes immersion scanner made by Inspection Technology Europe BV. It is also used to place the transducers (that are kept one beside the other) at specific positions on the measurement grid while maintaining a constant distance between the plate surface and the transducers. Due to the plastic holder, the distance between the centers of the transducers rises to 2.5 cm which is not an issue, as the distance is not large comparing to the wavelength. For this scenario, a total of $N_3 = 108$ measurements are collected at the same positions than those used for Scenario 1, the sampling frequency is 1.25 MHz, and the number of samples per measurement is $M_3 = 500$. The data acquired in this setup are expected to be representative of those that would

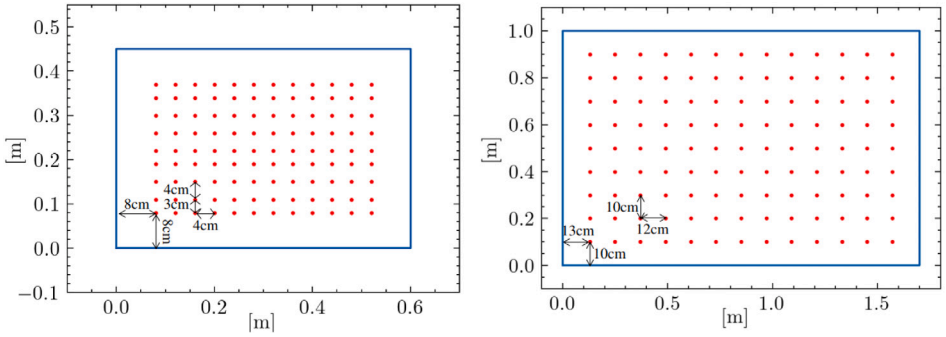

Fig. 5. Acquisition positions on the aluminum plate for Scenarios 1 and 3 (left), and on the steel plate for Scenario 2 (right).

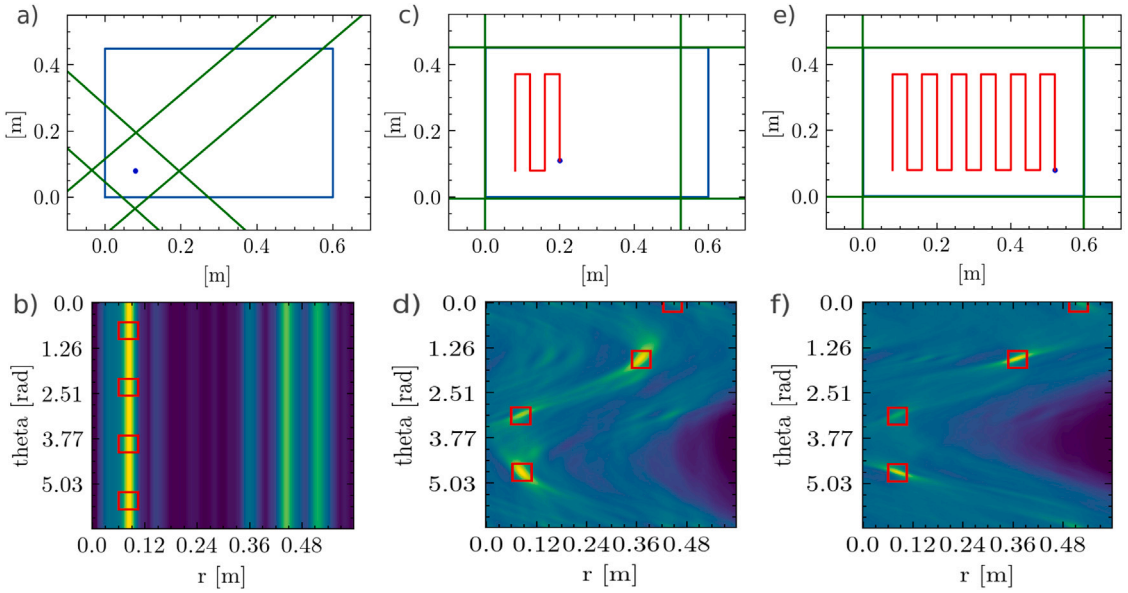

Fig. 6. Mapping results based on the standard DAS beamforming with a predetermined propagation model at different steps of a simulated lawn-mower trajectory in Scenario 1. Measurements steps 1, 35 and 108 correspond to figures (a), (c) and (e) respectively where the geometry estimate is represented by the straight lines. The corresponding beamforming maps are given in figures (b), (d) and (f) along with the retrieved edges indicated by the rectangles.

be acquired on a real structure by the robotic system, where water may also be used as coupling, and where the transducers may not be directly in contact with the structure surface to avoid damaging them by surface irregularities. Furthermore, this scenario will also allow us to highlight the potential of our approach in a slightly "disturbed scenario" comparing to the nominal acquisition conditions of Scenarios 1 and 2. Pictures of the experimental setups are available in Fig. 4, and all the acquisition positions are provided in Fig. 5.

In the next, we do not assume any imprecision on the sensor displacements. Indeed, Simultaneous Localization and Mapping has been studied elsewhere [28,30], and the method presented here is expected to integrate these frameworks conveniently.

5. Results

This section illustrates the efficiency of our approach for mapping a rectangular metal panel using ultrasonic guided waves in the three aforementioned scenarios. The benefit of filtering the beamforming maps is first discussed and highlighted based on the experimental data. Next, the correlation between the designed loss function and the reconstruction error is numerically assessed. The optimizer designed in the previous section is run to simultaneously infer the plate geometry and recover the propagation model. The resulting precision is compared with that obtained using a predetermined propagation model that will be used as a baseline. The overall results demonstrate that this target objective is successfully achieved with our method in nominal acquisition conditions (Scenarios 1 and 2). Our approach is also tested in slightly disturbed conditions (Scenario 3) to illustrate that it remains efficient. The results are obtained using the full batch of measurements in each scenario, which would amount to having the robot covering an important portion of the plate surface before calibrating the propagation model. As this may not be a representative scenario, the efficiency of our procedure is also assessed with simulated robot paths with acquisition points that are more sparse, and with a varying number of measurements available during the calibration.

5.1. Mapping with a predetermined propagation model

In Fig. 6, we show the mapping results for a lawn-mower trajectory simulated with the data from Scenario 1, and during measurement steps 1, 35 and 108. The geometry estimates are determined at each measurement step from the standard beamforming maps derived with Eq. (3), and based on a predetermined propagation model which is built using Eq. (2) and predetermined model parameters ($d = 6$ mm, $c_L = 6420$ m/s and $c_T = 3040$ m/s for our aluminum plate which were validated by comparing the theoretical and experimental dispersion curves). It can be observed that, initially, only the range to the closest edge is retrieved, but the orientation estimate is essentially random as only a single measurement has been integrated. During Step 35, three plate edges are correctly recovered but it is not the case of the

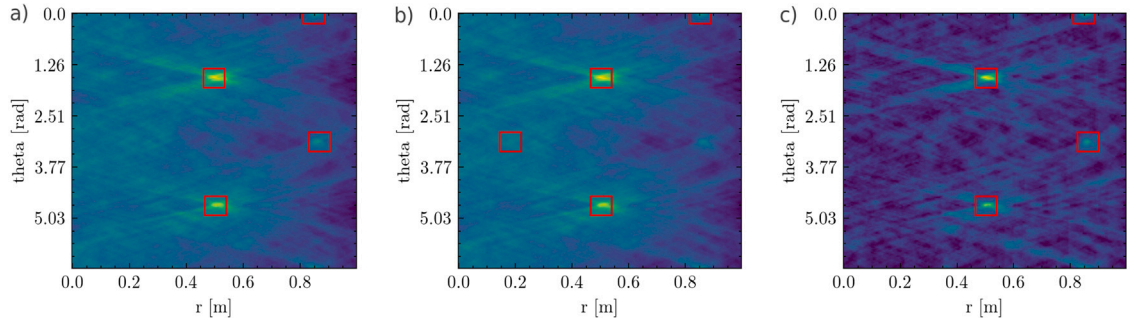

Fig. 7. Different beamforming maps computed using the data from Scenario 2 and the retrieved edges. (a) shows the standard beamforming map, which yields correct estimates. (b) depicts the map obtained with the same data sub-sampled in time. One edge is not correctly estimated. (c) shows the high-pass filtered beamforming map obtained from the sub-sampled data. The correct plate geometry is recovered, while the fuzzy areas due to interference and higher-order reflections have been partially filtered out.

right boundary as it is further away. Eventually, the geometry is fully recovered during Step 108, when all the available measurements have been integrated. The final average reconstruction error is less than one degree for the orientation, and the average estimation error is 0.15 cm for the lines range parameters. Overall, these results illustrate the efficiency of space-domain delay-and-sum beamforming combined with our grid search method for mapping the plate geometry with a propagation model based on prior knowledge of the mechanical properties of the material. This method is efficient despite the artificial holes that are present in the plate.

We now perform the experiment using all the measurements acquired on the larger steel plate (Scenario 2). This time, the parameters for the propagation model are $d = 6$ mm, $c_L = 5880$ m/s and $c_T = 3250$ m/s. The beamforming map shown in Fig. 7-(a) depicts two visible intensity peaks. The two other peaks are much less visible due to their lower intensity, and can be easily mistaken with interference and high-order reflections which cause areas of homogeneous intensity. Although the estimation is correct in this case (the average range error for the line estimation is approximately 0.5 cm), it may not be robust. To illustrate this, we sub-sample in time the data by a rate of 4 and reconstruct the beamforming map using the same propagation model. The results can be seen in Fig. 7-(b). The beamforming map is very similar. However, all but one line are still correctly recovered, causing the average error on the estimation of the line ranges to rise to 17 cm as the ambiguity is too important. Using high-pass filtered beamforming maps may increase the robustness of the estimate as described earlier. Such a map is shown Fig. 7-(c) where $V(r,\theta)$ is chosen as the rectangular area centered at (r,θ) with a size $6.5\text{ cm} \times 24°$. This window is sufficiently large to encompass the intensity peaks on the beamforming map, and sufficiently limited to make the filtering effective. When relying on the filtered version of the beamforming map, the estimation is made correct (the range error is again 0.5 cm), even though we cannot completely alleviate the effect of interference and higher-order reflections. Hence, the filtering may provide additional robustness which is to be leveraged to calibrate the propagation model. It may be even more useful in the presence of disturbances during the acquisition, as will be illustrated in the following.

5.2. Correlation between the loss and the geometry estimation error

We assess whether the designed loss is sufficiently correlated with the reconstruction error to ensure that its minimization yields an accurate plate geometry estimation. We create a family of 40 propagation models based on the approximate solutions to the Helmholtz equation Eq. (2) with values of $\Omega = \{c_T, c_L, d\}$ uniformly distributed within the intervals $c_T, c_L \in [2500\text{ m/s}, 6500\text{ m/s}]$ and $d \in [3\text{ mm}, 7\text{ mm}]$. Then, we determine the filtered beamforming map using each model to obtain a plate geometry estimate in each of the three scenarios under consideration. The results are displayed in Fig. 8 as plots of the reconstruction error (both in range and orientation) w.r.t. the loss value. We also display the same plots using the geometry estimates and loss values obtained without the filtering, for comparison. Ideally, we would obtain reconstruction errors that would monotonically decrease with the loss value.

For both Scenarios 1 and 2 in Fig. 8-(a)–(d), we observe that the range errors globally diminish for lower loss values. It can also be observed that models with close loss values can yield completely different reconstruction errors, or that models with high loss values can provide an accurate estimate (*e.g* the plot of the range error in Fig. 8-(c)). Yet, these tendencies are not critical, as the major requirement for our approach to be effective is that the best estimation results are achieved for the lower losses as this is what will be minimized. The variations of the orientation error present a different aspect. There is no strict decrease in the error for lower losses. Also, the discretization of the orientation value is visible due to the resolution of the beamforming map that is limited for the sake of computational efficiency. Yet, it is still possible to achieve an accuracy in the order of one degree, which is sufficient for our application. Also, the limited resolution is not a significant problem for propagation model learning, as the best accuracies are also achieved for the lower loss values.

We notice a slightly more divergent behavior for the two losses in Scenario 3, which corresponds to our slightly disturbed scenario. Regarding Fig. 8-(f) where the beamforming maps are not filtered, the reconstruction error presents a tendency to decrease for lower loss values. However, the minimum reconstruction error is achieved for a loss value of approximately $l(\Omega_{\min}) = -86$, and it becomes higher for lower losses. This is not the desired behavior, as it would result in poorer estimation results if the loss minimization is effective. This tendency is not visible when the loss values and the geometry estimates are obtained from the high-pass filtered beamforming maps (Fig. 8-e), where the lowest reconstruction errors are globally obtained for the lower losses. Hence, these results support the benefit of high-pass filtering the DAS beamforming maps for mapping and propagation model adaptation. It provides additional robustness due to its ability to lower the detrimental effect of high-order reflection and interference.

5.3. Model learning and plate mapping in nominal acquisition conditions

To assess the performance of our approach for optimal beamforming for Lamb wave-based mapping, we run it 10 times for Scenario 1 and 2, with random initial parameter values for each repetition. The simulated annealing is set with the following parameters: $\Delta c = 7000\text{ m/s}, \Delta d = 2\text{ cm}, c_{\min} = 1500\text{ m/s}, c_{\max} = 8000\text{ m/s}, m = 500\text{ m/s}, \gamma = 1$, $T = T_0/t$ where $T_0 = 200$, $d_{\min} = 3$ mm and $d_{\max} = 1$ cm. Besides, the performance of our approach is compared with the results achieved when using predetermined propagation models based on prior knowledge of the plate thickness, the longitudinal and transversal velocities in nominal conditions. These predetermined models will serve as a baseline for comparison. Fig. 9 depicts the evolution of the minimum loss value and the corresponding reconstruction errors

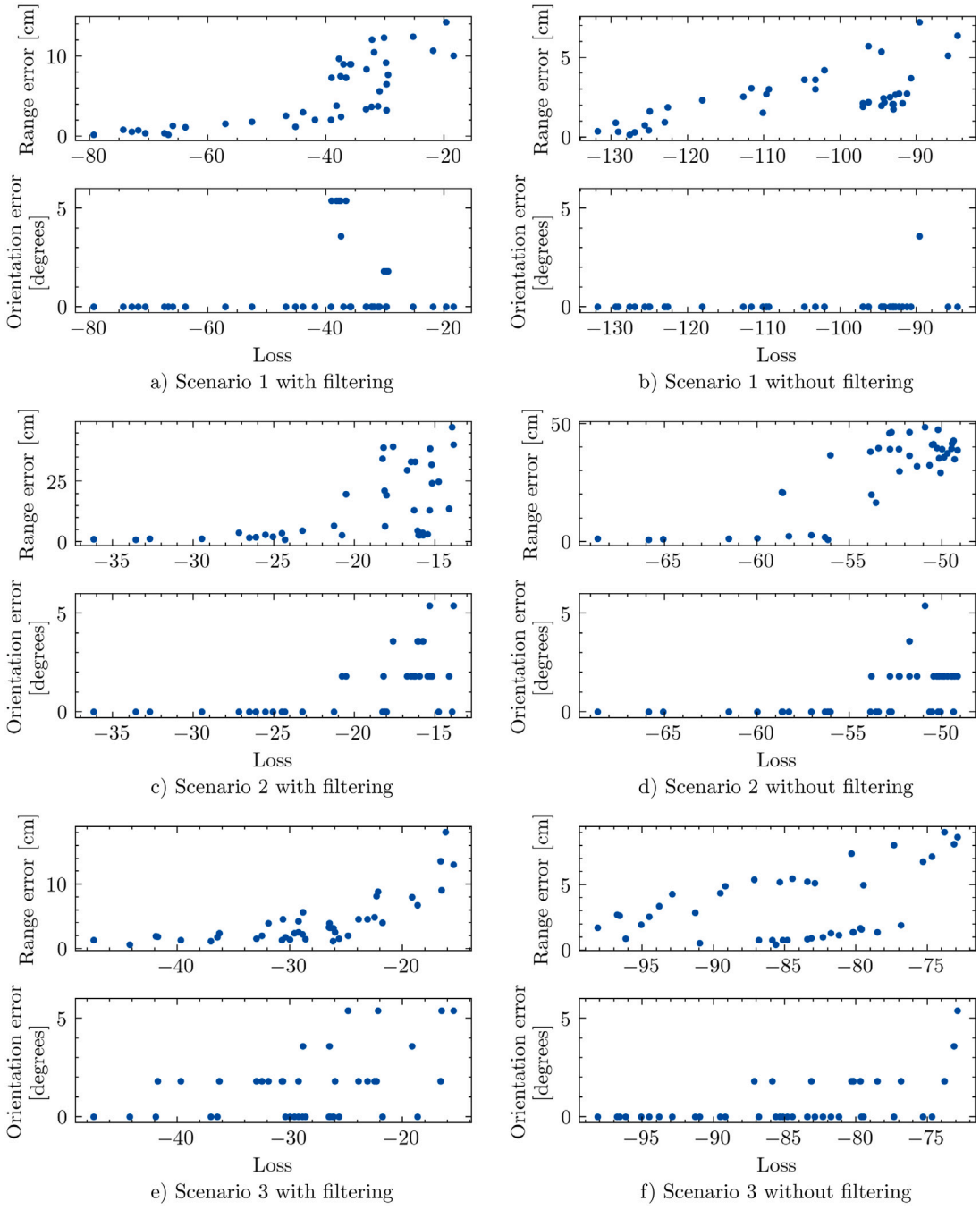

Fig. 8. 2D plots showing the correlation and loss values achieved using each of the propagation models from the predefined model set, and for the three scenarios. On the left, the loss value and geometry estimates are determined from the high-pass filtered beamforming maps. On the right, they are determined from the standard maps without filtering.

achieved during the optimization process. The upper and lower bounds of the filled areas represent the minimum and maximum values over the 10 runs, at each iteration step, while the solid blue lines account for the mean values. For comparison, the loss values and reconstruction errors achieved when using the predetermined propagation models for the two scenarios are also displayed.

In both scenarios, the achieved minimum loss decreases monotonically until it reaches a plateau. The final loss value is always lower than the loss value achieved with the predetermined model in Scenario 1 and significantly lower in Scenario 2. In terms of reconstruction error, the final average range error is comparable to that achieved with the predetermined model, which is 3 mm for Scenario 1. It is slightly above the estimation error value obtained with the predetermined model (0.5 cm) for Scenario 2. Besides, the orientation errors rapidly decrease to zero for all the runs, achieving the same precision as the predetermined models in the two scenarios.

Altogether, these experiments demonstrate that a propagation model can be efficiently recovered to estimate a plate geometry through optimal beamforming by relying directly on data, regardless of the plate size and material, and as long as the measurements have been acquired on a sufficient portion of the surface.

5.4. Model learning and plate mapping in non-nominal acquisition conditions

We perform the same experiments using the data from Scenario 3 which have been acquired in slightly disturbed conditions due to the

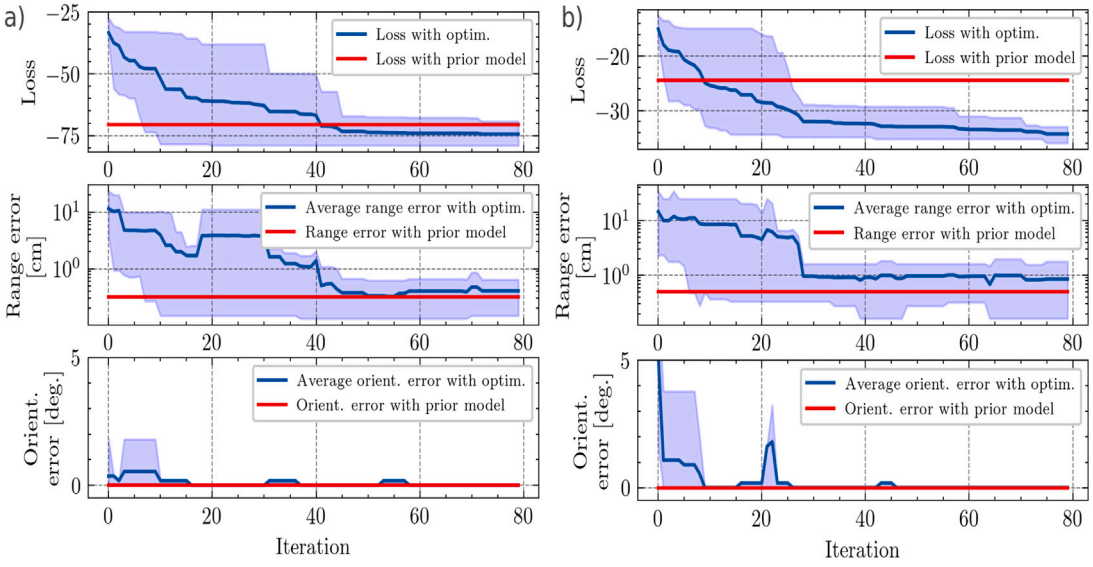

Fig. 9. Evolution of the loss value and reconstruction errors for 10 repetitions of the optimization process with simulated annealing, and using the data from Scenario 1 (a) and Scenario 2 (b). The solid lines represent the mean values. The upper and lower bounds of the filled areas represent the minimum and maximum values respectively during each iteration. For comparison, the values achieved with the predetermined propagation model for each scenario are displayed as horizontal lines. The scale along the y-axis is logarithmic for the range error plots only.

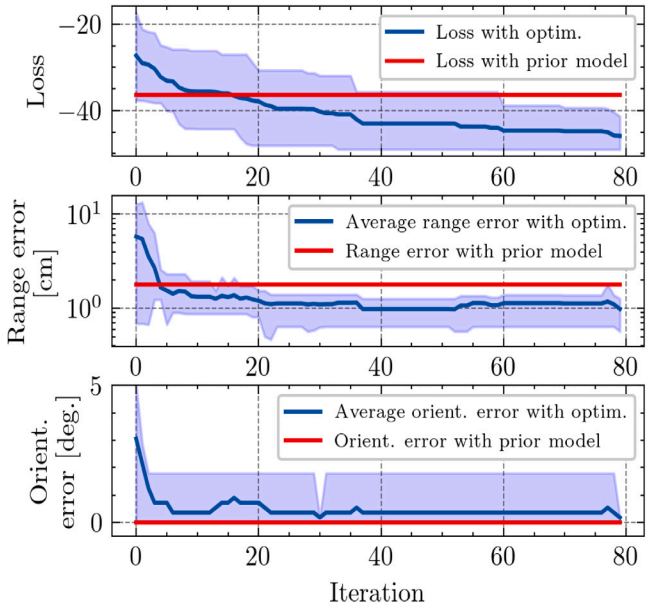

Fig. 10. Evolution of the loss value and reconstruction errors for 10 repetitions of the optimization process and using the data from Scenario 3. The blue lines represent the mean values. The upper and lower bounds of the colored areas represent the minimum and maximum values respectively during each iteration. For comparison, the values achieved with the predetermined propagation model are displayed as horizontal red lines. The scale along the y-axis is logarithmic for the range error plot only.

layer of water that is placed at the interface between the transducers and the plate surface. The evolution of the loss and the reconstruction errors for 10 repetitions of the optimization process with random initial parameter values is shown in Fig. 10. It can be observed that the loss rapidly decreases to a value lower than that achieved with the predetermined model. Regarding the reconstruction error, the average range error, after convergence, reaches 1 cm while the error is 2 cm when using the predetermined model for the geometry reconstruction. Furthermore, the orientation error rapidly decreases to a value lower than one degree.

Altogether, our approach, which automatically calibrates the propagation model based on data, yields better geometry estimates in this disturbed scenario compared to mapping with the predetermined propagation model, as illustrated by Fig. 10. These results are promising as the propagation in the thin layer of water has not been modeled explicitly. This further shows the potential of our approach which adapts the propagation model to achieve accurate plate reconstruction in varying conditions, as it is expected to happen for a robotic inspection task on large structures in challenging outdoor environments. Also, with our approach, there is potentially no need to take into account slight sources of disturbance explicitly in the propagation models.

5.5. Non uniqueness of the optimal model parameters

Although we have shown that a propagation model can be recovered based on data to achieve precise localization by adapting the model parameters, our method cannot recover the real values of the physical model parameters. Indeed, different model parameters can yield equivalent loss values as depicted by Fig. 11, where we represent the variation of the loss w.r.t. the two velocity parameters for a fixed thickness (d = 6 mm), and using the data acquired on the two metal plates considered in this study (Scenario 1 and 2). The more specific explanation is that different model parameters may lead to similar dispersion values in the considered frequency bandwidth, after resolving the Rayleigh–Lamb equations. Yet, the fact that the actual model parameters cannot be recovered with our method is not a significant issue, as our primary objective is to achieve accurate mapping of the plate structure with a calibrated model g, so that the wavepackets inside the measurements can be appropriately accounted for.

5.6. Evaluation of our approach with sparse measurements

During a real robotic inspection task, the acoustic measurements may not have been acquired over a dense grid, and over a sufficient portion of the surface during the calibration operation to fully recover the plate geometry. To evaluate the performance of our approach in more realistic scenarios, we assess how the quantity of measurements available during the optimization process affects the propagation model selection when the data are acquired along more realistic trajectories. To avoid running the optimizer every time, we consider the previous

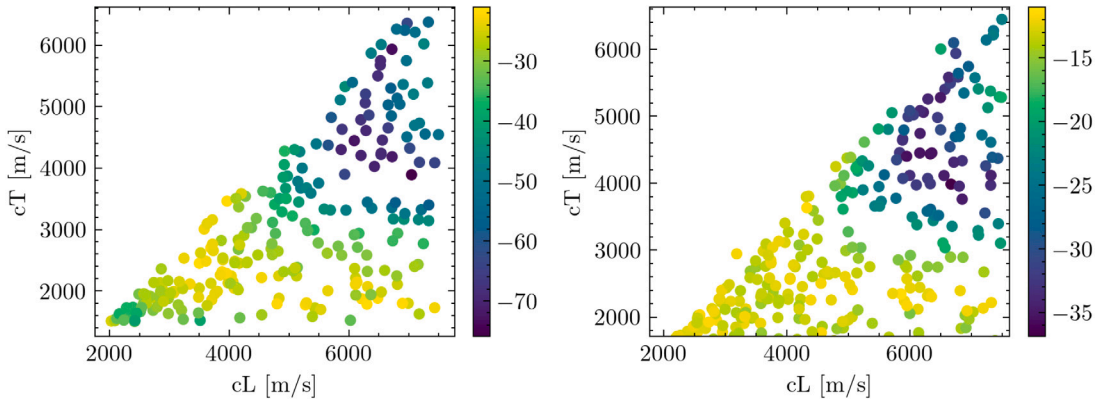

Fig. 11. Loss value computed on the high-pass filtered beamforming maps with respect to the longitudinal and transverse velocities. The data from Scenario 1 are used for the plot on the left, while the data from Scenario 2 are used for the plot on the right.

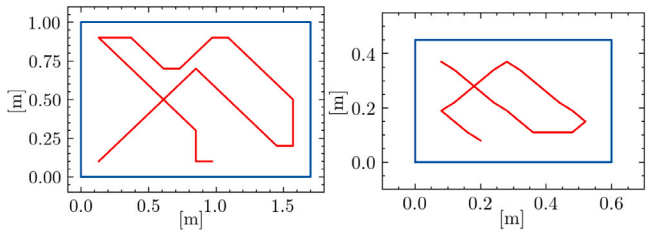

Fig. 12. Simulated robot paths used for the experiments on the steel plate (left) and the aluminum plate (right). The path lengths (*i.e* the number of acquisition positions) are respectively 36 and 26.

family of 40 propagation models. We evaluate, for each propagation model, the reconstruction errors obtained with and without filtering the beamforming maps, and select the error relative to the propagation model, for every set of measurements, that yields the lowest loss value. We also assess the estimation errors when the predetermined propagation model is used along with high-pass filtered beamforming maps, for comparison. We design two different trajectories (one for each plate) that are provided in Fig. 12. The results, which are shown in Fig. 13, were obtained using the data acquired on the large steel plate (Scenario 2) and using the data acquired in the disturbed conditions (Scenario 3).

When only a few measurements are available, the average range errors are relatively high in all the cases, because the sensors need to pass by a border closely enough to detect it. The most accurate results are achieved when all the measurements are taken into account. In the middle, we can see, in Fig. 13-(a), that the minimum range error is reached faster when the beamforming maps have been filtered, and this minimum error is lower than the error achieved with the predetermined model. Furthermore, both in Fig. 13-(a) and (b), the reconstruction errors are seemingly lower when relying on model calibration for the reconstruction. Overall, the results show that our approach is effective for mapping, and yields similar – if not better – performance than that obtained with a predetermined propagation model, even when the measurements have been sparsely acquired by the mobile unit.

6. Discussions

The method presented here restricts the propagation models to be approximate solutions of the Helmholtz equation with dispersion relations derived from the Rayleigh–Lamb equation. This approach is not sufficient for recovering the actual model parameters, and addressing this in future work would be desirable for a complete NDT method (the knowledge of plate thickness variation would be of particular importance). Yet, the recovered propagation model $\hat{g}$ is sufficient to achieve accurate mapping results through beamforming. Whether this approach remains appropriate in more realistic conditions (*i.e* on a real ship hull for example) is still subject to investigation. It is expected that this parametrization would be sufficient as long as the first-order wave-packets are sufficiently energetic within the measurements, and that the major hypotheses on the propagation model (linear propagation, homogeneous and isotropic material) approximately hold. Due to the large size of the plates on a real structure and the low reflectivity of weld joints, the signal-to-noise ratio (SNR) is expected to be low. Hence, a study evaluating the performance of our approach for various SNR conditions is needed to assess how likely it would work in practice. Also, it is to be noted that, in the present study, the sensor positions were measured accurately, whereas in practice, only estimated positions will be available.

The case of multi-modal propagation is not considered here, whereas it is likely if the frequency is not sufficiently adequate to the material in a -presumably- unknown state, or if mode conversion occurs. Having at least A0 and S0 modes propagating simultaneously is the most frequent scenario. It is believed that the algorithm could be extended by considering several hypotheses (bi-modal, A0-only, S0-only propagation, mode conversion for different paths, see [4]) to determine which one is most likely based on data. However, integrating more complex interactions such as diffraction due, for example, to complex structural features such as stiffeners, holes... would be more challenging. We expect isotropic propagation to be prevalent, as these complex wave interactions may be scarce and have a sufficiently small incidence on the signals to not affect the mapping results.

Besides, our method, as presented here, is restricted to rectangular geometries, as it facilitates edge retrieval from the beamforming map. This constraint is not a limitation for mapping storage tanks or ship hulls, as they are almost entirely made of rectangular panels. Yet, our approach could be extended in future work to make it applicable to structures with more general geometries. One may also want to adapt our approach to more conventional applications in SHM where, for example, the propagation model could be automatically calibrated by maximizing the energy focused at the estimated defect location on the imaging results, or by relying on the reflections on the sample boundaries.

7. Conclusion

In this paper, we introduce a method to accurately recover the geometry of a metal plate by relying on ultrasonic measurements acquired by a mobile unit, in pulse-echo, and without using a predetermined propagation model. Our approach is based on focalization in the model parameter space and beamforming for localization of the plate boundaries. We restrict the propagation model to be an approximate solution of the Helmholtz equation and parametrize it with only three physical

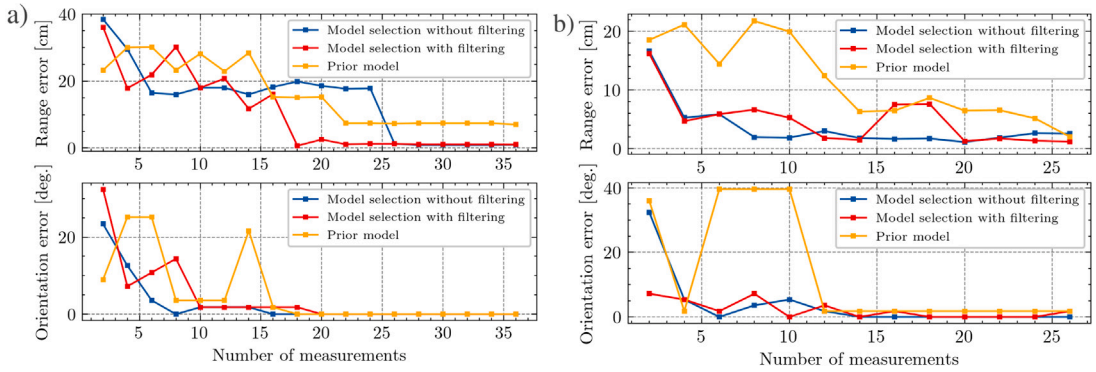

Fig. 13. Reconstruction errors w.r.t. the number of measurements considered in the loss, and using the data from Scenario 2 (a) or from Scenario 3 (b). The measurements are integrated one after the other in the loss, following the simulated paths. The error is only evaluated for the model yielding the lower loss value for the two cases (model selection with and without filtering the beamforming maps). For comparison, the errors achieved with the predetermined models are also displayed.

values. We introduce a loss function assessed on high-pass filtered beamforming maps to quantify the focusing ability of a candidate beamformer (*i.e.*, candidate model parameters). Eventually, we find optimal model parameters with a simulated annealing optimization process.

We demonstrate the performance of our method on three sets of experimental acoustic data acquired on a dense grid on two metal plates of different sizes and different materials. The results illustrate the relevance of filtering the beamforming maps to reduce the impact of interference and high-order reflections. We also show that a propagation model enabling accurate boundary localization can be recovered with simulated annealing. For the two undisturbed scenarios, the precision of the localization is found to be similar to that achieved with the model built from prior knowledge on the plate material, but it is found to be superior in non-nominal acquisition conditions. This highlights the very potential of our method for Lamb wave-based localization and mapping on a large metal structure, where the wave propagation conditions may not be known a priori. The benefit of this approach is real for practical industrial inspection tasks, where the propagation models could be automatically calibrated. Eventually, we assess the performance of our approach using reduced numbers of measurements acquired on the two plates, and following more realistic robot trajectories. The results illustrate that the proposed approach can recover the plate geometry accurately even with sparse measurements, and outperforms the mapping based on the predetermined propagation model.

In future work, the method shall be integrated within a simultaneous localization and mapping framework, as the sensor positions need to be estimated as well. Also, the hypothesis of rectangular plate geometries shall be relaxed, and more complex wave phenomena such as anisotropic and/or multi-modal propagation, diffraction, or mode conversion are to be integrated in the model. The recovery of the real physical parameters, such as plate thickness, and the mapping of defects shall be investigated to make possible a complete robotic NDT task. Finally, the method shall be tested in more realistic conditions, with a real robotic platform such as a magnetic crawler to acquire the signals.

Declaration of competing interest

The authors declare that they have no known competing financial interests or personal relationships that could have appeared to influence the work reported in this paper.

References

[1] Bugwright2, autonomous robotic inspection and maintenance on ship hulls and storage tanks, description of the innovative action (information and communication technologies), 2020.

[2] Roboplanet, robots for human and industrial and safety http://www.roboplanet.fr/en/.

[3] Z. Su, L. Ye, Identification of Damage using Lamb Waves, in: Lecture Notes in Applied and Computational Mechanics. LNACM, vol. 56, 2011.

[4] M. Zhao, W. Zhou, Y. Huang, H. Li, Sparse Bayesian learning approach for propagation distance recognition and damage localization in plate-like structures using guided waves, Struct. Health Monit. 20 (1) (2021) 3–24, http://dx.doi.org/10.1177/1475921720902277.

[5] Z. Su, L. Ye, Y. Lu, Guided lamb waves for identification of damage in composite structures: A review, J. Sound Vib. 295 (3) (2006) 753–780.

[6] J.S. Hall, P. McKeon, L. Satyanarayan, J.E. Michaels, N.F. Declercq, Y.H. Berthelot, Minimum variance guided wave imaging in a quasi-isotropic composite plate, Smart Mater. Struct. 20 (2) (2011) http://dx.doi.org/10.1088/0964-1726/20/2/025013.

[7] N. O'Donoughue, J.B. Harley, C. Liu, J.M.F. Moura, I. Oppenheim, Maximum likelihood defect localization in a pipe using guided acoustic waves, in: Conference Record - Asilomar Conference on Signals, Systems and Computers, 2012, pp. 1863–1867, http://dx.doi.org/10.1109/ACSSC.2012.6489360.

[8] S.R. Anton, D.J. Inman, G. Park, Reference-free damage detection using instantaneous baseline measurements, AIAA J. 47 (8) (2009) 1952–1964, http://dx.doi.org/10.2514/1.43252.

[9] J. Qiu, F. Li, S. Abbas, Y. Zhu, A baseline-free damage detection approach based on distance compensation of guided waves, J. Low Freq. Noise Vib. Act. Control 38 (3–4) (2019) 1132–1148, http://dx.doi.org/10.1177/1461348418813699.

[10] S.J. Lee, N. Gandhi, J.S. Hall, J.E. Michaels, B. Xu, T.E. Michaels, M. Ruzzene, Baseline-free guided wave imaging via adaptive source removal, Struct. Health Monit. 11 (4) (2012) 472–481, http://dx.doi.org/10.1177/1475921711435536.

[11] J.H. Han, Y.J. Kim, Time-frequency beamforming for nondestructive evaluations of plate using ultrasonic Lamb wave, Mech. Syst. Signal Process. 54 (2015) 336–356, http://dx.doi.org/10.1016/j.ymssp.2014.09.008.

[12] G. Dobie, S.G. Pierce, G. Hayward, The feasibility of synthetic aperture guided wave imaging to a mobile sensor platform, Ndt & E Int. 58 (2013) 10–17.

[13] M. Tabatabaeipour, et al., A feasibility study on guided wave-based robotic mapping, in: 2019 IEEE International Ultrasonics Symposium (IUS), IEEE, 2019, pp. 1567–1570.

[14] A. Miranda, C. Gonzales, A. Balyan, C. Schaal, Mobile robotic platform for inspecting aircraft surfaces using lamb waves, Struct. Health Monit. 2019 (2019).

[15] J.M. Galán, R. Abascal, Numerical simulation of Lamb wave scattering in semi-infinite plates, Internat. J. Numer. Methods Engrg. 53 (5) (2002) 1145–1173, http://dx.doi.org/10.1002/nme.331.

[16] O. Ouabi, P. Pomarede, M. Geist, N.F. Declercq, C. Pradalier, Monte-Carlo localization on metal plates based on ultrasonic guided waves, in: The 17th International Symposium on Experimental Robotics, 2020, pp. 345–353.

[17] S. Thrun, B. Wolfram, D. Fox, Probabilistic Robotics - 2nd Edition, in: Intelligent Robotics and Autonomous Agents series, MIT Press, 2005.

[18] C. Xu, Z. Yang, M. Deng, Weighted structured sparse reconstruction-based lamb wave imaging exploiting multipath edge reflections in an isotropic plate, Sensors (Switzerland) 20 (12) (2020) 1–17, http://dx.doi.org/10.3390/s20123502.

[19] A. Ebrahimkhanlou, B. Dubuc, S. Salamone, Damage localization in metallic plate structures using edge-reflected lamb waves, Smart Mater. Struct. 25 (8) (2016) http://dx.doi.org/10.1088/0964-1726/25/8/085035.

[20] L. Zeng, L. Huang, Z. Luo, J. Lin, Damage imaging that exploits multipath scattered lamb waves, Struct. Health Monit. 19 (6) (2020) 1629–1644, http://dx.doi.org/10.1177/1475921719892828.

[21] J.S. Hall, J.E. Michaels, Multipath ultrasonic guided wave imaging in complex structures, Struct. Health Monit. 14 (4) (2015) 345–358, http://dx.doi.org/10.1177/1475921715578316.

[22] C. Schaal, M. Brown, K. Schulz, Experimental investigation of lamb wave-based edge detection methods, 2019, 1097223, http://dx.doi.org/10.1117/12.2515452, 71.
[23] E. Hong, C. Schaal, Reverse engineering stiffened plates using guided wave-based nondestructive testing methods, 2018, p. 13, http://dx.doi.org/10.1117/12.2296745.
[24] K. Grabowski, M. Gawronski, I. Baran, W. Spychalski, W.J. Staszewski, T. Uhl, T. Kundu, P. Packo, Time-distance domain transformation for acoustic emission source localization in thin metallic plates, Ultrasonics 68 (2016) 142–149, http://dx.doi.org/10.1016/j.ultras.2016.02.015.
[25] N. Sen, T. Kundu, Acoustic source localization in a highly anisotropic plate with unknown orientation of its axes of symmetry and material properties with numerical verification, Ultrasonics 100 (2019) (2020) 105977, http://dx.doi.org/10.1016/j.ultras.2019.105977.
[26] A. Miranda, J. Vander Hook, C. Schaal, Lamb wave-based mapping of plate structures via frontier exploration, Ultrasonics 110 (2020) (2021) 106282, http://dx.doi.org/10.1016/j.ultras.2020.106282.
[27] M. Montemerlo, S. Thrun, D. Koller, B. Wegbreit, FastSLAM: A factored solution to the simultaneous localization and mapping problem Michael, in: Proceedings of the National Conference on Artificial Intelligence, 2002.
[28] C. Pradalier, O.L. Ouabi, P. Pomarede, J. Steckel, On-plate localization and mapping for an inspection robot using ultrasonic guided waves: A proof of concept, in: IEEE International Conference on Intelligent Robots and Systems, 2020, pp. 5045–5050, http://dx.doi.org/10.1109/IROS45743.2020.9340936.
[29] B.D. Van Veen, K.M. Buckley, Beamforming: A versatile approach to spatial filtering, IEEE ASSP Mag. 5 (2) (1988) 4–24, http://dx.doi.org/10.1109/53.665.
[30] O.L. Ouabi, P. Pomarede, M. Geist, N.F. Declercq, C. Pradalier, A fastSLAM approach integrating beamforming maps for ultrasound-based robotic inspection of metal structures, IEEE Robot. Autom. Lett. 6 (2) (2021) http://dx.doi.org/10.1109/LRA.2021.3062600.
[31] S. Chaabene, F. Bouchoucha, M.N. Ichchou, M. Haddar, Wave mode diffusion and propagation in structural wave guide under varying temperature, in: Applied Acoustics, Vol. 108, 2015, pp. 84–91.
[32] P. Zabbal, G. Ribay, B. Chapuis, J. Jumel, Multichannel multiple signal classification for dispersion curves extraction of ultrasonic guided waves, J. Acoust. Soc. Am. 143 (2) (2018) EL87–EL92.
[33] C.Y. Chang, F.G. Yuan, Extraction of guided wave dispersion curve in isotropic and anisotropic materials by matrix pencil method, Ultrasonics 89 (2018) 143–154.
[34] S.Y. Chong, M.D. Todd, Dispersion curve estimation via a spatial covariance method with ultrasonic wavefield imaging, Ultrasonics 89 (2018) 46–63.
[35] Q. Chen, K. Xu, D. Ta, High-resolution Lamb waves dispersion curves estimation and elastic property inversion, Ultrasonics 115 (2021) 106427.
[36] T. Kundu, X. Yang, H. Nakatani, N. Takeda, A two-step hybrid technique for accurately localizing acoustic source in anisotropic structures without knowing their material properties, Ultrasonics 56 (2015) 271–278.
[37] S. Yin, Z. Cui, T. Kundu, Acoustic source localization in anisotropic plates with Z shaped sensor clusters, Ultrasonics 84 (2018) 34–37.
[38] A.G. Sazontov, A.I. Malekhanov, Matched field signal processing in underwater sound channels (Review), Acoust. Phys. 61 (2) (2015) 213–230, http://dx.doi.org/10.1134/S1063771015020128.
[39] A.B. Baggeroer, W.A. Kuperman, Matched field processing in ocean acoustics, Acoustic Signal Processing for Ocean Exploration 7 (1993) 9–114, http://dx.doi.org/10.1007/978-94-011-1604-6_8.
[40] M.D. Collins, W.A. Kuperrnan, Focalization: Environmental focusing and source localization, J. Acoust. Soc. Am. 90 (3) (1991) 1410–1422, http://dx.doi.org/10.1121/1.401933.
[41] W.A. Kuperman, M.D. Collins, J.S. Perkins, N.R. Davis, Optimal time-domain beamforming with simulated annealing including application of a priori information, J. Acoust. Soc. Am. 88 (4) (1990) 1802–1810, http://dx.doi.org/10.1121/1.400201.
[42] H. Lamb, On waves in an elastic plate, Proc. R. Soc. A 93 (648) (1917) 114–128.
[43] J.M. Galán, R. Abascal, Numerical simulation of Lamb wave scattering in semi-infinite plates, Internat. J. Numer. Methods Engrg. 53 (5) (2002) 1145–1173, http://dx.doi.org/10.1002/nme.331.
[44] P. Huthwaite, F. Simonetti, High-resolution guided wave tomography, Wave Motion 50 (5) (2013) 979–993, http://dx.doi.org/10.1016/j.wavemoti.2013.04.0044.
[45] N. Quaegebeur, P. Masson, D. Langlois-Demers, P. Micheau, Dispersion-based imaging for structural health monitoring using sparse and compact arrays, Smart Mater. Struct. 20 (2) (2011) http://dx.doi.org/10.1088/0964-1726/20/2/025005.
[46] H. Kuttruff, Room Acoustics, fourth ed., 2000.
[47] S. Kirkpatrick, C.D. Gelatt, M.P. Vecchi, Optimization by simulated annealing, Science 220 (4598) (1983) 671–680, http://dx.doi.org/10.1126/science.220.4598.671.

2020 IEEE/RSJ International Conference on Intelligent Robots and Systems (IROS)
October 25-29, 2020, Las Vegas, NV, USA (Virtual)

On-plate localization and mapping for an inspection robot using ultrasonic guided waves: a proof of concept

Cédric Pradalier[1], Othmane-Latif Ouabi[1], Pascal Pomarede[1] and Jan Steckel[2]

***Abstract*— This paper presents a proof-of-concept for a localization and mapping system for magnetic crawlers performing inspection tasks on structures made of large metal plates. By relying on ultrasonic guided waves reflected from the plate edges, we show that it is possible to recover the plate geometry and robot trajectory to a precision comparable to the signal wavelength. The approach is tested using real acoustic signals acquired on metal plates using lawn-mower paths and random-walks. To the contrary of related works, this paper focuses on the practical details of the localization and mapping algorithm.**

I. Introduction

This paper aims at demonstrating the interest of using ultrasonic guided waves to support inspection robots operating on structures made of metal plates. Such structures include, in particular, ship outer hulls and large storage tanks, as depicted in fig. 1. On such a structure, localization with respect to individual plates can be beneficial to precisely triangulate defects such as corrosion patches [1], [2] or even attempt acoustic tomography as in [3]. In combination with odometry and an external localization system (laser theodolite, Ultra-Wide Band (UWB) beacons...), this would also lead to precise absolute localization of the inspection results.

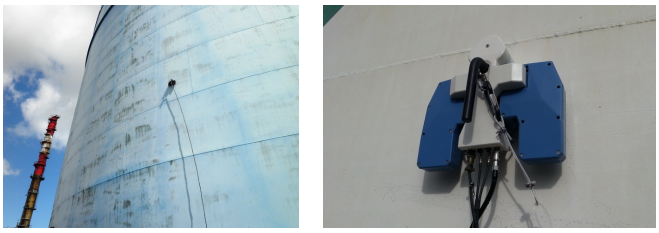

Fig. 1. Typical inspection conditions for magnetic crawlers operating on a structure assembled out of welded steel plates [Source: RoboPlanet[3]].

On metal plates, Ultrasonic Guided Waves (UGWs) can mostly be generated using piezo-electric transducers in contact with the plate. When the relation between the frequency, the plate thickness and the wave velocity is right, these waves propagate radially around the emitter through the plate material, like ripples around a stone thrown into a pool. For metal plates relevant to inspection tasks, frequencies in the range of hundreds of kHz are typically appropriate, with wavelengths of the order of a few centimeters.

In this paper, we are considering short bursts of a few wave cycles emitted from a transducer mounted on a mobile platform. When encountering the plate edges, these waves are reflected normally and these reflections are measured by a transducer co-located with the emitter to be converted into electrical signals. From these signals, it is possible to identify the reflected waves and, from them, recover the distance to the edge. In a practical case, while working on a rectangular plate, the acquired signal may include reflections from multiple edges as well as spurious detections. These sequences of edge detections are essentially range-only measurements to a line. We intend to use these ranges to both reconstruct the geometry of the plate and the localization of the emitter-receiver device over time. In the robotic community, this is a SLAM problem with a non-trivial data-association challenge to identify which edge has been observed at a given time. Although numerous different works have considered the very similar problem of room shape reconstruction from acoustic echoes as a SLAM problem, most of them only consider simulated measurements and do not describe exhaustively their map management strategies.

In summary, the contributions of this paper are:

1) a demonstration of the applicability of a sparsity-based reconstruction of the arrival times of the ultrasonic reflections in the plate using an $\mathcal{L}_1$-regularized least squares approach;
2) a demonstration of the applicability of room reconstruction methodologies to on-plate mapping with a description of the map management strategy, from initialization to landmark addition and outlier removal;
3) a proof-of-concept for the use of FastSLAM[4] in the context of on-plate localization for inspection tasks.

II. Related Works

a) Non-Destructive Evaluation: Ultrasound-based inspection technique is the most common tool for Non-Destructive Evaluation (NDE) on metal plates. In the most common set-up, the transducers are put in transmission or in echo mode. In the first one, two transducers are aligned along the same axis, one transducer is used as an emitter and the second receives the signal after propagation through the sample. In the second mode, one transducer acts both as emitter and receiver and the signal is recorded after reflecting on the sample. This is typically used with high frequencies (i.e. 5MHz) for thickness measurements. Alternatively, this

[1]Cédric Pradalier, Othmane-Latif Ouabi and Pascal Pomarede are with the GeorgiaTech Lorraine and the UMI2958 GT-CNRS in Metz, France. firstname.lastname@georgiatech-metz.fr

[2]Jan Steckel is with the CoSys-Lab, Faculty of Applied Engineering, University of Antwerp, Antwerp, Belgium and with the Flanders Make Strategic Research Center, Lommel, Belgium. firstname.lastname@uantwerpen.be

[3]Partner of the BugWright2 project. This project was supported by the European Commission under grant agreement 871260 - BugWright2.

paper considers the use of Lamb waves, a specific type of UGWs. Those waves propagate along the metal plate, potentially for large distances. In industry, they have been used to detect defects in pipelines, rails, or large structures with success [5], [6], but never deployed on autonomous mobile systems. Another technique is to use signals obtained during the inspection from different positions in order to localize defects using acoustic tomography [1], [2]. This technique is usually used in the Structural Health Monitoring (SHM) field with sensors embedded in the structures [7]. However, for such a technique to work, it is critical to know the location of the emitters and receivers with a good precision, which is a challenge for magnetic crawlers operating on an inspected structure. Most of the mentioned works assume a known localization of the emitter and receiver with respect to the inspected plate, and to the authors' knowledge, there is no work considering that the UGWs themselves could both provide the defect detection capabilities and help to infer the plate geometry and sensor localization.

b) Echo detection: Time delay estimation is often performed using a matched filter approach, which allows high-resolution time-delay estimation under the condition that the signal bandwidth is sufficiently high, and that the auto-correlation function of the used signals is sufficiently narrow [8]. More recently, sparsity-based methods using an $\mathcal{L}_1$-regularized least squares approach have surfaced as super-resolution time-delay estimation, and have been extensively applied to ultrasonic time-delay estimation [9], [10]. This approach promises the detection of highly-overlapping reflections, even under low Signal-to-Noise Ratio (SNR) conditions. In our approach, we will use this sparsity-based approach to solve the time-of-arrival estimation problem.

c) Localization and Mapping: Outside of the field of NDE, the closest problem to on-plate localization and mapping is acoustic room reconstruction. In this sub-field of acoustics and signal processing, there are different works that attempt to reconstruct the shape of a room based on acoustic echoes. [11] addressed the problem of a moving emitter-receiver device to reconstruct a room shape using a geometric solution. [12] showed that SLAM techniques could be used to estimate the shape of a convex room. Both works, however, were only tested in simulation, and did not consider the presence of spurious echoes. [13] expresses the problem as an optimization but is again tested only in simulation and does not address explicitly the ambiguous matching of measurements to room walls.

Besides, in all the works above, the map management strategy is not described exhaustively: in particular, they do not explicit how the geometry of the room is initialized and how map edges are included when first detected or removed when proven to be outliers. From a more practical standpoint, [14] and [15] build a practical room reconstruction system running on a smart-phone. The latter would be used to emit sound pulses that would reflect from the room walls. In [15], a rectangular environment is assumed, with known sizes, and the focus is on localization. In [14], both the localization and the wall estimation are considered with only the first echo but very little information is given on the map management.

In the context of SLAM, data association has always been a critical step, as described in reference works such as [16]. FastSLAM [4] is an alternative formulation of the SLAM problem where the state is estimated by sampling and where each sample contains an estimate of the trajectory and the map collected along this trajectory. FastSLAM also allows handling uncertain data association by including multiple samples for the various association hypotheses. This is particularly important for the problem at hand since the validity of wall hypotheses can sometimes only be estimated several steps after their initialization. To our knowledge, FastSLAM has not been used previously in the context of the acoustic room reconstruction and localization problem.

d) Summary: This work will use UGWs to build on the room reconstruction techniques within a FastSLAM framework. While moving an emitter-receiver pair on a metal plate, this will allow recovering the trajectory of the device and the geometry of the plate. To support fast and robust echo detection, we make use of an $\mathcal{L}_1$-regularized least squares approach to signal-delay estimation using a sparse signal model. This approach allows a very accurate time-delay estimation of multiple overlapping reflections to be performed, even in low SNR conditions. The next section will describe how these components combine together to demonstrate the feasibility of using UGWs for on-plate localization and plate geometry inference.

III. Methodology

A. Notations and assumptions

In this paper we are considering a mobile unit transporting an acoustic emitter-receiver pair on a metal plate. At the k-th scanning position, the emitter sends an acoustic pulse $s_b^k(t)$. Under mild assumptions of the acoustic properties of the ultrasonic probing system, we can model the received transducer signal $s_r^k(t)$ as a linear system through convolution:

$$s_r(t) = x(t) * s_b(t) \tag{1}$$

with $x(t)$ the environments impulse response and $s_r(t)$ which contains information about reflections on the plate edges. The superscript k is omitted when unambiguous.

We assume that the plate is a homogeneous material (steel, aluminium,...) of a constant thickness. We assume the plate to be a convex polygon, but we do not assume it to be rectangular, even though this is to be expected in any industrial case. Because the edges are linear, we will also assume that only the orthogonal reflection of the signal is picked up by the receiver. Any other reflection may lead to secondary echoes after bouncing from several edges but these are neglected in our work.

Out of the reflected signal $s_r^k(t)$, we will denote as $\{r_l(k), l = 1 \dots n(k)\}$ the set of detected ranges to the plate edges, assuming that not all the edges are detected all the time and that spurious detection may be included in the list.

Additionally, because we assume the transducers are carried by a mobile device on the plate, we assume that some

level of odometry is available to estimate the displacement between measurements. Because the inspection crawlers we are considering are moving on vertical structures (boat hulls, storage tanks), they can easily embed an accelerometer from which the crawler heading with respect to gravity can be observed with a good enough precision. Also, by construction, to avoid falling from the inspected structures, these crawlers need to have an extremely good adherence and incur very little slippage. We can hence assume the odometry locally very precise. These two assumptions (known heading and very precise odometry) are an important distinction with respect to the room reconstruction works.

In the next section, we will describe first how these echoes can be robustly extracted from the signal and then how they can be integrated with the proprioceptive measurements into a localization and mapping framework.

B. Echo detection

One of the key enabling technologies for the on-plate SLAM approach is the robust and accurate detection of ultrasonic echoes in the metallic plate. Due to the physics of the sound propagation in the metallic plate, only signals with limited bandwidth can be used for probing the underlying material. This limited bandwidth constraint complicates accurate time-of-arrival estimation for the reflections in the medium, removing classical signal processing techniques such as matched filtering from the set of applicable techniques. We apply a super-resolution technique based on $\mathcal{L}_1$-regularized least-squares and the concept of sparsity to solve this estimation problem. The underlying hypothesis of this approach is that most of the metal plate does not reflect the ultrasonic waves, and that only discontinuities in the medium cause reflections to occur. In that case, the environment response $x(t)$ from eq. 1 has only a limited number of non-zero components and can be considered sparse.

After discretization of the problem, this allows us to cast the following $\mathcal{L}_1$-regularized least squares problem:

$$\min_{\mathbf{x}} |\mathbf{D}\cdot\mathbf{x}-\mathbf{s_r}|_2^2+\lambda\cdot|\mathbf{x}|_1 \tag{2}$$

with $\mathbf{x}$ the discretized vector-representation of the impulse response $x(t)$ of size $[n_t\times 1]$, $\mathbf{s_r}$ the discretized received acoustic signal of size $[n_t\times 1]$, where n_t is the number of time-samples used in the discretization process. The vector norms $|\mathbf{a}|_p$ denote the $\mathcal{L}_p$-norm of vector-object $\mathbf{a}$, with the well-known fact that the $\mathcal{L}_1$-norm promotes sparsity of the least-squares solution. The matrix $\mathbf{D}$ is called a dictionary matrix of size $[n_t\times n_t]$, and contains time-delayed copies of the emitted echo signal $\mathbf{s_b}$:

$$\mathbf{D}=\begin{bmatrix}\mathbf{s_b}(1) & 0 & \dots & 0\\ \mathbf{s_b}(2) & \mathbf{s_b}(1) & \dots & 0\\ \vdots & \vdots & \ddots & \vdots\\ \mathbf{s_b}(n_t) & \mathbf{s_b}(n_{t-1}) & \dots & \mathbf{s_b}(1)\end{bmatrix} \tag{3}$$

This minimization problem is a convex problem which can easily be solved using open-source toolboxes such as the Matlab CVX toolbox [17].

C. From echoes to edge hypotheses

A single echo $r_l(k)$ provides information about the distance to an object. As will be described later, this information is useful to refine the parameters of the edge which reflected this echo. However, this is too ambiguous to initialize a new edge: it could be any tangent to the circle centered on the current pose with radius $r_l(k)$.

In [12], the authors show that 2 echoes taken at different known positions are sufficient to define two line hypotheses: there are only two lines tangent to the two circles defined by these radii and centered on the known poses. A third echo can be used to disambiguate between the two lines if the trajectory is not parallel to the line. Beside requiring three perception steps and the corresponding delay, using three echoes requires considering all the $O(n^3)$ 3-tuples of ranges.

Instead, we use only the last two echoes and deal with the multiple hypotheses in a later step. There are several arguments for this choice: first, the disambiguation with 3 echoes is only useful when the path is not parallel to the edge. However, in most practical deployments where the robot uses its accelerometer to realize vertical or horizontal transects, the path is aligned with the plate edges. Second, even on a non-parallel path, a clear disambiguation requires a large translation between the second and third echo to compensate for the perception noise. Last, when moving on a direction normal to the edge, two measurements are sufficient for a unique solution. Both cases are illustrated in fig. 2.

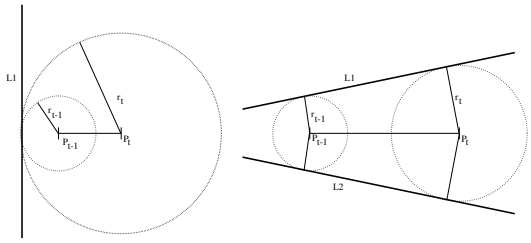

Fig. 2. Line hypotheses generated from two measurements at position P_{t-1} and P_t. Left: the robot moves away from the edge and generate a single hypothesis, right: generic case leading to two hypotheses.

Because of our combinatorial generation of edge hypotheses, a method is required to identify inconsistent edges and remove them. To this end, we take advantage of the hypothesis that only orthogonal reflections are reaching the receiver. Hence, with the assumption of a convex plate, if we consider two edges L_1 and L_2 observed from pose P and P_i the projection of P on L_i, then L_2 cannot intersect the segment $[PP_1]$ and L_1 cannot intersect the segment $[PP_2]$. If one of these conditions is true, then both edges cannot exist simultaneously on a convex plate because observing one edge would require the UGWs to cross the other one, which is not possible. In the following, this test will be denoted as the consistency check between two edge hypotheses.

D. FastSLAM integration

FastSLAM[4] is a solution to the simultaneous localization and mapping problem which is particularly relevant in the

context of uncertain data association. In essence, FastSLAM relies on a particle filter in the localization space and every particle holds a hypothesis of the map that can be inferred from the trajectory of this particle. In order to integrate FastSLAM into our localization and plate geometry inference problem, this section will define the particle state, the chosen map representation, the particle initialization strategy, how the internal maps are updated and the evaluation of a particle based on the measured echoes.

1) FastSLAM state: Because of our assumption of a known orientation, we only consider the sensor coordinates (x, y) on the plate as a system state. Orientation could be added to the state without significant changes.

As a map representation, we use a list of infinite lines represented by an angle and an offset. This is a relatively simple representation comparing to grid maps for example, but still, it offers enough flexibility on the plate geometry. In practice, a line is represented by a pair (θ, b) that defines the line equation:

$$\cos(\theta) \cdot x + \sin(\theta) \cdot y + b = 0 \tag{4}$$

A particle P_i is then described as a trajectory hypothesis associated with an estimated map defined as a set of lines:

$$P_i = [(x_i(s), y_i(s))_{s=1\ldots k}, \{(\theta_{i,j}, b_{i,j}), j = 1 \ldots n_i\}] \tag{5}$$

2) FastSLAM initialization: Most of the earlier papers [12], [13] on room reconstruction do not discuss the initialization of the Bayesian filter, which is an important element for practical implementation. In our case, we rely on the edge hypotheses generated from section III-C. After waiting for the second set of range measurements, we estimate a number of edge hypotheses from which we extract maximally consistent sets. These sets are built using a dynamic programming approach inspired by JCBB/JCDA [16] which will be omitted here for the sake of page limits. As a result, every particle is initialized by sampling around the zero position and randomly selecting a consistent set of edges from the maximally consistent sets. Including all the edge hypotheses in all the particles would be a viable alternative given the outlier removal decision described below. It would however add more ambiguity than necessary in the estimation.

3) Particle evaluation: Given $\{r_l(k), l = 1 \ldots n(k)\}$ the set of echoes measured at the k-th scanning position, we evaluate a particle based on its ability to explain the measurements. For a line $L_{i,j} = (\theta_{i,j}, b_{i,j})$ in particle P_i, the expected measured range is:

$$d_{i,j}(k) = |\cos(\theta_{i,j}) \cdot x_i(k) + \sin(\theta_{i,j}) \cdot y_i(k) + b_{i,j}|$$

From this range, the likelihood of measurement $r_l(k)$ due to a reflection on the line $L_{i,j}$ is expected to follow a Gaussian distribution centered on $d_{i,j}(k)$, with a standard deviation consistent with the echo detection uncertainty. If the highest likelihood over all the lines is lower than a threshold, then the measurement is considered "unexplained" and allocated a low probability P_0. Otherwise, the index of the line leading to the highest likelihood is recorded as $j^\star_{k,l}$. For the purpose of map update, the list of unexplained measurements is also stored to create additional line hypotheses.

For a complete set of echoes, the evaluation of a particle will then be the product of the likelihood of the $n(k)$ likelihoods of the independent measurements:

$$\mathcal{L}(P_i) = \prod_{l=1}^{n(k)} \max\left(P_0, \max_j \left(P\left(r_l(k) \mid P_i, L_{i,j}\right)\right)\right)$$

In this formulation, the product has $n(k)$ terms which makes the evaluation of different particles comparable. Performing the product over the set of lines of each particle would result in a varying number of terms, which is incompatible with importance sampling.

4) Map update: The map update stage has three purposes, first for "explained" measurements, the associated line needs to be updated to account for the new piece of information. Second, the "unexplained" measurements are used to create additional line hypotheses. Third, consistency checks are used to eliminate line hypotheses which are no longer supported by the observations.

a) Line update: Knowing a measurement $r_l(k)$ and its associated line in particle P_i, $L_{i,j^\star_{k,l}}$, one needs to update the corresponding $(\theta_{i,j^\star}, b_{i,j^\star})$. The definition of $d_{i,j}(k)$ suggests the use of an Extended Kalman Filter. Even though such a filter is feasible, the individual measurements can often be explained equivalently by changing $\theta_{i,j^\star}$ or $b_{i,j^\star}$, which prevents a precise convergence of the filter. To sidestep this issue, an alternative is to keep a record of the pairs of sensor poses and ranges associated with this line in a set $\mathbf{E}_{i,j^\star}$, and to minimize the following cost function:

$$C_{i,j^\star}(\theta, b) = \sum_{(s,l)\in\mathbf{E}_{i,j^\star}} \left[\left(x_i(s)\cos(\theta) + y_i(s)\sin(\theta) + b\right)^2 - r_l^2(s)\right]^2 \tag{6}$$

Although much more expensive, this approach converges without bias even when the measurements are taken on a monotonic walk along the edge.

b) New lines: For unexplained measurements, we need to combine them with the measurements from the previous pose to create edge hypotheses (sec. III-C). Every pair made of one previous measurement and a new unexplained measurement is used to generate one or two edge hypotheses. All the previous measurements are used for additional robustness against incorrectly associated measurements at the previous time step. All these hypotheses are added to the line set of the current particles.

c) Map clean-up: In a final stage of the map update, all the lines in a particle line set are checked for pairwise consistency. If two lines are deemed inconsistent and one of them has been observed (i.e. associated with a measurement) significantly more than the other since its creation, then the least observed line is marked for deletion. In our implementation, this criterion is defined as being observed two additional times. In this stage, we also mark for deletion lines that were not re-observed enough since their creation.

For instance, we delete a line that is more than 10 step-old but has been observed less than 3 times. The simple delayed outlier removal described in this paragraph is what makes possible the generation of many edge hypotheses from the set of detected echoes. This is critical since many of these hypotheses cannot be ruled out until the robot moves significantly and changes direction. In comparison, in [12] the authors made the hypotheses of a random walk of the agent, which is a much more informative path, but also much less realistic for a robotic crawler.

IV. Results

A. Experimental setup

At the time of this writing, the experimental setup is not yet integrated on a robotic crawler. Instead, in order to test our framework in a setup as close as possible from reality, we used a pair of emitter-receiver piezo-electric transducer on two different aluminium plates (plate 1: 470x470x5mm and plate 2: 600x450x6mm) and moved them by hand on the vertices of a regular grid with 30 to 40mm spacing. At every position, the response to 10 ultrasonic scans were averaged and recorded with their acquisition position. A scan in this context is the emission of two periods of a 100kHz sine wave and the recording of $400\mu s$ of an analog signal at 1Msample/second.

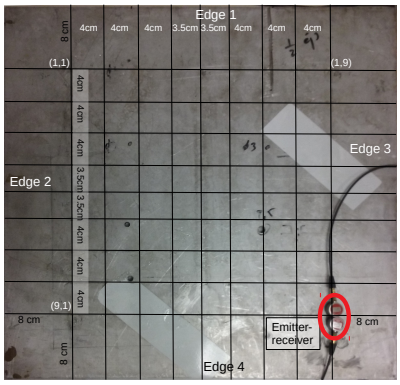

Fig. 3. Experimental setup for metal plate 1. The emitter and receiver transducer can be seen on the bottom right of the figure.

To simulate a sweep of a plate by a robotic crawler, the corresponding sequence of measurements is selected from the database and presented to the SLAM framework, with the theoretic displacement between grid cells used as odometry, even though the hand placement of the transducers is only precise up to 2mm. We believe that, apart from the size of the plates which is smaller than real ones, this setup is a correct representation of a real system in terms of signal quality.

B. Echo detection

Figure 4 illustrates the echo detection process. Panel a) shows the emitted signal, which is a 2-cycle burst at 100kHz. The reflected signal from the plate structure can be seen in panel b). It shows the pickup of the emission at the beginning of the signal, and a reflection due to coupling mismatches. Then, a series of echoes is apparent. Using the $\mathcal{L}_1$-based approach, the impulse response can be reconstructed (see panel b, orange trace). The method reconstructs the major echo components of the impulse response, while ensuring that the solution is sparse. Panel c) shows the reconstruction error. The fact that this residual is not zero can be explained by the fact that the direction-dependent filtering of the transducer is not taken into account during the reconstruction phase with the signal model $\mathbf{D}$. However, as the remaining experiments show, this crude approach to the echo detection process is sufficient for the plate-estimation algorithm.

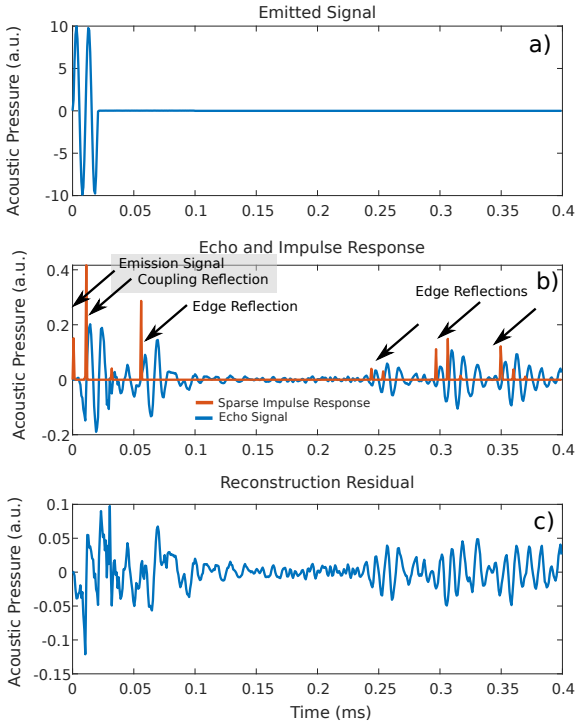

Fig. 4. Illustration of the echo detection process. Panel a) shows the emitted signal. Panel b) shows the echo signal (blue trace) and the reconstructed impulse response (orange trace). Panel c) shows the reconstruction residual.

C. Edge hypotheses

Fig. 5 gives an example of computed edges from the combination of the two first measurements on plate 2. As can be observed, the number of edge hypotheses is relatively large but a few of them are definitely good estimates of the real top and bottom edges. At this position, lateral edges are not observed correctly. The level of uncertainty in the putative edges is what calls for the FastSLAM framework and the delayed decision of the validity of the edges.

D. Mapping performance

Figure 6 shows one anecdotal example of a mapping run on plate 2 by displaying the highest-ranked particle (out of 16 in this case), its line set and its trajectory. The reconstructed path is clearly visible and the stability of the estimate can be observed when performing a second sweep of the path (iterations 225 and 239). The convergence of the estimated lines to the true plate outline can also be observed, with a final error in the order of 2cm on the line offsets b (see eq. 4).

Even though this run has a lower precision than the average case, 2cm is still a very acceptable precision given that the sensors are positioned by hand and that the wave length in this plate is approximately 3cm.

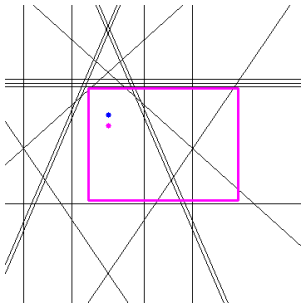

$r(1)$:	0.1151, 0.1297, 0.1436, 0.3406, 0.3557
$r(2)$:	0.1454, 0.1594, 0.1788, 0.1933, 0.3163, 0.3333, 0.4484

Fig. 5. Edge hypotheses generated on plate 2 from detected echoes $r(1)$ (blue dot) and $r(2)$ (purple dot), without consistency check. The purple rectangle is the outline of the true plate.

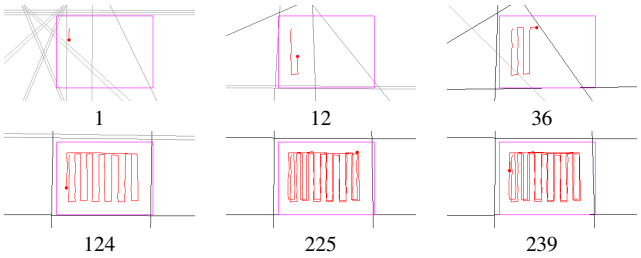

Fig. 6. Evolution of the map representation for the highest-ranked particle at step 1, 12, 36, 124, 225 and 239. The purple frame represents the outline of the true plate. The red dot is the current estimated sensor pose and the red line is the history of its estimated trajectory. The darkness of the line is proportional to the number of times they have been observed. The animation of the run is available on the linked video.

As a final evaluation, we evaluated in Fig. 7 the precision and repeatability of our approach through 100 repetitions in three scenarios. Scenario 1 and 2 consisted of a lawn-mover path through the plate 1 and 2. The length of the sweeping path being 81 steps and 108 steps respectively. In a third scenario, we used plate 1 and simulated localization and plate geometry estimation over a random walk. In the three cases, the real measurements described above were used. However, a single database of measurements was used for every repetition. The table above presents a summary of the resulting precision at different steps in the process. It is clear that the initial estimates after observing only half of the plate are still very uncertain for all the scenarios, but at the end of the simulation, all lines from plate 1 are estimated with a precision consistent with the signal wavelength. The poorer performance on plate 2 is due to the somewhat larger size of the plate and to the presence of artificial defects that are acting as reflectors and creating detection artifacts.

Scenario	Angle error [rad]	Offset error [m]
Scenario 1, step 50	0.017 ± 0.057	0.004 ± 0.032
Scenario 2, step 50	-0.029 ± 0.154	-0.061 ± 0.199
Scenario 3, step 50	-0.008 ± 0.084	-0.031 ± 0.133
Scenario 1, step 239	0.005 ± 0.020	0.002 ± 0.010
Scenario 2, step 239	-0.007 ± 0.091	-0.015 ± 0.126
Scenario 3, step 239	-0.001 ± 0.040	0.002 ± 0.045

Fig. 7. Average errors and standard deviations on the lines parameters estimation after 50 and 239 steps. They are evaluated using 100 repetitions.

V. Conclusions

This paper presented a proof-of-concept for a localization and plate geometry inference framework for a magnetic crawler performing inspection of structures assembled out of metal plates. The results show that there is enough information in the reflected signals to achieve a good localization and mapping precision as long as sufficient coverage of the plate is performed. The next steps will be to embed this framework on a robotic platform as presented in fig. 1, to test on a larger plate, improve the overall system robustness and consider an active sensing strategy to recover the plate geometry faster and even more reliably.

References

[1] T. Druet, B. Chapuis, M. Jules, G. Laffont, and E. Moulin, "Passive SHM system for corrosion detection by guided wave tomography," in *Sensors, Algorithms and Applications for Structural Health Monitoring*. Springer, 2018.

[2] P. Huthwaite and F. Simonetti, "High-resolution guided wave tomography," *Wave Motion*, 2013.

[3] W. Cailly and H. Walaszek, "Three dimensional ultrasonic imaging of mechanical components by inversion," in *7th edition of the International Symposium on AirCraft Materials*, 2018.

[4] M. Montemerlo, S. Thrun, D. Koller, B. Wegbreit, *et al.*, "Fastslam: A factored solution to the simultaneous localization and mapping problem," *Aaai/iaai*, vol. 593598, 2002.

[5] Z. Su, L. Ye, and Y. Lu, "Guided lamb waves for identification of damage in composite structures: A review," *J. Sound Vib*, 2006.

[6] P. Cawley and D. Alleyne, "The use of lamb waves for the long range inspection of large structures," *Ultrasonics*, 1996.

[7] E. Larose, O. I. Lobkis, and R. L. Weaver, "Passive correlation imaging of a buried scatterer," *J. Acoust. Soc. Am*, 2006.

[8] G. Turin, "An introduction to matched filters," *Information Theory, IRE Transactions on*, vol. 6, no. 3, pp. 311–329, 1960.

[9] J. Steckel and H. Peremans, "Sparse decomposition of in-air sonar images for object localization," in *Proceedings of IEEE Sensors*, vol. 2014-Decem, no. December, 2014.

[10] B. Fontaine and H. Peremans, "Determining biosonar images using sparse representations." *The Journal of the Acoustical Society of America*, vol. 125, no. 5, pp. 3052–9, may 2009.

[11] F. Peng, T. Wang, and B. Chen, "Room shape reconstruction with a single mobile acoustic sensor," in *2015 IEEE Global Conference on Signal and Information Processing (GlobalSIP)*. IEEE, 2015.

[12] M. Kreković, I. Dokmanić, and M. Vetterli, "Echoslam: Simultaneous localization and mapping with acoustic echoes," in *2016 IEEE International Conference on Acoustics, Speech and Signal Processing (ICASSP)*. Ieee, 2016, pp. 11–15.

[13] M. Krekovic, I. Dokmanic, and M. Vetterli, "Look, no beacons! optimal all-in-one echoslam," *arXiv preprint arXiv:1608.08753*, 2016.

[14] S. Pradhan, G. Baig, W. Mao, L. Qiu, G. Chen, and B. Yang, "Smartphone-based acoustic indoor space mapping," *Proceedings of the ACM on Interactive, Mobile, Wearable and Ubiquitous Technologies*, vol. 2, no. 2, p. 75, 2018.

[15] X. Song, M. Wang, H. Qiu, and L. Luo, "Indoor pedestrian self-positioning based on image acoustic source impulse using a sensor-rich smartphone," *Sensors*, vol. 18, no. 12, p. 4143, 2018.

[16] J. Neira and J. D. Tardós, "Data association in stochastic mapping using the joint compatibility test," *IEEE Transactions on robotics and automation*, vol. 17, no. 6, pp. 890–897, 2001.

[17] M. Grant, S. Boyd, and Y. Ye, "Cvx: Matlab software for disciplined convex programming," 2008.

Application of ultrasonic guided waves to localization and geometry inference on a metal plate

H. WALASZEK[1], Q.A.VU[1], A. SAIDOUN[1], N. SAMET[2], E. NDIAYE[2], J. THABOUREY[2]

[1]CETIM, 52 avenue Félix Louat, Senlis - France

[2] CETIM Grand Est, 21 rue de Chemnitz, BP 2278, Mulhouse - France

ABSTRACT

Non-destructive inspection of large structures represents one of the major challenges in various industrial sectors (energy, oil & gas, naval, etc.). In recent years, non-destructive testing methods, in particular ultrasonic methods, have been increasingly integrated into autonomous robots in order to carry out faster inspections, and therefore more reliable maintenance without the direct intervention of human operators. The benefit of using a robot during the inspection of large structures consists in the automatization of ultrasonic probe handling and motion, with controlled and reproduceable coupling of ultrasonic probes with the structure to be inspected. Some robotized ultrasonic crawlers are currently available, but are based on local ultrasonic measurements, that leads to important time of operation to scan large hull surfaces. In addition to their potential to detect defects, ultrasonic methods and in particular guided waves are able to propagate for several meters. Guided wave could allow precise localization of the robot and also mapping of structural configurations based on acoustic characteristics of reflected or transmitted waves. In the present work, the boat hull case is considered. A numerical and experimental analysis was carried out in order to study the interactions between different guided wave modes and discontinuities (welds, ribs-stiffeners, and transverse webs). The main goal of this study is the development and integration of an inspection technology in an autonomous robot system applied to the control of large structures (ex: boat hull, tank, etc.).

Keywords: *Guided waves, NDT, BugWright2, autonomous robots*

1 INTRODUCTION

Non-destructive inspection of large structures in various industrial fields increasingly requires the integration of NDT techniques into autonomous robots to overcome financial and security constraints.

Ultrasonic Guided Waves (UGW) have shown a potential for non-destructive testing (NDT) of large structures such as pipelines and storage tanks. In addition to their high sensitivity to internal defects, they have the advantage of fast propagation over long distances, with very little acoustic energy dissipation, allowing inspection of large installations with precise localization of the robot and mapping of structural configurations based on acoustic characteristics [1] [2].

1.1 Application of Ultrasonics measurements for the inspection of large industrial structures

Ultrasonic techniques applied to the control of large structures can be classified into two categories:

1.1.1 Conventional ultrasonic technique

The principle of this method is based on the reflection of all or part of the wave when it encounters an interface of a different nature than the propagation medium. This method is widely implemented on welds or constituent components relating to pressure equipment, storage tanks, transport pipelines, etc.

The control of large areas by this technique necessarily requires a point-by-point inspection with an often-fine mesh, which impacts the control time.

The integration of point-by-point inspection by conventional ultrasound moved by crawler robots is increasingly used, in particular for the control of welds. This inspection mode is suitable for detecting defects but not detection of the boundaries or the welded regions because the bulk waves only propagate in the thickness direction. Therefore, the use of this inspection mode is not suitable for robot location, especially on unknown structures.

1.1.2 Long range ultrasonics technics

For the ultrasonic inspection of large structures, the range of the acoustic waves plays an important role. Due to their propensity to propagate over long distances with a limited loss of energy, this type of elastic wave appears particularly suitable for testing installations consisting of large thin structures such as pipelines.

Guided wave inspection techniques are so-called global inspection methods and quite often remain qualitative. Thus, these techniques enable to provide information about the presence and location of boundaries as welds, and stiffeners. In addition, these techniques enable the detection of a possible defect or damage within the inspected part without necessarily trying to characterize it. Furthermore, as the systems currently available have too large dead zones near the probes and so, suffer of a lack of sensitivity and resolution when more restricted size areas are to be scanned.

Recently, new processing methods have appeared to improve performance in the detection and characterization of defects and to facilitate the interpretation of results. These methods are based on imaging algorithms (SAFT-Synthetic aperture focusing; TFM-Total focusing method; Tomography, Topology, etc.) to improve the resolution and therefore optimize the interpretation of the results.

In the majority of industrial applications using guided wave inspection of large structures, such as pipelines, the sensors remain fixed, in particular for control or Structural Health Monitoring (SHM).

Although the integration of guided wave inspection means in autonomous robots could be beneficial for the field of the inspection of large structures, the number of studies on this subject remains very limited. Nevertheless, we can mention certain works which have shown the feasibility of guided waves for localization as well as the mapping by a robot [3] [4].

1.2 Ultrasonic Guided Waves

Ultrasonic Guided waves (UGW) are generated when the ultrasonic wavelength is close to the thickness of the structure. In an infinite plate consisting of a single medium, two types of guided waves are generally used in Non Destructive Testing, such as Lamb waves and SH waves (Shear Horizontal waves). These guided waves can be interpreted as modes of resonance of the thickness of the plate which propagate along this one, following a direction parallel to the substrate. The plate is therefore deformed along its entire thickness when the guided wave propagates. Lamb waves are polarized in the plane of propagation containing the normal to the surface of the guide and the direction of propagation. The SH waves are polarized perpendicularly to this plane.

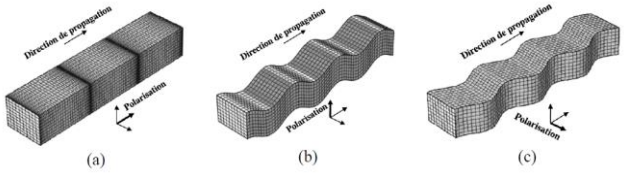

Figure 1 Types of waves propagating in an isotropic solid and polarizations: (a) longitudinal polarization, (b) vertical transverse polarization (c) horizontal transverse polarization [5]

Several sensor technologies are available for the generation and detection of guided ultrasonic waves:

- **Piezoelectric transducers**: this type of sensor is known for its good sensitivity both in transmission and in reception. However, conventional PZT sensors do not allow mode selectivity, which complicates analysis in some applications. A recent study succeeded in developing a special PZT sensor allowing to generate only an omnidirectional SH mode [6] [7].
- **Electro-magnetic acoustic transducers (EMATs):** EMATs make it possible to generate the SH mode directly in the plate without coupling product and to receive them in return after their propagation. It should be noted, however, that EMATs can generate ultrasonic waves only in electrically conductive materials. EMAT probes are composed by a coil connected to a strong current source, combined with a polarizing magnet. As the coil is placed at the surface of the conductive part, the current in the coil produces Lorentz force and magnetostrictive forces in the material, which result in the propagation of an ultrasonic wave [8]. EMAT probes are commonly used to generate volume shear waves in the materials and plate waves [9].

  In some cases, EMAT probes are used to generate at the same time shear and compressional waves in the volume of the parts [10]. EMATS have generally a much lower output efficiency compared to PZT.
- **Magnetostrictive transducers**: To generate guided waves by magnetostriction, a pulsed current is introduced, like in EMAT describes above, into a transmitter coil coupled to a ferromagnetic material. The local modification of the magnetization of the material is accompanied by a deformation of the material in a direction parallel to the applied magnetic field. This deformation, which corresponds to the magnetostrictive effect, generates a shear horizontal wave. The probes used make it possible to generate waves from a few kHz to a few hundred kHz which propagate at the speed of ultrasonic waves in the material.

This work is part of the European project named BugWright2[1] which aims to develop a robotic control methodology on boat hulls. The use of guided wave inspection has two objectives:

- mapping of the structure of the hull and location of the robot
- detection of corrosion defects

In this paper, a numerical and experimental analysis was carried out in order to study the interactions between the different modes of guided waves and the discontinuities encountered on the hull (welds, ribs-stiffeners, and transverse webs), in order to propose the optimal methodology in relation to the objective of the project.

2 EXPERIMENTAL AND NUMERICAL ANALYSIS OF THE GUIDED WAVES INTERACTION WITH METAL PLATE DISCONTINUITIES

2.1 Introduction

Ultrasonic guided waves, which were presented above, have interesting properties for nondestructive testing of large parts

[1] This project has received funding from the European Union's Horizon 2020 research and innovation programme under grant agreement No. 871260. www.Bugwright2.eu

such as welded metal sheets, thanks to their long-distance range propagation, due to a moderate attenuation versus distance. So, a study was led to understand the interaction of these waves with plate discontinuities. These discontinuities consist in welded joints i.e ribs and stiffeners. This section consists of studying the propagation of two different modes (SH_0 and A_0). The objective is to determinate the best candidate for detecting the plate discontinuities.

The study was performed using a representative mock-up of boat hull. Two approaches have been carried out:

- 2-D numerical modelling by finite element method (FEM): in order to analyze the behavior of the waves on the discontinuities, and to check their sensitivity for detecting discontinuities.
- Experimental trials: in order to compare and confirm the numerical results in real conditions.

2.2 *Design of specific mock-up*

To simplify numerical and experimental tests regarding the challenge of boat size and accessibility, a representative mock-up was designed and manufactured. This mock-up is a part of a boat hull at scale one.

The design of the mock-up is shown in the Figure 2 :

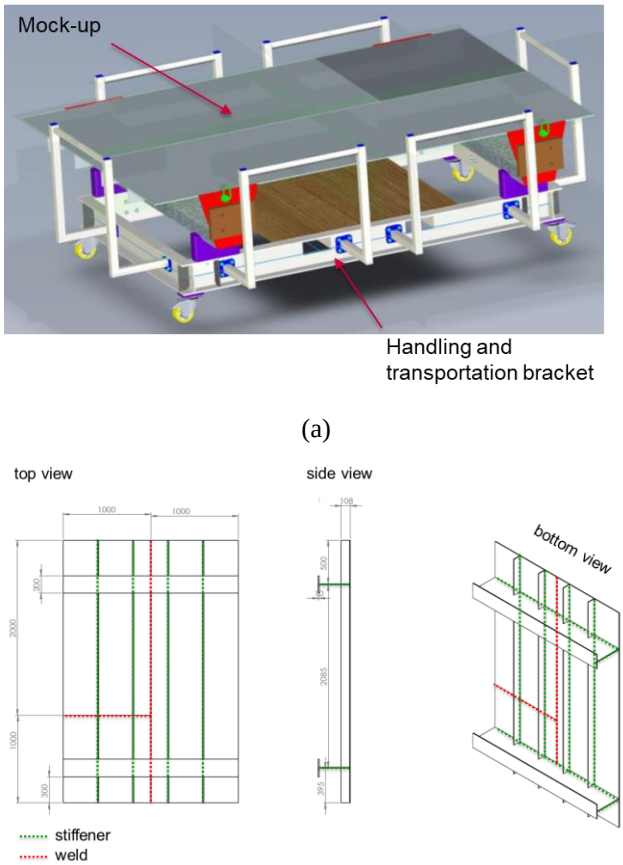

Figure 2: Modelling of a specific mock-up for the use of ultrasonic guided waves to monitor boat hull. (a) The mock-up handled on his transportation bracket and (b) the different views of the mock-up. All units in mm.

The mock-up is of dimensions: 2000 x 3000 x 8.8mm, in steel S235 without treatment. The plates have a thickness of 8mm with a coating layer of 0.8mm thick in average. It contains 2 butt welds: a longitudinal one and a transversal one, 4 longitudinal stiffeners and 2 transversal ones (stringers). All the dimensions of the mock-up's components are highlighted on the Figure 2 (b).

2.3 *Numerical modeling*

The software Comsol Multiphysics® is used to simulate guided waves propagation on the modelled mock-up. The fundamental Shear Horizontal wave SH_0 and the fundamental antisymmetric Lamb wave A_0 are chosen for their non-dispersive characteristics at low frequencies. The choice of these modes will be justified below. The numerical study is consisting of propagating the 2 modes (SH_0 and A_0) in the modelized mock-up in order to observe the interactions between the modes and the different obstacles i.e longitudinal and transversal welds and stiffeners. For all the numerical specimens, 2-D plane strain conditions are considered.

Three 2-D cuts of the mock-up were realized to obtain 3 different geometrical configurations. These numerical specimens are shown in the Figure 3.

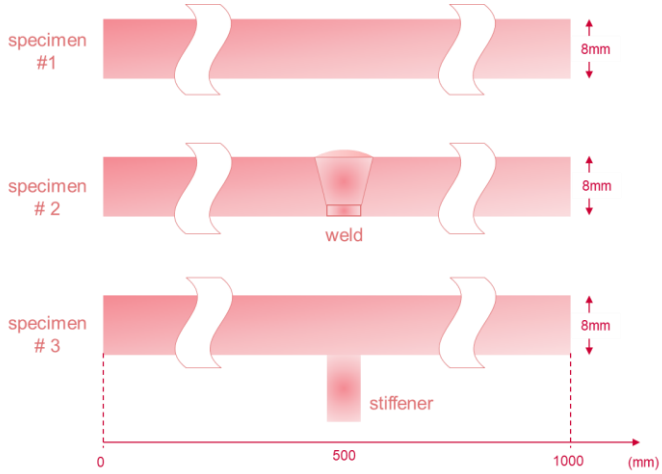

Figure 3: 2-D modeling of the plate representing the realized mock-up. Specimen #1: the plate without obstacle – specimen #2: the plate with weld obstacle #3: the plate with stiffener obstacle.

The material properties used for the simulations are summarized in the **Table 1**.

Table 1: Mechanical properties of the Steel

Parameter	**Value**
Density / ($kg.m^{-3}$)	7850
Young modulus / GPa	210
Poisson ratio μ	0.3

These configurations are chosen to represent the different cases of obstacles that the waves will encounter on the real mock-up during the experiments. It is important to note that the antifouling thickness coating of 0.8mm is not considered for the propagation of guided waves because its influence on the time arrival of modes is negligible.

Specimen #1: is a free plate without any obstacle. This configuration will be use as the reference for modes propagation.

Specimen #2: is a plate with a butt weld zone at the center. The weld is characterized by a single V-preparation joint of length 10mm with a clearance (trimming) and a heel of 2mm. The weld material has the same properties as the plate material except for the Young modulus which has been reduced by 10% (in order to take into account the heat-affected zone e.g HAZ).

Specimen #3: is a plate with a welded stiffener of 100mm length and 10mm width, located at the center. The stiffener material has the same properties as the plate material except for the Young modulus which has been reduced by 10% (in order to take into account the ZAT).

2.3.1 Shear Horizontal (SH) Guided Waves

2.3.1.a Relation of dispersion

SH_n guided waves for a plate of uniform thickness are characterized by their dispersion relation which is an important feature. This dispersion relation can be written as follow:

$$k^2 = \left(\frac{\omega}{c_T}\right)^2 - \left(\frac{n\pi}{d}\right)^2 \quad (1)$$

where k is the wavenumber, ω the angular frequency, c_T the shear wave velocity of the material, n the mode order and t the thickness of the plate. Knowing that the frequency can be written by $f = \omega / 2\pi$, the group velocity c_g can be derived as:

$$cg = \frac{\mathrm{d}\omega}{\mathrm{dk}} = c_T \sqrt{1 - \left(\frac{nc_T}{2fd}\right)^2} \quad (2)$$

Velocity depends both on the ultrasonic frequency and the plate thickness in addition to the material properties themselves. Dispersion curves of a steel plate of thickness d = 8mm, representative of boat hull material, is plotted on the Figure 4 below. The fundamental shear mode SH_0 (n = 0) is nondispersive while the higher modes are dispersive, especially close to their cut-off frequencies (i.e approximatively 200 kHz for SH_1). We just represent the first higher mode SH_1, but the other ones (SH_2, SH_3…SH_n) appear at higher frequencies.

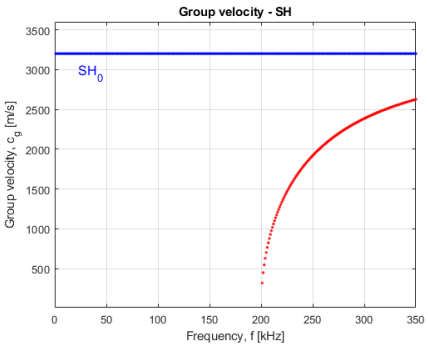

(a)

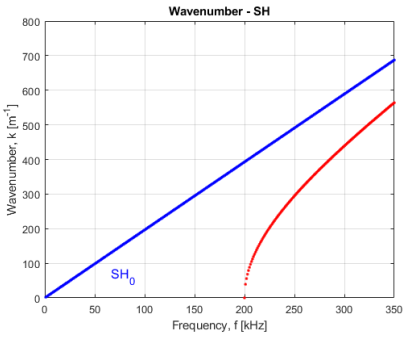

(b)

Figure 4: Dispersion curves of SH waves at the frequency range of [0 – 350kHz]. (a) Groupe velocity versus frequency and (b) wavenumber versus frequency

2.3.1.b Simulation of the SH_0 mode propagation

The displacement field of the SH_0 mode $f_{SH0}(y)$ at each frequency can be analytically calculated. By multiplying this displacement field with a burst of 5 periods centered at the frequency f = 180 kHz we apply this excitation at the left y-boundary (section x = 0mm) of the models. This excitation $s_{SH0}(t)$ is expressed as:

$$s_{SH0}(t) = A.f_{SH0}.\left[1 - cos\left(\frac{2\pi ft}{n}\right)\right] cos(2\pi ft).\left(t \leq \frac{n}{f}\right) \quad (3)$$

Where A denotes the amplitude of the wave, n = 5 the number of the burst's period and t the time.

Simulations are conducted in the transient regime for more than t = 650 µs duration of propagation. This time is enough to ensure a round-trip of the SH_0 mode propagation along the 3 models. For accurate analysis of the wave propagation, a suitable mesh sizing and a temporal sampling are required. For example, the maximum size of mesh element was 0.2mm and the time step 0.1µs. The displacement time dependencies are extracted from the FEM solution on the upper free surface of all the 3 models with a spatial step of 0.1mm. Finally, a time-position amplitude matrix is collected in a form of B-Scan. Results of the propagation of the SH_0 mode along the 3 models are detailed at the section §2.4.1.

2.3.2 Lamb Waves - Antisymmetric mode (A) Relation of dispersion

Lamb waves are also guided plate waves which remain confined inside thin structures. There are two basic kinds of modes: symmetric mode (S_n) and antisymmetric mode (A_n), both are dispersive. In the case of elastic and isotropic material, the Rayleigh-Lamb relation dispersion which permits as to plot dispersion curves, can be derived for Sn and A_n modes as follow:

$$\begin{cases} \frac{tan(pd)}{tan(qd)} = -\frac{(k^2-q^2)^2}{4k^2pq} \\ \frac{tan(pd)}{tan(qd)} = -\frac{4k^2pq}{(k^2-q^2)^2} \end{cases} \quad (4)$$

$$p^2 = \frac{\omega^2}{c_L} - k^2 \; and \; q^2 = \frac{\omega^2}{c_T} - k^2 \quad (5)$$

where d represents the thickness of the plate, k the wavenumber, ω the pulsation, c_L and c_T respectively the longitudinal and the shear velocities.

Dispersion curves of Lamb waves modes of a steel plate of thickness d = 8mm representative of boat hull material is plotted on the Figure 5:

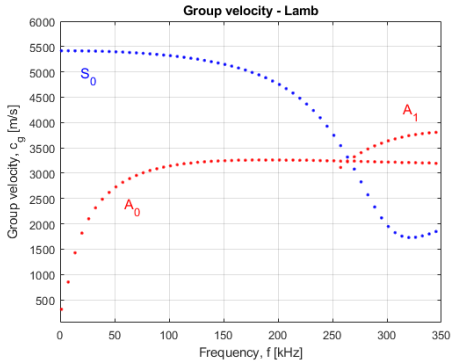

(a)

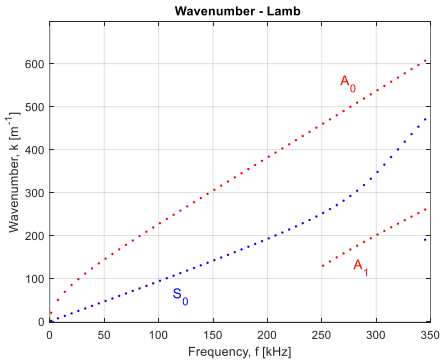

(b)

Figure 5 Dispersion curves of Lamb waves at the frequency range of [0 – 350kHz]. (a) Groupe velocity versus frequency and (b) wavenumber versus frequency

2.3.2.b Simulation of the A_0 mode propagation

The A_0 Lamb wave mode is also simulated by using the theoretical displacement f_{A0} (y) multiplied by a 5-cycle tone burst enclosed in a Hanning window. This excitation s_{A0} (t) is also applied at the left boundary (x = 0mm) at approximately f = 180 kHz and can be expressed as Eq. (3).

Simulations are conducted in the time domain for more than 600µs of propagation. As for the SH_0 wave propagation, a time position amplitude is collected for dt = 0.1µs and dx = 0.1mm to plot B-Scan images of the 3 specimens.

2.4 Numerical results

Results are plotted in term of B-Scan images and in A-Scan signal to visualize reflections and transmissions of guided waves.

2.4.1 Sensitivity of the SH_0 mode

B-Scan imaging:

The displacement amplitudes varying as a function of the time are stored for each position x in term of a matrix s_{SH0} (x, t). The displacement amplitudes are given in color level versus time t and position x. B-Scan images of the 3 specimens are represented in Figure 6.

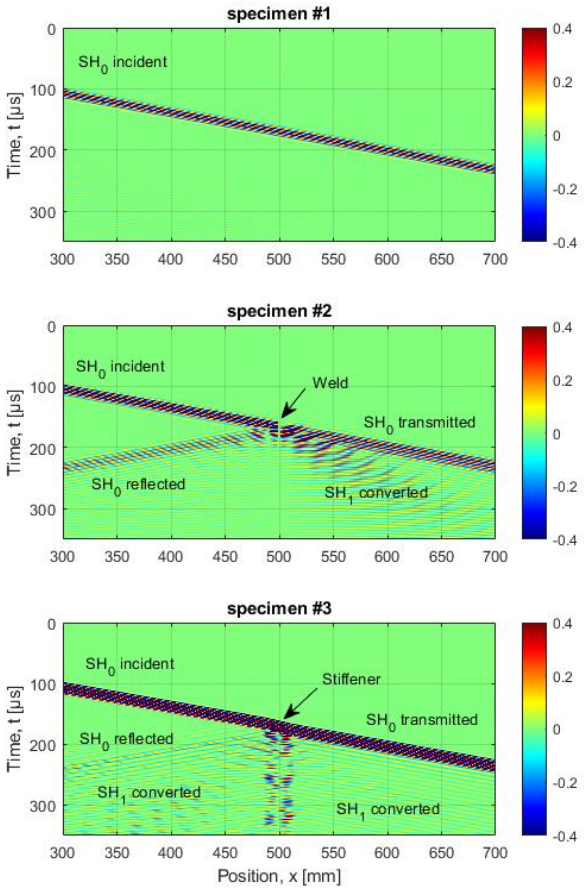

Figure 6: B-Scan images of the SH_0 mode propagation along the 3 specimens

One can see that, if the incident SH_0 mode propagates along specimen #1, any reflection is occurred until the wave packet reaches the back wall of the plate.

However, when the incident SH_0 mode interacts with the weld in specimen #2, a reflection (SH_0 reflected) and a transmission (SH_0 transmitted) appear. In addition, small modes conversions (from SH_0 to SH_1) occur after crossing the weld. The same phenomena are observed when the SH_0 incident mode interacts with the rib in specimen #3.

It can be observed that mode conversions from SH_0 to SH_1 are weak but show the presence of the weld and the stiffener as obstacles to the propagation of the SH_0 mode. Visualization of A-Scan signals simplifies the understanding of reflections and mode conversions.

A-Scan signal:

Analysis in reflection mode

This analysis is made by plotting a cut at the position x = 0mm (left edge of the plate) of the obtained B-Scans. When the SH_0 mode propagates along the specimen #1, any echo appears inside the window between the incident SH_0 emitted and the SH_0 back wall reflection. This SH_0 back wall echo corresponds to the arrival time of the round-trip echo of the incident SH_0 and can be calculated easily from the relation $t = (2 \times d) / 3200 = 625\mu s$ (with d = 1000mm, the plate's length).

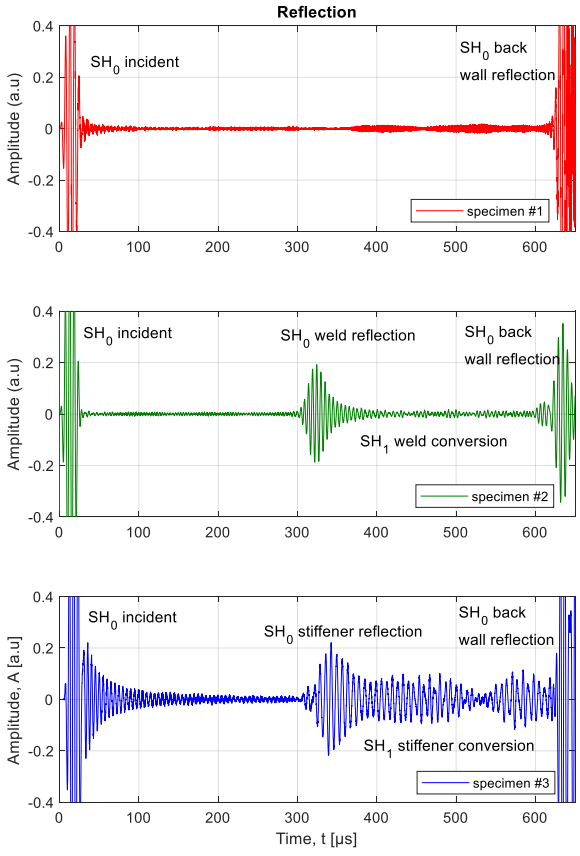

Figure 7: A-Scan signals of the SH_0 mode propagating along the 3 specimens. Visualization of the reflected echoes

With specimen #2 and specimen #3, SH_0 weld reflection and SH_0 stiffener reflection are clearly visible at t = 310µs. They are both followed by the SH_1 mode conversion which is characterized by a dispersion with multiple echoes. This mode conversion from SH_0 to SH_1 is highest with the stiffener than the weld. The analysis in reflection shows that discontinuities can be detected in the three specimens by propagating the SH_0 mode.

Analysis in transmission mode

This analysis in transmission mode is done by plotting a cut of the obtained B-Scans at the position x = 1000mm (right edge of the plate). When the SH_0 mode propagates along the specimen #1, the arrival time of the transmitted wave appears at t = 310µs.

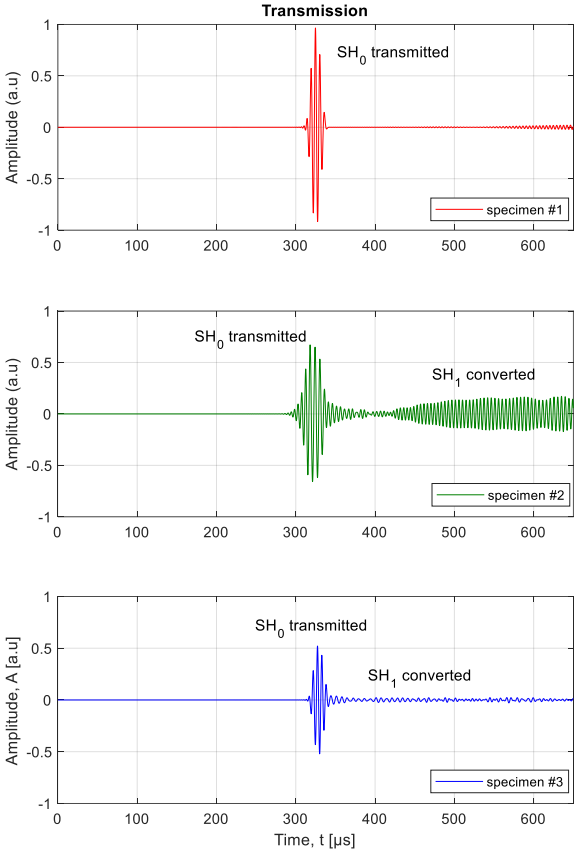

Figure 8: A-Scan signals of the SH_0 mode propagating along the 3 specimens. Visualization of the transmitted echoes

So, when the SH_0 mode propagates along the specimen #2, a very dispersive wave packet appears at approximately t = 420µs in addition to the SH_0 mode at t = 310µs. This large wave packet corresponds to the SH_1 mode conversion due to the presence of the weld. The same observations are done when the SH_0 mode propagates along the specimen #3, the transmitted SH_0 appears at t = 310µs with some others echoes with a less of conversion mode from SH_0 to SH_1 due to the presence of the stiffener.

2.4.2 Sensitivity of the A_0 mode

B-Scan imaging:

When the incident A_0 mode propagates along the specimen #1, any reflection is occurred until the wave packet reaches the back wall of the plate as observed with the SH_0 mode.

However, when the incident A_0 mode interacts with the weld in specimen #2, a reflection (A_0 reflected) and a transmission (A_0 transmitted) appear. In addition, very small modes conversions (from A_0 to S_0) occur. The same phenomena are observed when the A_0 incident mode interacts with the stiffener of the specimen #3.

One can see that mode conversions from A_0 to S_0 are very weak but show the presence of the weld and the stiffener as obstacles of the A_0 mode propagation. Visualization of the A-Scan signals simplifies the understanding of reflections and mode conversions of the propagation

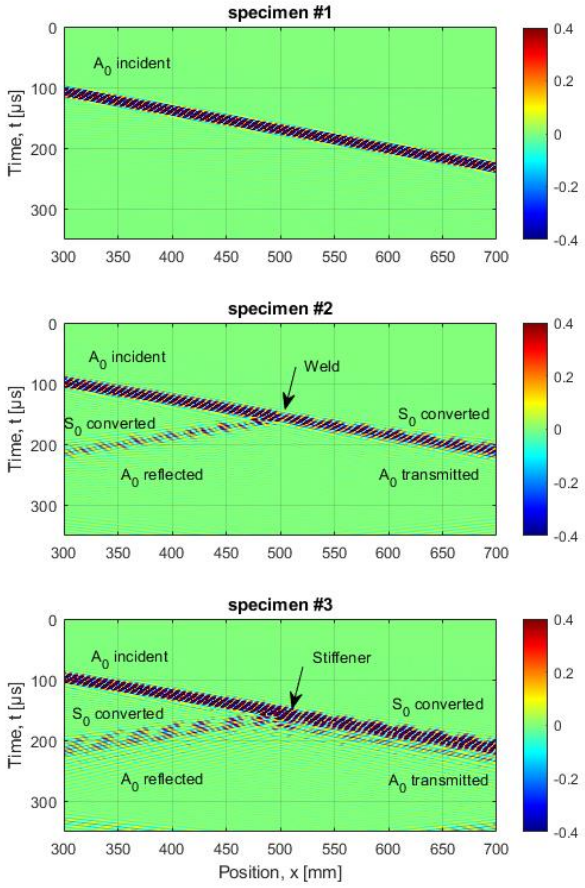

Figure 9 B-Scan images of the A_0 mode propagation along the three models

A-Scan signal:

Analysis in reflection mode

Analysis in reflection is done by plotting a cut of the obtained B-Scans at the position $x = 0$mm. When the A_0 mode propagates along the specimen #1 any echo appears between the incident A_0 echo and the A_0 back wall reflection echo. This A_0 back wall echo corresponds to the arrival time of the round-trip echo of the incident A_0 and the corresponding arrival time is evaluated at $t = 614$µs (with $c_{phA0} = 3260$m/s, the phase velocity of the A_0 mode at $f = 200$kHz).

With specimen #2 and specimen #3, A_0 weld reflection and A_0 stiffener reflection are clearly visible at approximately $t = 300$µs. They are all preceded by S_0 weld conversions which are characterized by a small dispersion. This analysis in reflection shows once again that discontinuities can be detected in the 3 specimens by propagating the A_0 mode at low frequency within his non-dispersive region.

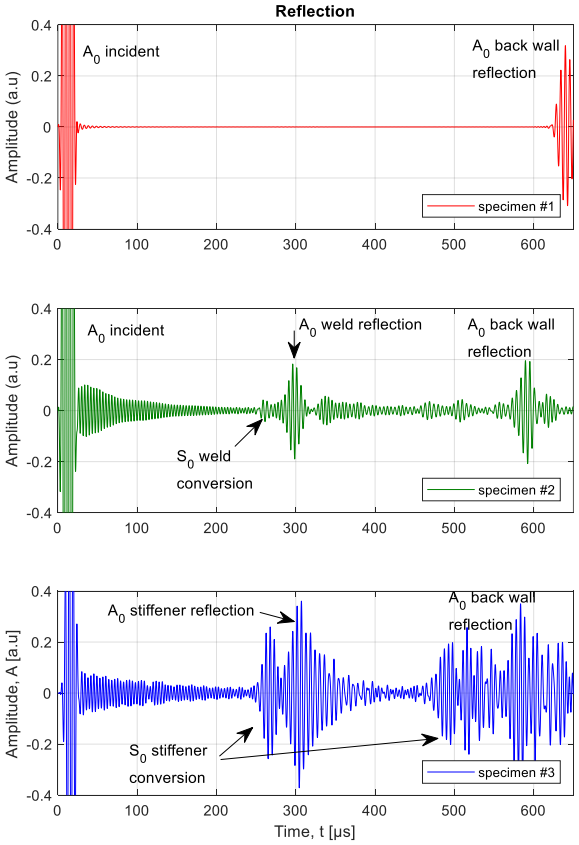

Figure 10: A-Scan signals of the A_0 mode propagating along the three specimens. Visualization of the reflected echoes

Analysis in transmission mode

Analysis in transmission mode is done by plotting signals at the position $x = 1000$mm of the obtained B-Scans. When the A_0 mode propagates along the specimen #1, the arrival time of the transmitted wave appears at $t = 310$µs.

When the A_0 mode propagates along the specimen #2, a dispersive wave packet with small amplitude corresponding to the S_0 weld conversion appears at approximately $t = 270$µs. In addition, the A_0 transmitted mode appears at $t = 295$µs. The same observations are done when the A_0 mode propagates along the specimen #3, the transmitted A_0 appears at $t = 310$µs preceded by another dispersive echo with small amplitude corresponding to the S_0 stiffener conversion.

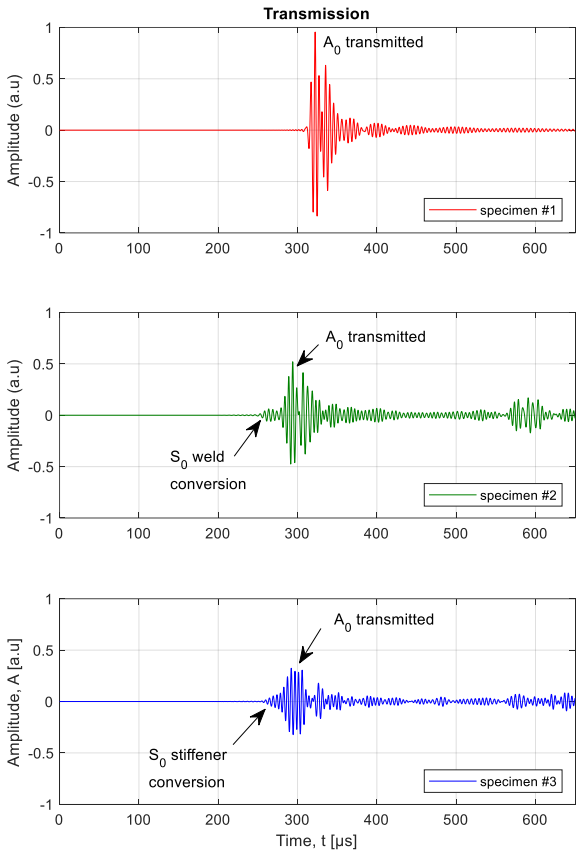

Figure 11: A-Scan signals of the A_0 mode propagating along the 3 specimens. Visualization of the transmitted echoes

2.5 Numerical results – highlights

FEM simulations performed in this numerical part discovered several interesting phenomena concerning the propagation behavior of the fundamental SH_0 and the fundamental A_0 guided waves in the frequency range of 0 to 350 kHz. The principal conclusions can be summarized as follow:

1. SH_0 mode propagates easily with leak attenuation over long distances with small energy loss when it encounters a discontinuity
2. The conversion of SH_0 to SH_1 occurs when it encounters a discontinuity. Indeed, whether with the weld or the stiffener, this phenomenon is observable. This mode conversion is higher when guided waves propagate in specimen #3. This mode conversion is due to the shape of the stiffener (significant thickness variation) and a slight variation in mechanical properties at the interface plate-stiffener. Based on the dispersion curves of the SH modes, it is preferable to carry out simulations or experiments at low frequencies where only the SH_0 mode exists. This can help us to avoid mode conversions from SH_0 to SH_1 and any reflection provided is only the signature of a discontinuity.
3. A_0 mode also propagates easily with leak attenuation over long distances. At the crossing of a discontinuity, a small energy loss is also observed.
4. A_0 mode is also converted to S_0 when it encounters a discontinuity. The same observation made with the SH_0 that mode conversion is higher in the case of the stiffener than in the weld is done.

2.6 Experimental set-up

In both cases of SH_0 and A_0 modes, the choices of transducer and experimental configuration were made in order to generate the interesting modes as being dominant over other guided wave modes.

First, experimental measurements were carried out in a non-defective area to validate the existence of SH_0 and A_0 modes. Then, measurements were achieved in transmission and reflection configurations to investigate the wave interaction with butt weld and stiffener.

For transmission configuration, signal acquisition was conducted by sweeping the receiver from 150 mm to 300 mm, with 5 mm increments. This allows, via FFT-2D analysis, to study all the modes generated in the measurement direction.

In reflection configuration, two transducers are placed side-by-side and the attention has been paid to the reflection echo from butt weld or stiffener.

2.6.1 Shear Horizontal (SH) Guided Waves

EMAT transducers are known as suitable for practical generation of SH waves in ferromagnetic and non-ferromagnetic metals. The Innerspec PowerBox H was used for the signal generation and acquisition. A 274A0107 magnet with T-L-M-0.500x2-1.000 meander coil were used for the emitter, and an identical magnet with the associated model R-L-M-0.500x2-1.000 coil were used for receiving the signal. These EMAT transducers are bidirectional and have a low aperture beam profile.

The excitation signal is a 2 cycles pulse at 230 kHz, which is the central frequency of the EMAT transducers. The tension peak is at 1200 V and the pulse repetition frequency is 25 Hz.

The experimental setups in transmission and reflection configurations are respectively showed in Figure 12. It is important to note that, here the paint coating plays the role of lift-off in EMAT measurement. The coating thickness is variable on the different zones of the mock-up, in the range of 0.3 mm to 0.6 mm.

a/ Transmission configuration in a non-defective area (di: probe displacement increment)

b/ Transmission measurement with the presence of a butt weld

c/ Transmission measurement with the presence of a stiffener

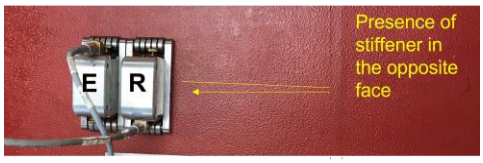

d/ Pseudo pulse-echo configuration for reflection investigation

Figure 12 SH_0 measurement configurations using EMAT transducers.

2.6.2 Lamb Waves - Antisymmetric mode (A_0)

The use of piezoelectric compressional wave transducers to generate and receive the A_0 mode is quite common [11]. In general, the mode S_0 is simultaneously generated. Both wave modes are dispersive. It is important to note that, in such a configuration, the A_0 mode generation is omnidirectional.

Trials are performed on the realized mock-up of 8 mm thick with a paint coating. It is found that the Vallen VS150-M transducers, working in the range of [80 – 450 kHz] with the central frequency of 150 kHz, can generate an energetic A_0 mode. It is noted that this kind of transducer is resonant as it has with a very low damping, due to the fact that the piezo element of the transducer vibrates freely. So, it produces a longer impulsion, consisting in several oscillations than a conventional transducer used with industrial echographs to detect defects in the materials.

The excitation signal is a 5 cycles tone burst enclosed in a Hanning window. The measurements were conducted at different frequencies in the range of 80 kHz – 250 kHz, in which the A_0 mode is considered as being non-dispersive (shown in 2.3.2 numerical study section). Signal acquisition was carried out using NI USB 6356 module with the sampling rate of 1.25 Ms/s.

Experimental measurements were conducted following the same approach as in the case of the SH_0 mode. First, transmission measurements were carried out in a non-defective area for proving the existence of the A_0 mode. Secondly, the wave attenuation properties through butt weld and stiffener will be shown. Last, some acquisitions in the pseudo pulse-echo configuration helps to clarify the reflection phenomena.

a/ Through transmission configuration (case of a butt weld)

b/ Pseudo pulse-echo configuration (case of a butt weld)

Figure 13 Experimental set up using piezoelectric transducers

2.7 Experimental validation

2.7.1 Sensitivity of the SH_0 mode

Figure 14 shows the existence of a non-dispersive SH_0 wave generated by the EMATs and recorded at different propagation distance. The velocity of SH_0 is measured at 3183 m/s.

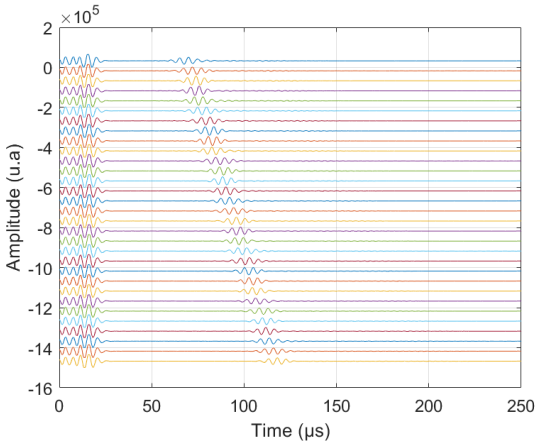

Figure 14 Amplitude-versus time signals recorded at different measurement locations, in a non-defective zone, in transmission configuration Figure 15 shows the frequency-wavenumber image, obtained from all recorded signals with applying a 2D–FFT analysis. The result is in good coherence with the theorical dispersion curves, confirms the generation of the SH_0 mode.

Figure 16 shows signals obtained in through transmission configuration. In both cases, when the receiver probe is placed at other side than the transmitter, an attenuation of the signal amplitude is observed, in addition to the attenuation due to the propagation distance observed in the non-defective zone. The attenuation is more important when propagating through stiffener than butt weld as shown in Figure 17.

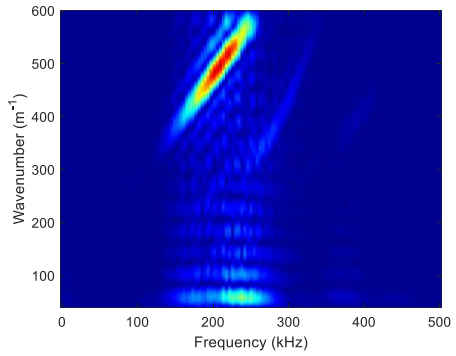

Figure 15: SH_0 experimental result in a non-defective zone. Frequency-wavenumber presentation obtained from all the recorded signals.

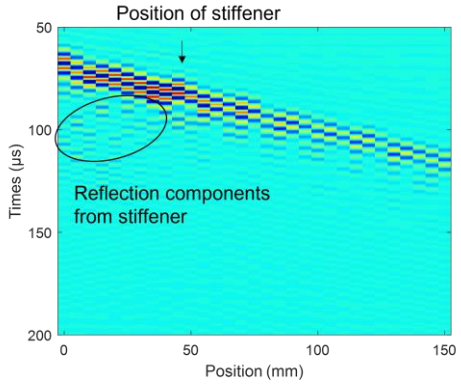

a/

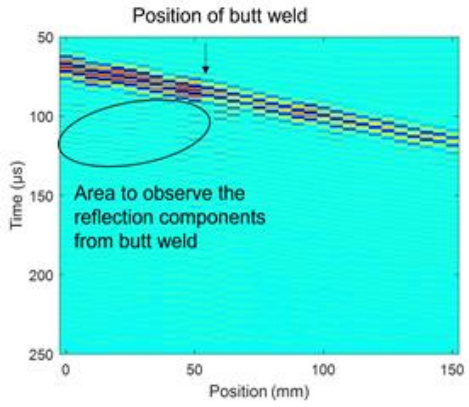

b/

Figure 16 Results in form of B-scan presentation of transmission measurements, in the cases with presence of stiffener and butt weld.

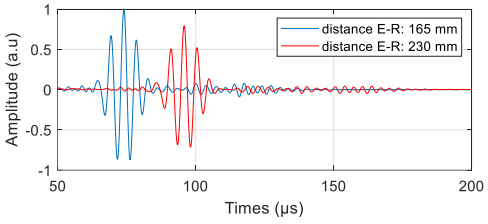

a/ Signals in a non-defective area. The two signals are normalized with respect to the peak amplitude of the 1st signal (in blue)

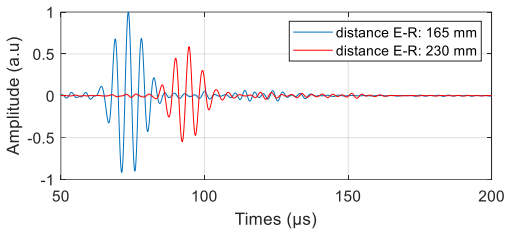

b/ Signals in the zone with presence of butt weld

Blue signal: The receiver and the emitter located on one side of the butt weld

Red one: The receiver and the emitter located on two sides of the butt weld

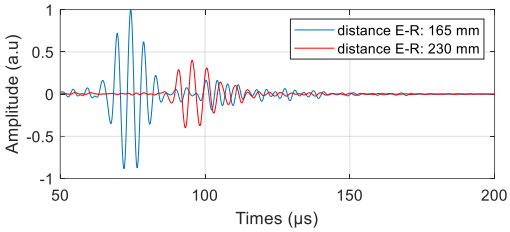

c/ Signals in the zone with presence of stiffener

Blue signal: The receiver and the emitter located on one side of the stiffener

Red one: The receiver and the emitter located on two sides of the stiffener

Figure 17 SH_0 attenuation comparison between in a non-defective zone and when encountering a butt weld or a stiffener

Looking to the reflection components, which are observed when emitter and receiver are placed in the same side with respect to the discontinuity, it is noted that the reflections are more important when the discontinuity consists in a stiffener than in the case of a butt weld.

Another more convenient way to study SH_0 reflection is using pulse-echo configuration. Here, pseudo pulse-echo configuration is exploited, in which the emitter and the receiver are placed side-by-side at known distances to the discontinuities (as described in the Figure 12-d). The Figure 18 shows signals achieved when two transducers placed at different distance to the stiffener. The SH_0 echo reflected from stiffener is clearly observed with a good coherence. The detection remain possible until 600 mm from where the signal to noise ratio becomes critical due to the attenuation.

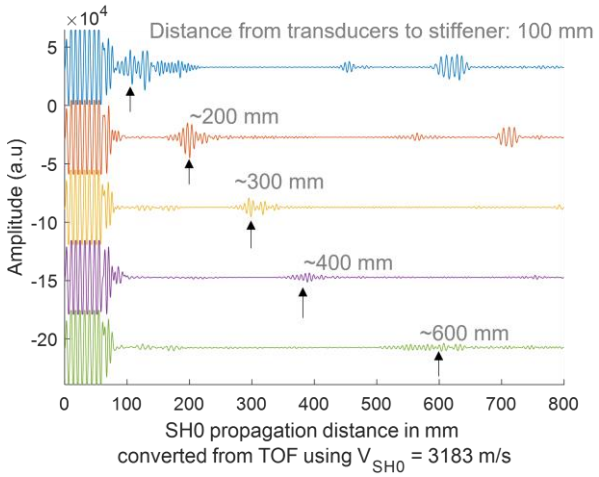

Figure 18 The detection of SH_0 reflection echo when encountering a stiffener

The changes in wave amplitude obtained in transmission and reflection configurations seems to be in good agreement. Indeed, through a stiffener, there is more loss in transmission than in the case of butt weld. Inversely, the amplitude of the reflection part is more important.

2.7.2 Sensitivity of the A_0 mode

The results of measurements in a non-defective zone are presented in the Figure 19.

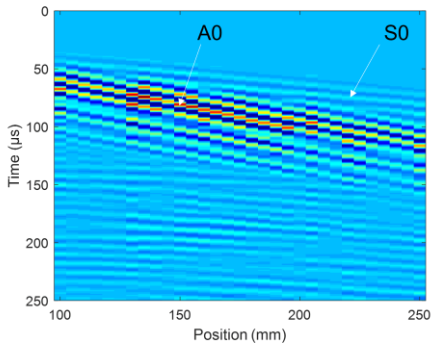

a/ B-scan presentation of all acquisitions in an intact zone

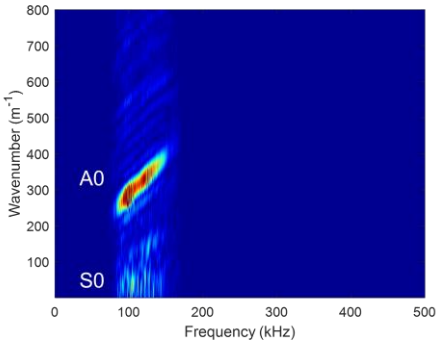

b/ Frequency-wavenumber presentation

Figure 19 Measurements in an intact zone. Generation of the A_0 mode which is dominant over the S_0 mode.

The frequency range that gave the best compromise of high amplitude signal and non-dispersive working point is [90 – 140] kHz. The A_0 mode is generated with much higher amplitude than the associated S_0 mode. The group velocity of A_0 mode is measured at 3125 m/s, that is in good coherence with the theorical value.

When propagating through butt weld or stiffener, the A_0 mode also suffers a signal amplitude attenuation, but at lower level than in the case of SH_0 mode.

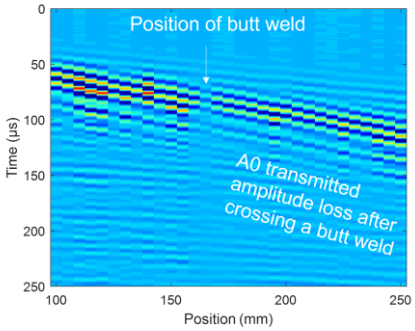

a/ B-scan presentation of the transmission measurements in a zone with a butt weld

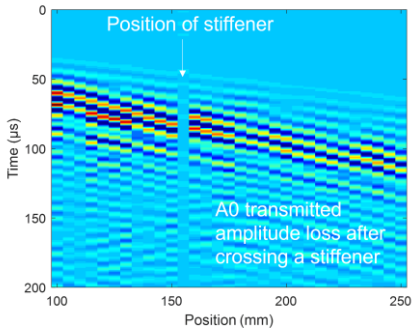

b/ B-scan presentation of transmission measurements in a zone with stiffener

Figure 20: Observation of transmission signal loss when propagating through a butt weld or a stiffener. The tendance is in good coherence with the observations in the case of SH_0 mode propagation.

As observed in the Figure 20, it is difficult to detect A_0 echoes from butt weld and stiffener. Even in pseudo pulse-echo configuration, by choosing judiciously some measurement positions on the mock-up, the echoes detection remains quite tricky.

In general, as the generation is omnidirectional, the signal composition is complex as it contains reflection components from all reflectors possible as discontinuities and the mock-up' free edges. There are also modes conversions. It should be noted that the echoes from discontinuities as stiffeners and buttwelds should be with the smaller amplitude than ones from free edges. In this case, advanced signal processing methods to reveal these components are needed. One of such method will be presented in section 3.

2.7.3 Numerical and experimental studies synthesis

The guided wave modes, SH_0 and A_0, were chosen as most potential candidates for the control of large industrial structures. Numerical simulations and experimental tests helped us to understand the behavior of these modes' propagation on the representative mock-up in term of transmission and reflection phenomena when encountering discontinuities. The results obtained in the experimental tests are generally in good agreement with those obtained in FEM simulations.

SH_0 has a big advantage as being completely non-dispersive and can be properly and selectively generated by EMAT transducers, which do not need any viscous acoustic coupling agent as special pasts or honey, generally used in such applications. When interacting with a butt weld or a stiffener, as being polarized in the plane, SH_0 is propagating with a small energy loss. The mode conversion level from SH_0 to SH_1 was not enough high to be detected experimentally because of its small amplitude. In the case of the propagation through a stiffener, the reflection part of the SH_0 can be detected with a good signal to noise ratio. Relating to the butt weld, it was difficult to conclude about the reflection. As mentioned in the case of the A_0 mode, it would need more measurements and advanced signal processing to detect a butt weld in a reflection configuration.

Using piezoelectric longitudinal compressional transducers having characteristics meeting the needs of the current experiment, the A_0 mode was properly generated with an amplitude dominant over the S_0 mode. It is advantageous that the generation is omnidirectional. It is recommended to work at a frequency range for which the A_0 mode is also non-dispersive. When interacting with discontinuities, A_0 exhibits a good transmission with low energy losses. This is consistent with the fact that, the reflected wave on part was not clearly detected. The mode conversion and the omnidirectionality of the mode, make the received signals and consequently their analysis more complex.

In the following part a method based on multi transducer measurement in reflection configuration, and an advantageous algorithm of signal processing to detect discontinuities, are presented.

3 TFM (TOTAL FOCUSING METHOD) ALGORITHM BY USING GUIDED WAVES

3.1 Introduction

The objective of this chapter is to set up a mapping method, based on guided waves, to make possible the detection of stiffeners and welds in order to locate them on the structure.

Several researchers have worked on locating obstacles and defects using guided waves. Haider et al [12] worked on an impact localization method on composite materials through 2 clusters of 3 sensors. The method demonstrated that it was possible to determine the position of the impact using an imaging method based on the time of flight of the guided waves generated by the impact. Others have worked on tomography imaging using surface waves to detect corrosion [13]. Huthwaite et al [14] and He et al [15] have also worked on tomography imaging methods. Other algorithms based on the Total Focusing Method (TFM) reconstruction technique using guided waves have demonstrated their effectiveness [7] [16]. This method seems to be interesting since it allows to obtain 2-D cartographies. At a given position on the mock-up described above (later a position of the robot), guided waves can be emitted by a phased array sensor. They are propagating in the plate and when they encounter discontinuities, they are reflected and received by the phased array sensor. Then, using TFM reconstruction the area to be controlled can be mapped. The dimensions of this area are greater than $1m^2$ in the case of Song [16] and a little less than $1m^2$ in the case of Huan [7]. But in reality, SH_0 and A_0 guided waves propagate over long distances, as it was demonstrated by Huan [17] using SH_0 waves enables propagation over a distance by 20 meters on buried tubes.

To study the use of TFM algorithm for detecting discontinuities on the representative mock-up, two approaches are led. First, 2-D numerical simulations in the (x, y) plane are conducted and second experiments are carried out on the representative mock-up.

3.2 Theory

By using TFM algorithm for each pixel (x, z) of a given image, the intensity is given by the following formula [18]:

$$I(x,z) = \left| \sum_{\text{for all tx, rx}} h_{tx,rx}\left(\frac{\sqrt{(x_{tx}-x)^2+z^2}+\sqrt{(x_{rx}-x)^2+z^2}}{c_l} \right) \right|$$

with t_x the transmitter and r_x the receiver, x_{rx} and x_{tx} their abscissas, $h_{tx,rx}$ the Hilbert transform of the emitted signal by t_x and received by r_x and c_l the propagation velocity of the wave.

Since the waves used here are guided waves, so $z_{rx} = z_{tx} = 0$, and the formula becomes (Figure 21):

$$I(x,y) = \left| \sum_{\text{for all tx, rx}} h_{tx,rx}\left(\frac{\sqrt{(x_{tx}-x)^2+(y_{tx}-y)^2}+\sqrt{(x_{rx}-x)^2+(y_{tx}-y)^2}}{c_l} \right) \right|$$

with y_{rx} and y_{tx} the ordinates of the transmitters and receivers.

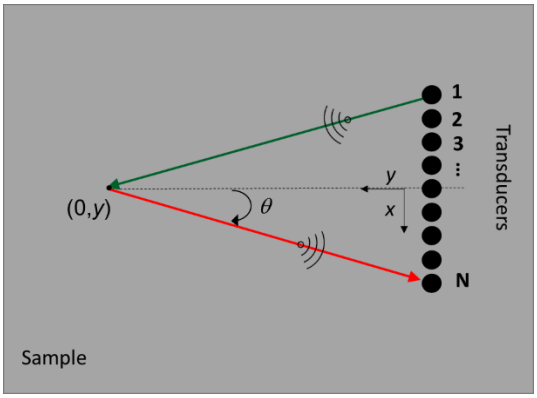

Figure 21: Explanation of the resolution of the TFM (in green the emission and in red the reception, to see the whole sequence refer to the video at the following address here)

3.3 *Numerical setup*

The Finite-Differences in Time Domain (FDTD) approach is used to simulate elastic wave propagation in 2D medium surrounded by simple sponge boundaries to avoid free edge plate reflections [19]. This assumption is made in order to work in the same conditions as on a boat hull where dimensions are very huge. To conduct simulations, a specimen with an inspected area of 1000mm x 1000mm containing ribs and stiffeners is modelled in the x-y 2-D plane. This inspected area is divided into 1000 x 1000 pixels, i.e 1 pixel / mm.

Simulations are conducted at the frequency of 200 kHz to generate only the A_0 mode. This means that the wavelength generated in the plate is equal to $\lambda = c/f = 3000/200x10^3 = 15$ mm.

According to Song [16], the imaging resolution that can be obtained from TFM is limited by wave diffraction. According to Rayleigh's criterion [20], the achievable imaging resolution, L_r, of the TFM at the imaging point at (0, y) is given by:

$$L_r = 0.61\frac{\lambda}{sin(\theta)}$$

So, discontinuity fitting into a pixel of 0.61λ x 0.61λ or less is difficult to be detected.

The sensors are modelized by omnidirectional point sources which generate a pure A_0 mode. 9 omnidirectional point sources (sensors) are modeled with a spaced distance (pitch) of 15 mm apart from each other.

The acoustic characteristics of the metallic plate, the stiffeners and the welds are summarized in the following table:

Table 2: Acoustic parameters of the designed sample for TFM simulations

	Density (kg/m^3)	**Phase velocity of mode A_0 at 200kHz (m/s)**
Plate	7850	3260
Stiffener	7850	2000
Welds	7850	2500

FDTD simulations is performed with material properties of density and elastic wave velocity, so slight acoustic impedance variations at the interfaces plate-weld or plate-stiffener are favoring wave reflections. These choices were made according to the 2D plane strain simulations and experimental observations obtained on the mock-up (refer to sections §2.4.1 and §2.7.1), i.e a stiffener reflects much more energy than a weld.

3.4 *Numerical results*

TFM algorithm is first performed on the numerical mock-up without defects in order to visualize stiffeners and weld's locations. The selected area contains 3 stiffeners (in green): 2 vertical and 1 horizontal and 2 welds (in red): 1 vertical and 1 horizontal. The results of this first numerical study are given in the Figure 22:

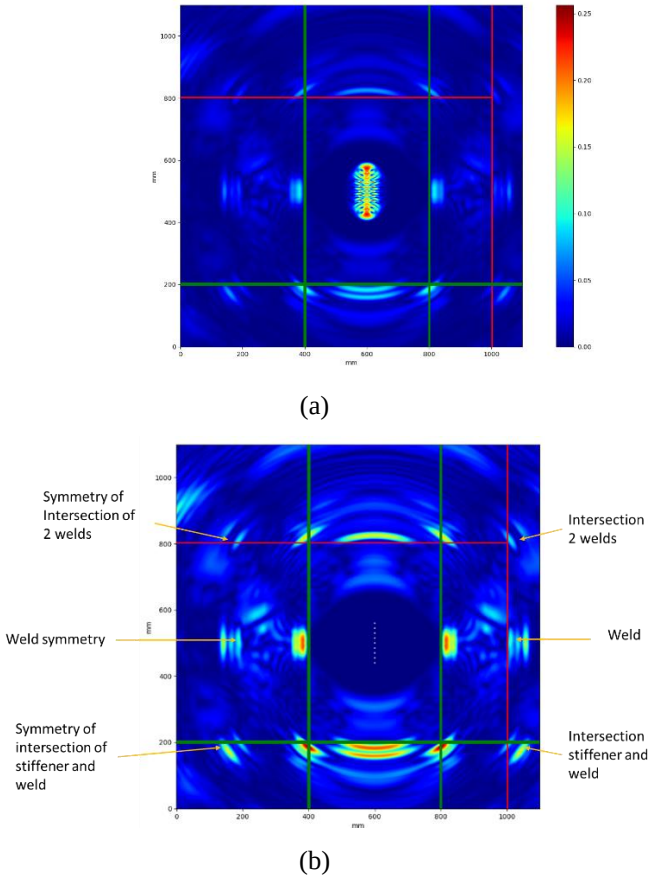

(a)

(b)

Figure 22: Numerical simulation result for TFM imaging using 9 omnidirectional sensors with15 mm pitch. (a) before blind zone removal (b) after blind zone removal

One can observe that there is a symmetry, respect to alignment axis of the sensors, of the obtained mapping related to the TFM reconstruction method. Indeed, this method is based on the calculation of the time of flight of the emitted wave. Knowing that sensors are omnidirectional, the waves could arrive from either side of the alignment axis of the sensors. This is problematic because it is impossible to determine which side the discontinuity comes from (a solution will be proposed in the next section).

The weld on the right of the image is well detected and well positioned but because of the symmetry effect, it is visible on the left of the image symmetrical about the alignment axis of the sensors. The same observation is done for the intersection of the 2 welds at the top right (in red). This intersection is also visible on the left because of the symmetry.

It should be noted that the weld and the stiffener which are located on the alignment axis of the sensors are, contrary to what is expected, visible. However, it should be noted that the spot is amplified by the symmetry effect.

Stiffeners are clearly visible and well located (Figure 22 (a)). The intersections between the stiffeners are also clearly visible. Indeed, an angle concentrates the energy and sends it back to the sensors like a 45° angled reflector as seen in the Figure 22

(b). It should also be noted that the spot is less marked when it is an angle between a stiffener and a weld or two welds. In fact, a weld is less visible than a stiffener given its acoustic property very similar to the metallic plate.

A blind zone around the sensors related to the wavelength (resolution) estimated around a 2,5λ = 40 mm is visible. In order to better visualize the discontinuities, in terms of contrast, the blind zone is removed and replaced by zeros (Figure 22 (b)). One can observe that the signature of a stiffener is different from that of the weld. The signal coming from the stiffener is split, since despite the low resolution, the wave can discriminate the first and the second edge of the stiffener.

TFM algorithm is secondly applied with the addition of three defects on the numerical mock-up. These defects have a square shape of different dimensions, with sides of 0.61λ/2, 0.61λ and 2x0.61λ. The defects are through thickness holes with density ρ =1.3 kg/m^3 and phase velocity c = 340 m/s. The objective is to verify the detectability of these defects after interacting with discontinuities such as stiffeners and welds. Another objective is to confirm the limit of detection (resolution) as expressed in the formula ($L_r = 0.61\frac{\lambda}{\sin(\theta)}$).

The results are given below. Defects are marked with red crosses on the Figure 23.

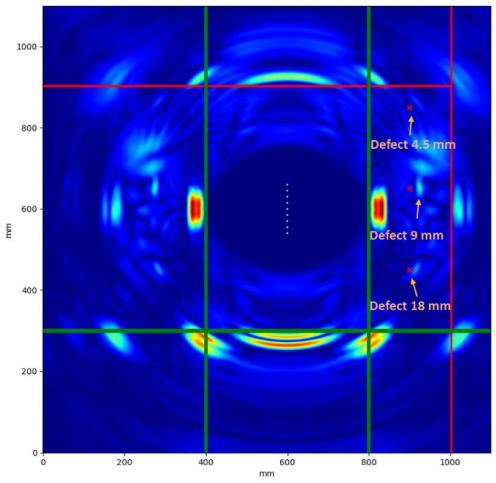

Figure 23: Result of the numerical study of TFM imaging using 9 omnidirectional point sensors spaced 15 mm apart in the presence of 3 defects of different sizes 0.61λ/2, 0.61λ and 2x0.61λ (red crosses).

As expected, the visible defects are the those of sizes greater than or equal to the theorical resolution i.e., 0.61λ ≈ 9 mm. The smallest defect of size 0.61λ/2 ≈ 4.5 mm is missing (indetectable).

3.5 Experimental setup

After verifying by numerical study that stiffeners, welds, and defects are detectable with TFM algorithm, experimental trials are conducted in the same conditions.

3.6 Experimental results

First, a check that the stiffeners and welds are visible is made. A simplified configuration with a single stiffener and a single weld is made in order to simplify the understanding of the mapping which is complicated by the problem of symmetry explained above. The configuration is described in Figure 24(a) where the free edge of the plate is located at x = 250 mm and y =0, the stiffener at x = -150 mm and y = 0 and the weld at x = 0 and y = 150 mm. The result obtained after propagating the A0 wave and applying the TFM algorithm is given in the Figure 24(b).

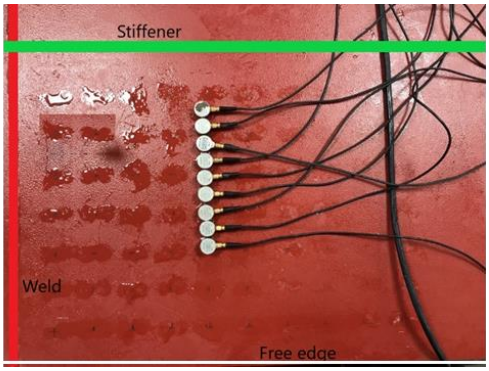

(a)

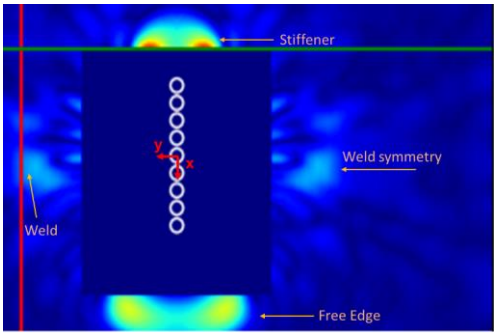

(b)

Figure 24:(a) Simplified setup to detect a stiffener and a weld (b) result of TFM mapping

As obtained in the numerical study, the stiffener is clearly visible, and the weld is less so. The free edge is also clearly visible.

Secondly, an acquisition using the same experimental set-up on a largest area is conducted. This is done to confirm the detectability of the different discontinuities on a more complex and larger area. The area is constituted of 3 horizontal stiffeners, a vertical stiffener, horizontal weld and vertical free edge.

In parallel an equivalent numerical simulation is carried out for comparison. The results are given in the Figure 25. Interpretations of the obtained results remain difficult due to the problem of symmetry despite the visualization of the discontinuities on both the numerical (Figure 25 (a)) and the experimental (Figure 25 (b)) 2D-cartographies.

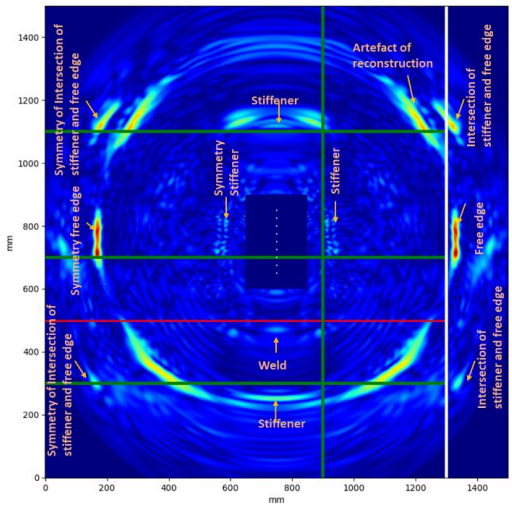

(a)

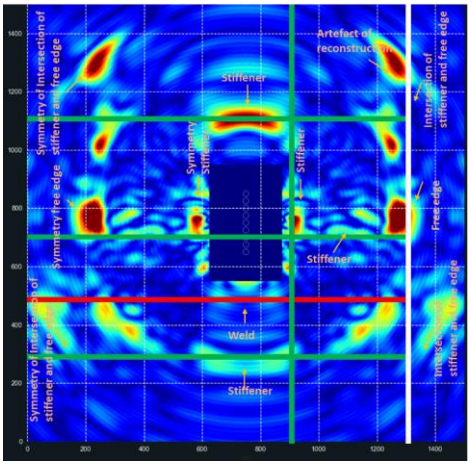

(b)

Figure 25: Comparison of the numerical (a) and the experimental (b) results to detect the different stiffeners and weld

In the following part, a solution to remove symmetry in order to facilitate the interpretation is presented.

3.7 Symmetry removal

The main problem happened after TFM algorithm application is the appearance of a symmetrical image about the sensors line. One of the two spots does not correspond to any real discontinuity (Figure 26), this means that it is difficult to easily locate discontinuity. It is therefore important to find a solution to be able to avoid this phenomenon inherent to the method.

For removing the symmetry, a solution is proposed. This solution consists of changing the position of the array sensors perpendicularly to their alignment axis. So, 2 cartographies of the same area are needed with a shift of 100 millimeters (Figure 26). Thus, if the positions of the discontinuities are conserved, the symmetrical spot will disappear. By multiplying the two TFM cartographies pixel by pixel, and also taking the square root in order to keep the same scale as before, the spot corresponding to the discontinuities remains. The two symmetrical spots relating to the 2 different positions disappear afterwards (Figure 27).

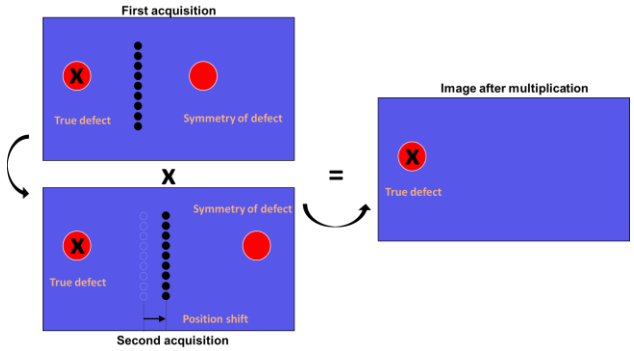

Figure 26 : schematic for symmetry problem removal

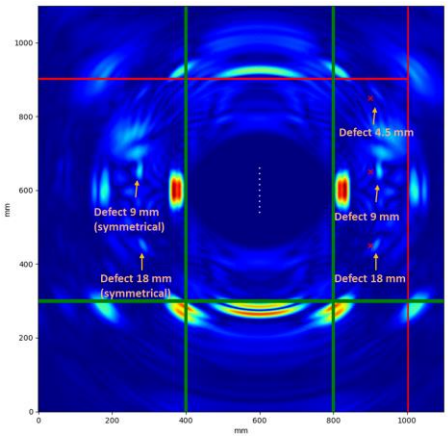

(a)

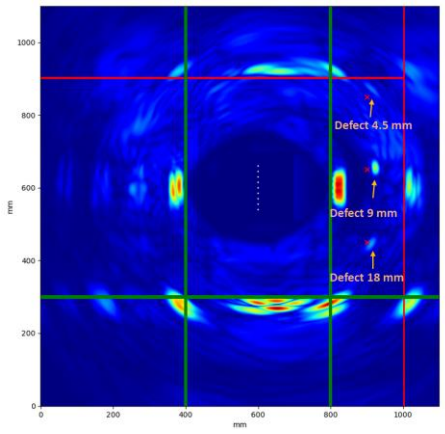

(b)

Figure 27 : cartographies obtained with TFM (a) before shift (b) after shift and multiplication

From Figure 27, a comparison of the numerical cartographies before removal of symmetry (Figure 27(a)) and after removal (Figure 27(b)) is made. The symmetries of the defects of size 18 mm and 9 mm which were located at x = 300 mm have disappeared. Also, the symmetry of the weld which was visible

on the left at x = 180 mm has been greatly reduced but a residual spot remains.

To delete these residual spots due to the symmetry, a thresholding operation is applied. By choosing a suitable threshold, all residual spots as shown in the Figure 28 are removed.

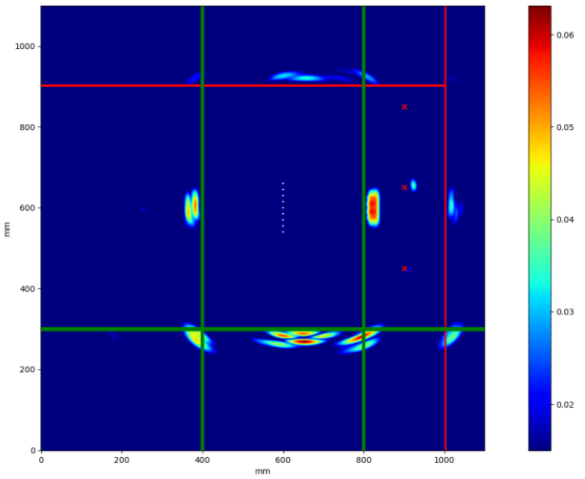

Figure 28 : TFM mapping after removal of symmetry and after thresholding

This method eliminates the symmetry effect but requires two acquisitions at 2 different positions. Therefore it requires more time and more computational resource for the reconstruction of the TFM cartography. This problem could be solved in another way by working on directional sensors which only send waves in a half plane.

4 CONCLUSION

In this paper, the interaction between guided waves and geometric discontinuities of a large structure (boat hull) was considered. First, numerical simulations were performed considering two types of guided waves (antisymmetric Lamb waves (A), shear horizontal waves (SH)) and different geometric discontinuities (welding, stiffener). The results of this analysis show the advantages of the SH_0 mode for the detection of discontinuities, particularly in reflection. Indeed, the SH_0 mode is not dispersive and does not present mode conversion in reflection. However, it should be noted that ribs are less well detected than welds. These results have been validated experimentally on a representative mock-up of a section of boat hull.

In order to overcome the resolution limits of the conventional single-element method, a multi-element imaging technique is proposed in this work based on the TFM algorithm. First, a numerical model was developed based on the characteristics of the test mock-up. The results show that all the discontinuities were detected with good resolution. The first experimental validation tests were carried out using conventional PZT transducers. Although the modal selectivity of these sensors is not optimal, the results obtained make it possible to detect both welds and ribs present on the mock-up. in the future works, the optimization of the SH_0 mode excitation is considered in order to improve the resolution.

Acknowledgement

This project has received funding from the European Union's Horizon 2020 research and innovation programme under grant agreement No. 871260.

The authors thank M. Yves Guillermit from the company Weez-U Welding [21] for his assistance to model the representative mock-up and for his knowledge in welding process.

5 REFERENCES

[1] a. P. C. M. J. S. Lowe, "Rapid, long range inspection of chemical plant pipework using guided waves," *AIP Conference Proceedings,* vol. 557, p. 180, 2001.

[2] L. A. G. R. B. Pavlakovic, "The reflection of guided waves from notches in pipes: a guide for interpreting corrosion measurements," *NDT & E International, ,* vol. 37, pp. 167-180, 2004.

[3] S. G. P. a. G. H. G. Dobie, "The feasibility of synthetic aperture guided wave imaging to a mobile sensor platform," *NDT and E International,* vol. 58, pp. 10-17, 2013.

[4] M. Tabatabaeipour and O. T. e. al, "Application of Ultrasonic Guided Waves to Robotic Occupancy Grid Mapping," *Mechanical Systems and Signal Processing,* 2021.

[5] A. Leleux, *Contrôle non destructif de composites par ondes ultrasonores guidées, générées et,* Université de Bordeaux, Thèse de doctorat 2012.

[6] Q. Huan, M. Chen and F. Li, "A practical omni-directional SH wave transducer for structural health monitoring based on two thickness-poled piezoelectric half-rings," *Ultrasonics,* 2018.

[7] Q. Huan, "A high-resolution structural health monitoring system based on SH wave piezoelectric transducers phased array," *Ultrasonics,* vol. 97, pp. 29-37, 2019.

[8] B. P. T. Clause, "Modélisation des traducteurs électromagnétiques acoustique (EMAT) pour le contrôle non-destructif (CND) de milieux ferromagnétiques," 2018.

[9] H. Salzburger, "EMAT pipe inspection with guided waves welding in the world," *le soudage dans le monde , pp.* 5-6, 2013.

[10] H. Walaszek, "Accurate ultrasonic stress mesurement in already tightenedbols by means of optimized EMAT," *WCNDT,* 2016.

[11] J. Li, Z. S. Khodaei and M. H. Aliabadi, "Boundary element modelling of ultrasonic Lamb waves for structural health monitoring," *Smart Materials and Structures,* vol. 29, 2020.

[12] M. F. Haider, "Experimental Investigation of Impact Localization in Composite Plate Using Newly Developed Imaging Method," *Inventions 2018,* pp. 3-59, 2018.

[13] W. Li, "Combination of nonlinear ultrasonics and guided wave tomography for imaging the micro-defects," *Ultrasonics,* vol. 65, pp. 87-95, 2016.

[14] H. P, "High-resolution guided wave tomography.," *Wave Motion,* vol. 93, pp. 50-979, 2013.

[15] H. J, "Guided wave tomography based on least-squares reversetime," *Struct Health Monit,* 2019.

[16] H. Song, "Super-resolution visualization of subwavelength defects via deep learning-enhanced ultrasonic beamforming: A proof-of-principle study," *NDT and E International,* vol. 116, p. 102344, 2020.

[17] Q. Huan, "Long-distance structural health monitoring of buried pipes using pitch-catch T(0,1) wave piezoelectric ring array transducers," *Ultrasonics,* vol. 106, p. 106162, 2020.

[18] C. Holmes, "Post-processing of the full matrix of ultrasonic transmit–receive array data for non-destructive evaluation," *NDT&E International,* vol. 38, pp. 701-711, 2005..

[19] C. Cerjan, "A non reflecting boundary condition for discrete acoustic and elastic wave equations," *GEOPHYSICS,* vol. 50, no. 4, pp. 705-708, 1985.

[20] G. JW., Introduction to Fourier Optics. third ed., Englewod, Colorado.

[21] "https://weez-u-welding.com/," [Online]. Available: https://weez-u-welding.com/. [Accessed 25 03 2022].

[22] W. U, "Weez U welding," [Online]. Available: https://weez-u-welding.com/. [Accessed 10 03 2022].

[23] Q. Huan, M. Chen, Z. Su and F. Li, "A high-resolution structural health monitoring system based on SH wave piezoelectric transducers phased array," *Ultrasonics,* 2019.

[24] M. Haider, "Experimental Investigation of Impact Localization in Composite Plate using Newly developed imaging method," *inventions,* pp. 3-59, 2018.